

University of Warwick institutional repository: <http://go.warwick.ac.uk/wrap>

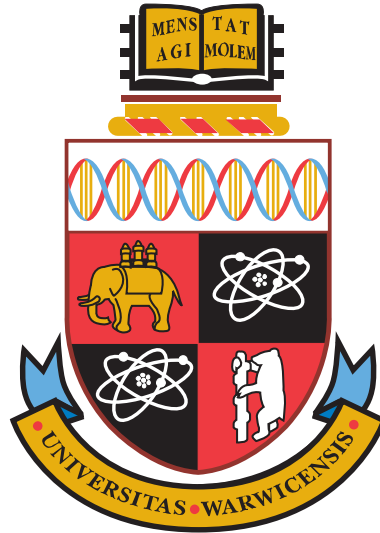
A Thesis Submitted for the Degree of PhD at the University of Warwick

<http://go.warwick.ac.uk/wrap/54323>

This thesis is made available online and is protected by original copyright.

Please scroll down to view the document itself.

Please refer to the repository record for this item for information to help you to cite it. Our policy information is available from the repository home page.



**Stochastic Pattern Formation in Growth Models
with Spatial Competition**

by

Adnan Ali

Thesis

Submitted to the University of Warwick

for the degree of

Doctor of Philosophy

Centre for Complexity Science and Mathematics Institute

September 2012

THE UNIVERSITY OF
WARWICK

Contents

Acknowledgments	iv
Declarations	v
Abstract	vi
Notation	vii
Chapter 1 Introduction	1
Chapter 2 Non-equilibrium growth	9
2.1 KPZ universality class	11
2.1.1 KPZ equation	11
2.1.2 Connections to Edward Wilkinson universality class	13
2.1.3 Lateral growth	15
2.1.4 Scaling arguments	17
2.1.5 Exactly solvable models in the KPZ class	19
2.2 Eden model	20
2.2.1 Lattice models	21
2.2.2 Off-lattice model	22
2.2.3 Exact Solution of Eden models	26
2.3 Growth and pattern formation in biological systems	26
2.3.1 Space-limited population growth	29
Chapter 3 Segregation patterns in growing populations	33
3.1 Introduction	33
3.2 Family of Eden models	35
3.3 Main Results	39
3.3.1 Quantitative analysis of the colony surface	39
3.3.2 Domain boundaries	44

3.3.3	Sector patterns	47
3.4	Realistic reproduction times	49
3.5	Conclusion	51
Chapter 4	Computing amplitudes for the Eden model	54
4.1	Introduction	54
4.2	Dynamic Renormalization group theory	55
4.3	Mode coupling calculation	60
4.3.1	Deriving the correlation function	62
4.3.2	Deriving the form of the gradient squared	63
4.3.3	Deriving the prefactor of the domain boundary	65
4.4	Conclusion	68
Chapter 5	Scale invariant growth processes in expanding space	69
5.1	Introduction	69
5.2	Main results	73
5.2.1	Mapping	74
5.2.2	Basic properties of the mapping	75
5.3	Applications to self-similar models	77
5.4	Generalized geometries	80
5.4.1	Decreasing radial domain	81
5.4.2	Motion on a general evolving domain	82
5.5	Generalized local interactions	84
5.5.1	Finite size particles	85
5.5.2	Structures in $n + 1$ dimensions	86
5.5.3	Branching coalescing structures	87
5.6	Discussion	91
Chapter 6	Exact results on scale invariant growth	94
6.1	Introduction	94
6.2	Rigorous derivation of the mapping	95
6.2.1	Brownian motion	96
6.2.2	α -stable Lévy process	99
6.2.3	Fractional Brownian motion	100
6.3	Analytical derivation for $\langle N_F \rangle$ and $\langle D_F^2 \rangle$	104
6.3.1	Computing statistics for fractional Brownian motion	105
6.3.2	Computing statistics for α -stable Lévy process	107

Chapter 7	Growth, competition, range expansions and beyond	109
7.1	Summary of the main results	109
7.2	Population fronts in competition growth models	111
7.2.1	Introduction	111
7.2.2	Equivalence of radial and fixed domain colonies	112
7.2.3	Discussion	115
7.3	Further applications	117
7.3.1	Non-local growth and DLA	117
7.3.2	Possible application in cosmology	119
Appendix A	Elliptic theta functions	122
Appendix B	Stochastic analysis	123
B.1	Probability space	123
B.2	Stochastic process	124
B.3	Stochastic integration	124
B.4	Itô formula	126

Acknowledgments

First and foremost, I would like to express my deepest gratitude to my supervisor Stefan Grosskinsky. I cannot stress how much I have appreciated his constant guidance, support and dedication throughout the past few years. In particular, I am thankful to him for his continuous availability to discuss my work, and sharing his wisdom in the most benevolent manner. I would also like to thank him for reading through my thesis many, many times and I appreciate his insightful comments.

I would also like to thank my second supervisor Ellák Somfai, who has also played a significant role in my research. He dedicated more time and effort towards me than what many students get from their main supervisor. Additionally, I would also like to thank him for reading my through thesis and providing me with his comments. A special thanks is given to Robin Ball for his inspiring discussions with me.

My work has been supported by the Engineering and Physical Sciences Research Council as part of the University of Warwick Complexity Science Doctoral Training Centre. I am grateful to the Complexity DTC and EPSRC for allowing me to conduct my research. I would also like to thank all members of the DTC for making my time in the department so enjoyable.

I would also like to thank all members of my family for their constant support, encouragement and belief in me. A warmest gratitude is given to my parents for everything they have done for me. In particular, a special thanks is given to my wife Roheena Ali for her affection and support.

Finally and most importantly, I would like to thank my Lord Allah almighty, who has guided me from darkness to light.

Declarations

This work has been composed by myself and has not been submitted for any other degree or professional qualification.

- Parts of Chapter 2 have appeared in the article titled: Pattern formation through genetic drift at expanding population fronts, *Advances in Complex Systems*, Vol. 13, No. 3 (2010) 349366. Authors: Adnan Ali and Dr. Stefan Grosskinsky.
- Results in Chapter 3 and parts of Chapter 4 have been published in the article titled: Reproduction-time statistics and segregation patterns in growing populations, *Physical Review E* 85, 021923 (2012). Authors: Adnan Ali, Dr. Ellák Somfai and Dr. Stefan Grosskinsky.
- Results from Chapter 5 have been submitted for publication, with article titled: Scale invariant growth processes in expanding space. Authors: Adnan Ali, Prof. Robin C. Ball, Dr. Stefan Grosskinsky and Dr. Ellák Somfai.
- Parts of Chapter 6 will be submitted for publication in the near future.

Abstract

The field of stochastic growth encompasses various different processes which are ubiquitously seen across the physical world. In many systems, stochasticity appears quite naturally, where inherent randomness provides the right setting for the tone of motion and interaction, whose symphony leads to the surprising emergence of interesting patterns and structure. Although on the microscopic scale one can be overwhelmed by the randomness arising from the fluctuating interactions between components, on the macroscopic scale, however, one is mesmerized by the emergence of mathematical beauty and symmetry, leading to complex structures with fractal architecture.

Competition between components adds an extra degree of complexity and leads to the possibility of critical behaviour and phase transitions. It is an important aspect of many systems, and in order to provide a full explanation of many natural phenomena, we have to understand the role it plays on modifying behaviour. The combination of stochastic growth and competition leads to the emergence of interesting complex patterns. They occur in various systems and in many forms, and thus we treat competition in growth models driven by different laws for the stochastic noise. As a consequence our results are widely applicable and we encourage the reader to find good use for them in their respective field.

In this thesis we study stochastic systems containing interacting particles whose motion and interplay lead to directed growth structures on a particular geometry. We show how the effect of the overall geometry in many growth processes can be captured elegantly in terms of a time dependent metric. A natural example we treat is isoradial growth in two dimensions, with domain boundaries of competing microbial species as an example of a system with a homogeneously changing metric. In general, we view domain boundaries as space-time trajectories of particles moving on a dynamic surface and map those into more easily tractable systems with constant metric. This leads to establishing a generic relation between locally interacting, scale invariant stochastic space-time trajectories under constant and time dependent metric. Indeed *“the book of nature is written in the language of mathematics”* (Galileo Galilei) and we provide a mathematical framework for various systems with various interactions and our results are backed with numerical confirmation.

Notation

$a \ll b$ b asymptotically dominates a

$a \propto b$ a is propotional to b

$a \rightarrow b$ Quantity a converges to quantity b

$|X|$ Cardinality of the set X

pdf Probability density function

cdf Cumulative distribution function

pde Partial differential equation

∇ Defined as $\nabla := (\frac{\partial}{\partial x_1}, \dots, \frac{\partial}{\partial x_n})$ for $x \in \mathbb{R}^n$

Δ Laplacian operator, defined as $\Delta := \sum_{i=1}^n \frac{\partial^2}{\partial x_i^2}$ for each $x_i \in \mathbb{R}$

$\langle a \rangle, \mathbb{E}[a]$ Expectation of random variable a with to respect to a probability measure \mathbb{P}

$\stackrel{\text{dist.}}{=}$ Denotes equality in distribution for two random variables (Chapter 5 and 6)

L The system size for a fixed, strip and linear geometry

$y(x, t)$ The KPZ interface with $x \in \mathbb{R}^n$ and $t \geq 0$ (Chapter 2, 3 and 4)

(v_0, ν, λ, D) Parameters of the KPZ equation (Chapter 2, 3 and 4)

(α, β, z) Exponents of the KPZ universality class (Chapter 2, 3 and 4)

$\eta(x, t)$ White-noise with mean 0 and space-time correlations $\delta(x - x')\delta(t - t')$, with δ the Dirac-delta function (Chapter 2, 3 and 4)

$S(t), S(r_0, t)$ Roughness of an interface (Chapter 2 and 3)

$C(l, t)$ Height-height correlation function (Chapter 3 and 4)

ξ_{\parallel} Lateral correlation length (Chapter 2, 3 and 4)

$h(t)$ Average height of the linear interface (Chapter 2)

$f(\cdot)$ Family-Vicsek scaling function (Chapter 2 and 3)

$\Psi(t)$ Denote's the general index set of particles at time t (Chapter 3)

F_{δ} Cumulative distribution function of reproduction times with parameter $\delta \in (0, 1]$ (Chapter 2)

T Random reproduction time (Chapter 2 and 7)

τ Vertical correlation length (Chapter 2)

ζ GUE or GOE random variable (Chapter 2)

$\text{Exp}(1/\delta)$ Exponential distribution with mean δ

$\text{Gamma}(\rho_3, \rho_4)$ Gamma distribution with parameters $\rho_3 > 0$ and $\rho_4 > 0$

$(X_h, h \geq 0)$ Stochastic process in a fixed geometry

$(Y_r, r \geq r_0)$ Stochastic process moving on the perimeter of a growing circle

γ Local scale invariance exponent such that $\gamma > 0$ (Chapter 5, 6 and 7)

H Hurst exponent such that $H \in (0, 1)$

$Z := (Z_t, t \geq 0)$ Rescaled stochastic process

$B = (B_t, t \geq 0)$ Standard Brownian motion

$B^H = (B_t^H, t \geq 0)$ Fractional Brownian motion with Hurst exponent $H \in (0, 1)$

$L^{\alpha} = (L_t^{\alpha}, t \geq 0)$ α -stable Lévy process with $\alpha \in (0, 2)$

$M(h)$ Mean square displacement (Chapter 3 and 4)

σ_δ^2 Prefactor of the boundary process (Chapter 3, 4 and 7)

ψ Brillouin zone (Chapter 4)

$G_0(k, w)$ Bare propagator (Chapter 4)

$\langle N_F(h) \rangle, \langle N_R(r) \rangle$ Number of particles on the fixed domain and radial domain, respectively

$\langle D_F^2(h) \rangle, \langle D_R^2(r) \rangle$ Inter-particle distance squared function on the fixed domain and radial domain, respectively

$L(t)$ Continuous function used for the length of an isotropic growing domain $[0, L(t))$ (Chapter 5 and 6)

ρ Density of particles (Chapter 5 and 6)

$\vartheta_3(\cdot, \cdot)$ The elliptic theta function of third kind (Chapter 5 and 6)

\mathcal{F} σ -algebra (Chapter 6)

Chapter 1

Introduction

Stochastic growth processes are observed ubiquitously in many phenomenon across nature and lead to the formation of rough complex surfaces with a variety of interesting patterns [95, 204, 216]. These patterns are very fascinating and have attracted a tremendous amount of attention in recent years from a range of research fields, where similar structural behaviour is seen to arise in many systems which at first sight appear to have no connection (see [17, 132, 142] for a general review). For instance, the propagation of rough surfaces are observed in a broad variety of physical and biological processes, examples include the spread of fluid in a porous or disordered medium [77, 161], directed polymers in a random medium [28, 39, 101], colloid aggregation [129], vapor and electron deposition [128], molecular-beam epitaxy [217], and bacteria and tumor growth [27, 47, 205].

In the last three decades there has been a considerable effort in understanding the dynamics of growing random surfaces. From a theoretical perspective, much of the interest is due to the recognition that surface fluctuations, despite being random, appear to have intrinsic scaling behavior in both space and time, where the structures that appear are typically very complex but can be described in terms of fractal geometry [52, 142, 205]. Although many growing structures themselves are not fractals, their surface however exhibits anisotropic scaling, a characteristic of scale invariant geometry.

Stochastic growth leading to scale invariant structures are abundantly seen across nature. Examples include diffusion-limited aggregation [161, 216], river basins [173], and self-affine domain boundaries forming behind growing fronts for spatial competition models [45, 177] with applications in microbial growth [69, 111]. The latter can be modelled as trajectories of locally interacting particles, a picture adopted in this thesis. The overall geometry has a strong impact on the growth

process. A dramatic example is viscous fingering, where in constant width channel geometry a stable Saffman-Taylor finger of fixed shape propagates [176], while in radial geometry a continuously tip splitting branched structure emerges [160, 197]. In biological growth spatial range expansion is often coupled to drift and competition in the genetic pool and these processes are identified to have a major influence on the gene pool of natural populations [111, 127]. This is quite visibly seen in colonies of microbial species, where spatial range expansion leads to striking spatial segregation in populations along the advancing frontier. As a consequence, sectoring patterns emerge as a distinct footprint of past expansions. These patterns are a result of dynamical competition between distinct and fluctuating phases, and play an important role in determining the final morphology [70, 71].

In general, the combination of spatial competition with range expansions can have a variety of consequences on the dynamical behaviour of a system. For example in evolutionary biology, this leads to a phenomenon known as genetic drift, which we studied in [5]. Genetic drift is one of several evolutionary processes which lead to changes in allele frequencies in a population over time. It is different from other non-random processes such as natural selection, where over a period of time biological traits become more or less common in a population due to differential reproduction leading to heritable advantages becoming dominant. Genetic drift is driven purely by random sampling and chance events, and is now widely accepted to be a major evolutionary force (see [69, 137] and references therein). In large populations the variations introduced by genetic drift are typically small compared to the population size, and these systems are dominated by the law of large numbers. But in small populations genetic variation and fluctuations in allele frequencies can have a significant impact and may even lead to speciation i.e. dominance of a single allele [2, 71, 151].

For populations that undergo range expansions, the local reproductive population is smaller than the whole, therefore the effects of random sampling have a significant impact on the allele frequencies, where chance effects are enhanced. In such cases genetic drift can therefore be considered as the major force for spatial segregation and genetic demixing. For some species such as humans it has even been shown to be the primary force responsible for particular set of genetic features [2, 32]. The changes brought by genetic drift can be beneficial, increasing adaptation speed to changing environmental challenges and therefore the chances of survival. They can also be neutral or harmful when gene variants disappear, which results in a reduced genetic variability in the population [94].

Spatial range expansion is a very common non-equilibrium process in nature

and can be seen to occur in processes such as viscous fingering [161, 176], crystal growth [113, 125, 153] and grain coalescence in alloys [170]. In a variety of these processes the morphology is generated through the influence of factors such as diffusion, quenched disorder, interface roughness, noise, nucleation, and so on. Common patterns amongst them are fractal structures [17, 132]. These structures consists of a collection of stable phases that grow steadily into space with some control parameters [177]. Such structures emerge quite frequently in various physical and biological systems, leading to the appearance of a variety of patterns, which are visibly seen in systems such as turbulent fluids [22] or in the growth of bacterial colonies [112]. The problem is to determine how the various mechanisms introduced by range expansion affect growth dynamics, pattern formation and the resulting interplay between phases.

In natural systems, the growing entities usually exhibit additional degrees of freedom. This is most prominent in biological settings, where spatial expansion has been seen to occur in the history of many organisms [32, 175, 196]. A common familiar theme is that in response to environmental changes, such as climate and biophysical, species tend to move to favorable habitats [71, 80]. This spreading process is driven by cooperative and non-linear evolution rules, where during expansion the system develops features which are often rather complex [202]. Over time as a direct result of previous spatial expansions, strong genetic differences occur between the characteristics of the lineage. These differences are subsequently amplified by a genetic bottleneck, where the genetic variability of the entire population is seen to increase and subsequently leading to biodiversity. In the case of population migration, due to a moving bottleneck at the expanding frontier the genetic diversity of the sub-population depends sensitively on the population dynamics of the colonist [57, 70, 211]. For example, the ‘Out of Africa’ theory combines together factors such as previous range expansions, low population densities and random genetic drift to explain the major genetic differences that exist between *Homo sapiens*. In addition, the phenomenon known as the ‘Isolation by Distance’ explains the genetic similarities within a particular region [169, 172].

Recently, microbial systems have progressively become a valuable tool for understanding fundamental aspects of evolutionary biology and are now at the leading-edge for providing answers to philosophical questions such as the origin of species [49]. In particular, due to attributes such as large population sizes and rapid generation times, microbial experiments are now being used to study spatially structured populations. Here, phenomena such as the impact of range expansions on the genetic diversity can be measured [69, 112]. There is an increasing amount of evidence

that spatial structures are actually very crucial, where they affect spatiotemporal dynamics of interacting components and are important characteristics of ecological systems. Interaction and competition are ever-present amongst all species, where they lead to Darwinian selection and speciation, which is seen to characterize the structure in phylogenetic trees. Due to their facile nature, microbial systems have established themselves as excellent systems for not just the study of evolutionary forces and biodiversity, but also for the formation of defensive alliances, as well as structural complexity [70, 90].

The classic case of systems containing ideal particles rarely occur in nature and variations in physical or architectural properties in particles are present in many systems. In particular, in context of ecological systems, spatial heterogeneity in competing microbial species attracts much interest due to displaying the emergence of characteristics such as stability, biodemography and coexistence [90, 211]. Quite surprisingly, many of these processes can be understood by using the methods and tools from statistical physics. Here stochastic systems containing interacting particles have progressively been used to shed light on the dynamics of spatially extended systems. In particular, they have provided a deeper insight into key features of various interactions and their relative importance on the dynamical behaviour [71, 120].

Numerous example can be cited where the use of statistical physics has lead to novel insights once applied to biological problems. Some of these include the application of statistical mechanics to neural networks [89, 184], stochastic walkers with long range correlation functions to model DNA sequences [35], or the use of phase transition theory to understand the behavior of animal collectives [64]. A striking instance of alliance between physics and biology is seen in the emergence of spatial patterns produced by growing microbial colonies and has become the focal point of many intense studies in statistical physics during the previous few decades [23, 155]. Thus a clear qualitative understanding has emerged of the various morphological patterns that such colonies exhibit.

Typically growth begins with a strip or drop of a culture containing microorganisms, which are inoculated on a petri dish. Over time, the growth and division of cells results in the emergence of a colony with morphological structure that varies with the initial nutrients and agar concentration levels [155, 199, 207]. Although the microscopic behaviour appears random and disordered, at macroscopic length scales one can observe a range of interesting patterns and interfaces. Some colonies have a compact shape, with a rough surface, similar to the structures confronted in fluid flow such as spilled coffee, others are branched morphologies, reminiscent

of the arms observed in viscous fingering or crystal growth [17, 136]. A common question is; are these patterns universal in nature and if so, are there some general principles which are common to processes such as colony growth, fluid flow and crystal growth?

The fascination with researching growing colonies of microbial species stems from rapidly increasing interest in fractal growth phenomena arising in biology. More and more experimental investigations into biological structures reveal the fractal nature of various objects, some examples are the structure of the bronchial tree or the dendritic pattern of neurons, spiral fractals occurring in clouds, and fractal branching patterns in electrical discharge (see [132, 142, 204] for a broad review). The formation of such structures are influenced by a large number of factors and in practice it is hard to investigate all of them [17]. Through a combination of physical and biological strategies, one can hope for attaining a heuristic understanding of the global dynamics in these systems. A natural question is whether these systems and their structural properties can be captured by identifying a small number of laws. This can lead to determining a suitable model, where the microscopic details only include the essential physics and ignore the less important details.

In this thesis we use the methodology of non-equilibrium statistical mechanics to understand spatial competition in stochastic growth processes. Of particular interest are models of biological systems with radially symmetric growth, such as bacterial colonies or tumors. Although our work is purely theoretical, as an application we treat the formation of patterns occurring in microbial populations with competing strains, which has received a tremendous amount of interest recently [69, 70, 71, 111, 112, 127].

Central to our study is non-equilibrium growth and its influence on species spreading, which is a physical process that is very common. Examples can include processes such as deposition, diffusion, adsorption and aggregation on a surface, fluid flow in porous media, dendritic growth, electro-convection of turbulent liquid crystal, epidemic spreading, etc (see [17, 142] for a general review). Over the years, different collections of such processes have been extensively studied using experimental and simulation tools. In the latter, the validity of the results depend sensitively on the essential physical details, including the embedding geometry. It can be observed that the morphologies which emerge due to spreading phenomena are not universal under a statistical physics terminology and depend on the considered underlying geometry.

Our work deals with spatial growth models of particles of the same size (or type) and we investigate the impact of the geometry on the growth mechanism,

particle motion, interparticle interactions and most of all pattern morphology. Our aim is to study various structures in different geometries that can arise from competition between various components. As an application, we study the two-component case in detail, since this provides a general framework for characterizing a particular phenomenon, explained in detail in Chapter 3. Recently, various theoretical growth models with two species domain boundaries or phases in competition have been studied [45, 71, 177, 178, 202, 203]. A particularly interesting set of natural examples are the experiments on microbial colonies in [69] and [112]. Competition in these systems is driven by the growth of domains into open space resulting from the motion of the domain boundaries, where these are fractal objects with power-law behaviour. These experiments show that the competitive growth of separate domains and their coarsening patterns are a universal phenomenon. In particular, the indications are that competition is vital for biodiversity and emergence of pattern formation in ecosystems [90].

We provide a detailed mathematical framework for the study of spatial fluctuations and competition leading to nucleation of possible phases in stochastic growth models. In particular, we present an exact analysis backed up with simulation data to promote a theory which can replace previous mean field studies [45, 177]. As an application we look at populations that display characteristics of spatial competition. In particular, we show that there is a strong indication that the observed segregation patterns are an emergent phenomenon which to a large extent is independent of the microscopic details.

We study the important problem in statistical physics to understand the growing mechanism of rough surfaces which contain multiple components. Our main interest is the effect of stochastic growth, competition and geometry on pattern formation. Mainly we investigate the relationship in models with radially symmetric growth and linear growth in a strip geometry, which although stems from our desire to treat the patterns encountered in biological systems [145, 218] such as the microbial colonies in [69]. These two geometries are also of practical importance, where they are used to study a wide variety of physical processes. We also generalize our study to consider general systems displaying stochastic competition within an arbitrary geometric setting. For colony growth, we focus on the case where the growth dynamics can be modelled using Eden-type clusters. A detailed explanation of the non-equilibrium Eden growth model is performed in Chapter 2. The surface of a standard Eden cluster is known to be in the Kardar-Parisi-Zhang universality class

[47, 95], this universality class is known to be very important in statistical physics which includes a wide variety of growth models. An understanding of this class is of paramount importance to our study and is also performed in Chapter 2.

In Chapter 3 under the non-equilibrium statistical mechanics framework we introduce a more realistic variation of the Eden model. Detailed events based simulations are used alongside the theoretical framework to measure the scaling exponents and the amplitude functions which are associated with the advancing fronts of microbial colonies on a hard agar substrate. Here our aim is to affirm the universality class to which the system belongs to, where we perform a qualitative comparison of the patterns produced with the ones in [69]. This qualitative analysis is performed for self-affine growing interfaces in a strip geometry, where we show that colonies with different species exhibit a universal behavior and the reported differences can be completely described by our results.

The numerical measurements shown in Chapter 3 are then followed by Chapter 4, which contains exact computations and predictions for various amplitude functions. Through a mode coupling analysis we connect the microscopic details of our growth model with the continuum theory and we show that our theoretical predictions work well with the simulation data.

In Chapter 5 we look at competition in general stochastic systems composed of particles that exhibit a range of interactions that result in scale invariant structures. We use concepts such as local scale invariance and conformal invariance to study the properties in non-equilibrium systems. In general, these powerful concepts have an ability of providing simple and unified descriptions of natural phenomenon, and can dominate behaviour in complex systems, making them analytically tractable. We study the equivalence between stochastic walkers whose motion is governed by local kinetic rules, but are embedded in a particular geometry. Using local space-time dependent symmetry we show that the behaviour and fluctuations can be elegantly captured in terms of a time dependent metric. Moreover, we provide a function which depends on the temporal coordinates of the system, and maps the statistics from one geometry onto another. This mapping depends on the local scale invariance exponent of the particles, and works directly for local interactions which do not involve a length scale, such as annihilation or coagulation of point particles. Branching or exclusion/reflection of finite size particles can also be treated after mapping the interaction length scales appropriately. In addition to describing the domain boundary growth in different geometries as mentioned above, our results are more widely applicable, including diffusion processes with time-dependent diffusion rate (i.e., temperature) [42, 114, 167, 182], in cosmologically expanding space [79],

or on a biologically growing substrate.

A rigorous derivation of some results in Chapter 5 are performed in Chapter 6. Here we present exact derivation of key formulas for the processes considered. In particular, we provide mathematical validity to mean field equations and extend previous known results to characterize processes with long range correlations.

In Chapter 7 the overall theory developed throughout the thesis is used to study radially growing microbial populations. Here we show that a complete understanding of such systems can be attained through looking at the analogous growth in a strip. In general, our results provide a substantial contribution towards uncovering the interplay between stochastic competition and spatial expansion and their effect on coexistence and biodiversity. Our approach to describe spatially expanding systems has not been used in this context before, and we believe that it can also be generalized to other non-equilibrium growth models.

Chapter 2

Non-equilibrium growth

Surface growth is a great topic of scientific interest in statistical physics, due to the self-similarity and universality emerging from dynamical local processes in a wide variety of different systems. This phenomenon therefore covers many technological and practical applications, examples include crystal growth [38, 125], epitaxial deposition [78], bacterial colony formation [84, 108, 204], propagation of burning fronts [17, 122] and fluid motion in a porous media [19, 82, 161]. It is thus a very important problem to understand the mechanisms leading to such surfaces.

Typically due to the stochastic nature of growth, the interface exhibits a rough morphology and the understanding of this is an active field of non-equilibrium statistical mechanics and irreversible growth phenomena [52, 96, 205]. Surface roughening is seen to occur in many physical problems of practical interest, ranging from crystal-growth and deposition processes [195], to two-phase flow in porous media [82]. Hence a deeper understanding of surface roughening can be expected to benefit many applied sciences.

The field of statistical mechanics offers a wide range of powerful tools for extracting the dynamical properties that is related to the growth of structures with rough surfaces. Of these tools one of the most important is dynamic scaling analysis based on concepts that arise in the field of stochastic processes [84]. In principle for a large number of systems, the evolution and dynamics of the interface can be characterized by a set of scaling exponents [17, 132]. These scaling exponents result from the scale invariant properties of certain physical quantities and are α , the roughness exponent characterizing the saturated interface roughness and acts as a quantitative measure of the fluctuations of the interface, it also sometimes referred to as the Holder exponent or self-affine exponent [17]. The exponent β known as the growth exponent, characterizes the time dependent dynamics of the roughening

process and $z = \alpha/\beta$, the dynamic exponent, related to the saturation time of the surface and the spread of correlations [84, 142, 205].

In general the evaluation of these scaling exponents is firmly based on modern statistical mechanics. For a large number of rough condensed phases many measurable quantities are seen to obey scaling relations. For example, the dynamical kinetic roughening process can be described by the interface roughness, which is defined as the root mean squared fluctuations of the surface and denoted as $S(t)$ (2.12), this is seen to increase as a power law with time, $S(t) \sim t^\beta$. The roughness will usually saturate at a value that will increase with a power-law of system size L , where $S(L) \sim L^\alpha$. The scaling properties of many surfaces have been investigated by means of both numerical and experimental techniques [195, 205, 207]. Scaling is seen as a universal tool with surprising power of prediction, where simple measurements in complicated systems allow us to capture the inherent behaviour. Through studying scaling relations, and inferring the values of scaling exponents, this approach permits the deduction of the likely universality class that a growth process belongs to [17].

The universality class is a concept which codifies the fact that for certain physical processes there are only a few essential details which will determine the behaviour. Surprisingly different systems which although appear to have no connection are found to behave quantitatively similarly [17]. Thus for a large number of systems, the values of the exponents seem to be independent of many factors characterizing their details. For example, the values of α and β do not depend on whether we look at a microbial colony or a directed polymer in a random media [84, 96]. In fact, the scaling behaviour and the surface distribution of bacteria colonies seems to be the same as those measured for the burning front of a sheet of paper, despite the obvious differences in the growth mechanism [122, 155].

For many systems, it is known that their asymptotic coarse-grained dynamics can be described by a continuum stochastic differential equation [48, 95]. These equations allow us to understand the behaviour of a growth process on a macroscopic level through the combination of deterministic terms and noise. For many systems, randomness or dynamical noise is an inherent component of the equation of motion. The effect of randomness is an aspect which makes growth processes both interesting and difficult. Where the noisy local fluctuations lead to the dynamics of the interface displaying scale-invariant behaviour and is a process which is responsible for producing kinetic roughening, a property which seems to play an essential role in shaping the morphology of the interface [117].

The origin of randomness depends on the process being studied. In growth

processes, there is a fluctuating nature of advancing flux, i.e. locally the surface grows at random positions and at random times. Here the presence of noise generally leads to the emergence of dynamics and behaviour which require novel treatments. Current techniques revolve around dealing with stochastic partial differential equations, examples which are widespread in nature are dynamics which usually evolve subject to gravitational forces, dissipative forces and a fluctuating drive, all of which can be conveniently expressed by a Langevin type equation [8, 62]. These equations typically describe the surface at large length scales, so we neglect short length scales details such as interactions between components and only consider the mesoscopic coarse-grained properties [17]. In this context, one of the most important concepts is the Kardar-Parisi-Zhang equation and universality class.

2.1 KPZ universality class

Following the seminal work of Kardar, Parisi, and Zhang (KPZ), the kinetic roughening phenomenon of many stochastic interfaces has sparked a tremendous amount of interest in the statistical mechanics community [40, 52, 95, 117]. The KPZ framework has led to a deeper understanding of a broad range of complex structures which arise in the field of non-equilibrium statistical mechanics (see [17, 142] for more details). The KPZ universality class aggregates a large portion of observed interface dynamics, for instance bacterial colony growth, burning fronts and turbulent fluids are all believed to be described by the KPZ class [22, 47, 122]. Scientist from the field of classical statistical mechanics have also been attracted to the area, since there exists a direct connection between driven interfaces and disordered equilibrium systems such as directed polymers in a random medium [96, 101, 117]. The KPZ behaviour has been observed in a large number of theoretical models [55, 139, 201] and in a few experimental systems [84, 195]. All these studies have led to the development of a wealthy inventory of powerful and innovative methods which can be used to analyze and understand KPZ surfaces (see [40] for a recent review).

2.1.1 KPZ equation

One particular important system in the KPZ class is the Kardar-Parisi-Zhang (KPZ) equation, which was introduced to describe the coarse-grained mesoscopic evolution of a rough surface, growing under the deposition of particles.

According to Kardar, Parisi, and Zhang [95], the local height position $y(x, t)$ of an interface in $d + 1$ dimensions, i.e. $x \in \mathbb{R}^d$ and $t > 0$, consist of four main

contributions

$$\partial_t y = v_0 + \frac{\lambda}{2}(\nabla y)^2 + \nu \Delta y + \sqrt{D}\eta(x, t). \quad (2.1)$$

The first two terms on the right-hand side arise from a gradient expansion of the macroscopic inclination-dependent growth rate [95, 117]. The last two terms describe the microscopic dynamics, where the Laplacian with $\nu > 0$ corresponds to a smoothing mechanism and the fluctuations $\eta(x, t)$ are described by space-time white noise which is Gaussian distributed, with zero mean and covariance

$$\langle \eta(x, t) \eta(x', t') \rangle = \delta(x - x') \delta(t - t').$$

The surface $y(x, t)$ governed by Eq. (2.1) produces a self-affine interface. An object is said to be self-affine if a small part of it looks the same as the whole after this part has been expanded in an anisotropic way. E.g. if the fractal is embedded in two dimensions, this matching can be achieved by rescaling the size horizontally and vertically by different factors. Formally, if an object has coordinates $P = (x_1, x_2, \dots)$ then an anisotropic scaling is $bP := (b_1 x_1, b_2 x_2, \dots)$ and a self-affine object is invariant under this transformation, for a particular chosen $b = (b_1, \dots, b_n)$ and $b_i > 0$, i.e. the object is given by the same equation in coordinates P and bP [17]. For surface growth, the height $y(x, t)$ of an interface is self-affine if the function is invariant under the following self-affine transformation

$$\begin{aligned} x &\rightarrow x' = bx \\ t &\rightarrow t' = b^z t \\ y &\rightarrow y' = b^\alpha y \end{aligned} \quad (2.2)$$

where (α, β, z) are as defined above.

In $1 + 1$ dimensions the KPZ class is uniquely determined by the values

$$\boxed{\alpha = 1/2, \quad \beta = 1/3 \quad \text{and} \quad z = 3/2.} \quad (2.3)$$

The $1 + 1$ dimensional KPZ equation is capable of explaining not just the values of the exponents but also the scaling functions and surface distribution for several surface growth models such as Eden, ballistic deposition and solid-on-solid models [14, 40, 47, 55, 116, 139, 150], and these models are said to be the discrete versions of the continuum theory (2.1). In higher dimensionality the scaling behaviour and universality class is much less clear [100, 119].

The ballistic deposition is probably the most studied growth model in the KPZ class, it is a very basic model with simple prescriptions that lead to a non-equilibrium interface [17, 52, 116, 139, 150]. Here, particles rain down onto a dynamically growing rough surface, and latch onto the first point on the surface they

touch. For this growth model a direct connection to the continuum equation can be established through a limiting procedure, where on coarse-grained scales the hydrodynamic modes of the rough surface can be described by a long-wavelength expansion. The cellular automata that give rise to the ballistic model can then be transformed through a limiting procedure into an integrable difference-difference equation. This, with a combination of perturbation methods on the microscopic prescriptions, can be reduced to the KPZ equation (2.1) through the Burgers equation [150].

The KPZ equation can be mapped to a number of other surface growth models. The so-called Hopf-Cole transformation ($u = \log(y)$ see [14]) maps the KPZ interface $y(x, t)$ into a directed polymer diffusion equation driven by a multiplicative noise [96]. Whereas, the Burgers equation describing the evolution of a vorticity-free velocity field $u(x, t)$ can be mapped onto the KPZ equation by taking the transformation $u = -\nabla y$ [143]. Also, the Kuramoto-Sivashinsky equation [174]

$$\frac{\partial y}{\partial t} = -\Delta y(x, t) - \nabla^4 y(x, t) + \frac{1}{2}(\nabla y(x, t))^2,$$

has the same large spatial scale, long time behavior as the KPZ equation [143].

2.1.2 Connections to Edward Wilkinson universality class

The KPZ equation is the simplest equation which describes a fluctuating interface that is undergoing lateral growth. When the lateral growth term is removed i.e. $\lambda = 0$, the universality class changes and the resulting linear equation for the $d + 1$ dimensional interface reads

$$\frac{\partial y}{\partial t} = v_0 + \nu \Delta y(x, t) + \sqrt{D} \eta(x, t). \quad (2.4)$$

This equation is called the Edward Wilkinson (EW) equation and describes the surfaces properties and displacement of the class of models known to belong to the Edward Wilkinson universality class [48]. This universality class contains surface growth models such as random deposition with surface relaxation and solid on solid models with a particular set of parameters [51, 102]. In the random deposition with surface relaxation, particles rain down onto a growing surface from a random position. Once they land on the aggregate they perform a diffusive walk up to a finite distance and stick to the surface at a point with the lowest height. Therefore a newly arrived particle will compare the local heights before deciding where to settle [17]. As a direct result of this relaxation rule, this produces a surface which is smoother compared to those models without relaxation. As with the KPZ universality class,

the scaling properties of the EW class are determined by a unique set of exponents. Using the self-affine transformation (2.2), a scaling analysis of (2.4) with $v_0 = 0$, gives the following

$$\frac{\partial y}{\partial t} = b^{z-2}\nu\frac{\partial^2 y}{\partial x^2} + b^{-d/2+z/2-\alpha}\sqrt{D}\eta(x,t)$$

and in order for the equation to be invariant under the transformation, the right hand side must be independent of the parameter b . This leads to equating the powers of b to zero and gives the following

$$\alpha = \frac{2-d}{2}, \quad \beta = \frac{2-d}{4}, \quad z = 2, \quad (2.5)$$

which for $d = 1$ lead to different values compared to (2.3).

The crucial ingredient introduced in the KPZ equation (2.1) and not present in the corresponding linear counterpart (2.4), is a non-linear term which takes into account the fact that the interface grows locally normal to the surface. In particular the KPZ equation can be thought of an extension to the EW equation with the inclusion of non-linear terms in order to explain the lateral growth phenomenon observed in a variety models [62, 95]. It is therefore necessary to look at the terms of (2.4) in greater detail to see how they relate to the growth dynamics. The parameter $\nu > 0$ is known as the surface tension and the term $\nu\Delta y(x,t)$ will act to smoothen the interface. This can be seen through the following: Consider an interface $y(x,t)$ in 1 + 1 dimensions governed by Eq. (2.4), then in a small time interval $[t, t + \delta t]$ we have

$$y(x, t + \delta t) = y(x, t) + \delta t v_0 + \delta t \nu \frac{\partial^2 y(x, t)}{\partial x^2},$$

where for the moment we have neglected the stochastic noise. Presuming $y(x, t)$ is locally concave in a small interval $(x - \epsilon, x + \epsilon)$, at the local maximum x the term

$$\nu \frac{\partial^2 y(x, t)}{\partial x^2} < 0$$

so that $y(x, t + \delta t) < y(x, t) + \delta t v_0$. This leads to a smoothing effect which reduces the irregularities of the interface compared to the average height increase [17]. For example in the random deposition with surface relaxation model, a newly arriving particle that creates a bump is re-distributed to other parts of the surface through the mechanism of surface diffusion.

If we apply the expectation operator on (2.4), we have

$$\frac{\partial \langle y \rangle}{\partial t} = \langle v_0 \rangle + \langle \nu \Delta y(x, t) \rangle + \langle \sqrt{D} \eta(x, t) \rangle.$$

Since $\langle \eta(x, t) \rangle = 0$ and by imposing periodic boundary conditions at the edges of the domain we have $\langle \nu \Delta y(x, t) \rangle = 0$, the average velocity is then

$$\frac{\partial \langle y \rangle}{\partial t} = v_0.$$

The uniform nature of the velocity will not affect the scaling properties of the interface. Since by viewing the interface from a system of coordinates that move with velocity v_0 and performing a change of variables $y \rightarrow y' = y + v_0 t$, one can effectively set $v_0 = 0$.

2.1.3 Lateral growth

In order to describe growth models such as the ballistic deposition and Eden model mentioned above, Kardar, Parisi and Zhang proposed Eq. (2.1) as an extension to the EW equation (2.4) to include terms which take into account the mechanism of lateral growth [95]. The resulting equation is valid only in the small gradient approximation i.e. in the limit $|\nabla y| \ll 1$. This approximation is consistent with the requirement on the roughness exponent that $\alpha < 1$, since for a self-affine surface we have $\delta y \sim (\delta x)^\alpha$. This means that local slopes $\delta y / \delta x \sim (\delta x)^{\alpha-1}$ decrease as we increase the size δx of the chosen domain.

A common source of lateral growth in many models such as Eden and ballistic deposition is that the surface tends to grow locally normal to the interface. One can envision adding a new particle to an aggregate in the direction that is locally normal to the interface, this leads to a gradient expansion [17, 95]. Since growth occurs locally normal, in a time interval $[t, t + \delta t]$, we generate an increase by δy along the y -axis, which by Pythagoras theorem gives

$$\delta y = ((v\delta t)^2 + (v\delta t \nabla y)^2)^{1/2}, \quad (2.6)$$

with the requirement that $|\nabla y| \ll 1$, expanding (2.6) gives

$$\delta y \approx v\delta t \left(1 + \frac{1}{2}(\nabla y)^2 + \dots\right),$$

the term generated leads to the interface equation

$$\frac{\partial y(x, t)}{\partial t} = v + \frac{v}{2}(\nabla y)^2 + \dots$$

This physical argument suggests to add an additional term to (2.4) which describes the lateral growth mechanism and is proportional to $(\nabla y)^2$, leading to the KPZ equation (2.1).

For certain physical processes, an alternative method to derive a growth equation is to exploit the physical symmetries present in the system. In most systems, the symmetries that exist have the same scaling properties as the continuum equation. Therefore the symmetry principles can lead to determining which terms to include in the equation of motion. The KPZ equation (2.1) is the simplest growth equation that breaks the up/down symmetry i.e.

$$y \rightarrow -y.$$

The source of this symmetry breaking is known to be the existence of a driving force which cannot be transformed away. This force acts in the perpendicular direction to the interface and leads to determining the direction of growth. For models in the KPZ class, this symmetry breaking is due to the presence of lateral growth, which leads to the inclusion of terms such as $(\nabla y)^{2k}$, $k \in \mathbb{N}$ in the growth equation. The lowest order term of this sort is obviously $(\nabla y)^2$ which if added to (2.4) leads to the (2.1). Note the terms $(\nabla y)^{2k}$, $k \geq 2$ are usually not included since we assume that $|\nabla y| \ll 1$ and in the large scale limit the term $(\nabla y)^2$ will dominate the rest [17, 142].

We can also consider a geometrical interpretation of the non-linear term. Suppose at time t the interface $y(x, t)$ is governed by Eq. (2.1), at time $t + \delta t$ the height of the interface is

$$y(x, t + \delta t) = y(x, t) + \delta t \frac{\lambda}{2} (\nabla y)^2,$$

where for now we neglect the contribution from the Laplacian, the additive term and the noise. Since for all $x \in \mathbb{R}^d$ we have $(\nabla y)^2 \geq 0$, this term will therefore generate an increase in the local height of the interface by the addition of material if $\lambda > 0$ or a decrease in the interface by removing material if $\lambda < 0$. This is in contrast to the Laplacian term, which re-organizes the interface height such that the total mass remains unchanged [17]. Thus the non-linear term for $\lambda > 0$ increases the height of the interface, where more material is added to parts with a larger local slope, this will lead to the average velocity of the interface increasing even when $v_0 = 0$. Therefore, the material added by the non-linear term can be seen to generate an excess velocity, where the mean velocity of an interface governed by Eq. (2.1) is given by

$$v_\infty = v_0 + \frac{\lambda}{2} \langle (\nabla y)^2 \rangle \quad (2.7)$$

and in general will be non-zero for a non-flat interface.

2.1.4 Scaling arguments

The non-linear term in the KPZ equation is responsible for a phase transition from one universality class to another, and should lead to a correct prediction for scaling exponents. These can be easily observed numerically for growth models and take values as in (2.3). As illustrated above for the EW equation (2.4), the values of the scaling exponents were obtained using the transformation (2.2), and here we replicate the approach for the KPZ equation. Under the self-affine transformation (2.2) the equation (2.1) with $v_0 = 0$ becomes

$$\frac{\partial y}{\partial t} = \nu b^{z-2} \nabla^2 y + \frac{\lambda}{2} b^{\alpha+z-2} (\nabla y)^2 + b^{-d/2+z/2-\alpha} \sqrt{D} \eta,$$

again to insure scale invariance the right hand side has to be independent of the parameter b . By equating the powers of b to zero, this procedure however leads to three scaling relations for two exponents, namely, α and z . To proceed forward one can argue for KPZ models the non-linear term is the most important since it generates lateral growth, therefore this term should dominate over the Laplacian. This leads to the following relations: $\alpha = (2-d)/3$ and $\beta = (2-d)/(4+d)$, and in $d = 1$ we have

$$\alpha = 1/3 \quad \text{and} \quad \beta = 1/5,$$

which clearly differ from the measured values of the exponents given in (2.3). The reason the scaling argument method does not provide us with a correct set of values for the exponents is that under rescaling the system, the terms (ν, λ, D) in the equation do not renormalize independently, since they are coupled to each other [96]. So in order to have scale invariance, we cannot simply equate the exponents of b to zero, as the coefficients (ν, λ, D) also change under rescaling [17, 95].

In order to obtain the values of the scaling exponents via scaling arguments, we use Galilean invariance and by mapping to the Burgers equation this leads to a scaling relation between two independent exponents. Further, we use information known for the stationary solution of Eq. (2.1) and this will give us the roughness exponent α in one dimension [17, 215]. The noisy Burgers equation for a vorticity free velocity field $v(x, t)$ is

$$\frac{\partial v}{\partial t} + \lambda(v \cdot \nabla)v = \nu \nabla^2 v - \nabla \eta, \tag{2.8}$$

where ν is the viscosity and $\nabla \eta(x, t)$ is the random force. The noisy Burgers equation can be mapped to the KPZ equation through the change of variables

$$v = -\nabla y, \tag{2.9}$$

and because of this transformation, the Burgers equation belongs to the KPZ universality class and has the same scaling exponents. The left hand side of (2.8) originates from the total derivative

$$\frac{Dv}{Dt} = \frac{\partial v}{\partial t} + \lambda(v \cdot \nabla)v,$$

where after rescaling with (2.2) we expect this total derivative to remain unchanged. This leads to the rescaled prefactor $\bar{\lambda} = b^{\alpha+z-2}\lambda$ remaining unchanged so that $\bar{\lambda} = \lambda$ [17, 143]. So the coefficient of the non-linear term in the rescaled KPZ equation also remains unchanged and the relation

$$\alpha + z = 2$$

is expected to hold. This relationship is a connection between the two unknown exponents α and $z = \alpha/\beta$ and this characteristic relationship of growth is valid in all spatial dimensions $d > 0$.

This relation is also a consequence of a symmetry for the KPZ equation known as Galilean invariance. This arises from the microscopic dynamics of the interface formation i.e. the lateral growth rule, and corresponds to the law of physics remaining unchanged. The Burgers equation is invariant under the Galilean transformation and this results in an invariance under tilting of the KPZ interface by an infinitesimal angle θ , the transformation is

$$\begin{aligned} y' &= y + \theta x \\ x' &= x - \lambda \theta t \\ t' &= t. \end{aligned} \tag{2.10}$$

The tilted KPZ equation satisfies

$$\frac{\partial y'(x', t')}{\partial t'} = \nu \nabla^2 y' + \frac{\lambda}{2} (\nabla y')^2 + \sqrt{D} \eta(x' + \lambda \theta t', t'),$$

this displays Galilean invariance since the uncorrelated noise is invariant as well [17]. Applying the transformation (2.2) to the tilted equation with coordinates (x', t', y') and to the non-tilted equation with coordinates (x, t, y) leads to

$$\begin{aligned} y' &= y + \theta b^{1-\alpha} x \\ x' &= x - \lambda \theta b^{z-1} t \\ t' &= t, \end{aligned} \tag{2.11}$$

using the coordinate transformation (2.11) in Eq (2.1) leads to a condition $\alpha + z = 2$ being required for Galilean invariance [143, 215].

It is known that the exact solution for the stationary state of a KPZ equation in $1 + 1$ dimensions is a Brownian motion [86]. A Brownian motion has a roughness exponent $1/2$ and this will characterize the fluctuations of $y(x, t)$ for $t \gg L^z$. Since the saturated interface has a roughness exponent α , we thus have

$$\alpha = 1/2, \quad z = 2 - \alpha = 3/2 \quad \text{and} \quad \beta = \alpha/z = 1/3.$$

These values are consistent with the measured exponents for $1 + 1$ dimensional models in the KPZ class.

2.1.5 Exactly solvable models in the KPZ class

The universality class for the surface dynamics of a particular model can be inferred mainly from measuring the scaling properties of the surface fluctuations by means of scaling exponents [51]. However, there exists a number of other universal quantities that are also suitable for determining the class of a surface. Examples include the stationary distributions of the global interface width and the extremal height [7, 55], and the distribution of the height during the transient regime that's prior to saturation of the interface [40]. Both flat and radial KPZ growth models have been subject to recent analytical and experimental investigations [55, 195]. These agree with the conjecture in [181], where interface-fluctuations in systems belonging to the KPZ universality class are described by well-known universal distributions in random matrix theory [10, 157]. In $1 + 1$ dimension for a particular set of models proposed to be in the KPZ class the distributions during the transient growth regime have been computed exactly. For example the limiting solution of the height distribution $y(x, t)$ of a particular set of single step solid on solid models [100] has been determined analytically in [91]. Another relevant example is the surface $y(x, t)$ of the polynuclear growth model, where in [165] the Airy process (with distribution governed by the Painlevé II equation) was found to be the limiting process describing the surface fluctuations. Furthermore, the one-point fluctuations of the growing KPZ interface can be expressed as

$$y(0, t) \simeq v_\infty t + \left(\left(\frac{D}{2\nu} \right)^2 \lambda t \right)^{1/3} \zeta,$$

where ζ is the random amplitude dependent on the geometry of growth. For linear growth where the initial interface starts from a flat line of seeds, the law of ζ is the Gaussian orthogonal ensemble (GOE) Tracy-Widom distribution, which governs the largest eigenvalue distribution of real symmetric matrix [10, 55, 157]. On the other hand, growth from a single seed which also represents radial growth leads to ζ having a Gaussian Unitary Ensemble (GUE) Tracy-Widom distribution, this governs

the distribution of the largest eigenvalue for complex Hermitian random matrices [10, 55, 181]. Full descriptions of the properties of the Tracy-Widom distribution for the largest eigenvalues of GUE and GOE can be found in [10]. The solution of the $1+1$ dimensional KPZ equation with an initial condition that induces the growth of curved surfaces has also been found, where the limit for the radius fluctuations is the GUE distribution and the analytical results have subsequently been corroborated through a numerical evaluation [181].

Experimentally, the GOE and GUE distributions have also been observed, for example in the slow combustion of paper sheets [122]. Where the surface of a burning front that evolved from a flat initial condition was seen to be in agreement with the GOE case. Also a recent experiment on growing interfaces of liquid crystal turbulence allowed the investigation of an isotropically growing radial and flat surfaces [195]. It was shown that these surfaces belong to the KPZ universality class, where the interface position exhibited agreement with GUE or GOE distributions, and the cumulants from second to fourth order also matched.

Thus, from theoretical and experimental studies, the GUE and GOE are universal features of the KPZ class. Where they describe the distributions of the interface position in one-dimensional growth from flat and radial seed.

2.2 Eden model

In 1961, Eden introduced a lattice based stochastic growth model, which over the years has been used to investigate many processes, such as epidemics, tumor growths and percolation theory and henceforth has become a standard growth model for describing the propagation of rough surfaces [47, 52, 108]. The Eden model is one of the simplest growth models, and is generally considered as a prototype reference to describe cluster growth and aggregation phenomena, with many potential applications in physics, chemistry and biology [119, 194] including the formation of cell colonies such as bacteria and tissue cultures [84, 155]. The original model was introduced on a regular square lattice. The growth mechanism begins with a seed particle at the origin, and subsequently at each iteration an identical particle is added to the cluster on a uniformly chosen empty site next to the cluster. Such a prescription generates a compact cluster of cells with a random perimeter.

The kinetic rules of the Eden model can be captured by a constant source of randomness, which emerges from the local growth rules and drives the interface forward. This generates lateral growth and leads to Galilean invariance, and places the Eden model in the KPZ universality class along with the other models mentioned

above [7, 92, 119].

2.2.1 Lattice models

There exists three well known versions of the lattice based Eden model labelled A, B and C, which differ in the microscopic rule of choosing the growing sites [17, 67, 92]. These differ only on the short-range scale and different versions exhibit different finite size corrections. In version A, all unoccupied sites adjacent to the surface are assigned the same probability and one site is chosen at random to add a new particle. The surface of this version contains a great number of small holes which artificially increases the interface roughness. Due to this, the version is known to have poor convergence [139]. The original model introduced by Eden is known as version B [47]. Here the growth prescriptions involves considering all open bonds with equal probability, where open bonds are defined as those that join an occupied site to an unoccupied site. In version C, all occupied sites of the surface with empty neighbours are assigned the same probability to produce an offspring. Then at each time step one of these sites is chosen at random and a new particle is added on any of the nearest-neighbour empty sites with equal probability. Version C is known to have good scaling properties and is the most biologically relevant for studying the formation of microbial colonies driven by mitosis [84]. These three versions can be shown to be effectively different, by considering simple examples of growth in \mathbb{Z}^2 with a particular configuration of the surface and empty sites [92].

The irreversible nature of growth leads to the surface of the Eden cluster displaying a morphology with kinetic roughening. This model is therefore considered to be in the field of non-equilibrium statistical mechanics [17, 92]. One finds that the surface of the cluster becomes smoother going from model A to C. In general, scaling theory of critical phenomena tells us that for large system sizes the behaviour is independent of small length scale details. Therefore the scaling properties in each version are not affected by the differences in the growth rules. The three versions of the Eden model therefore produce interfaces that differ microscopically, but all give similar statistics for quantities such as the roughness $S(t)$, where the exponents are the same and therefore all three versions are known to belong to the KPZ universality class [17, 92, 142]. In addition, further versions of the Eden model which only differ by small modifications to the microscopic growth rules are also expected to be in the KPZ class [67].

The Eden model is known to represent a large number of stochastic growth processes described by the continuum equation (2.1). Applications for the Eden models are varied and wide ranging. They include physical processes such as sedi-

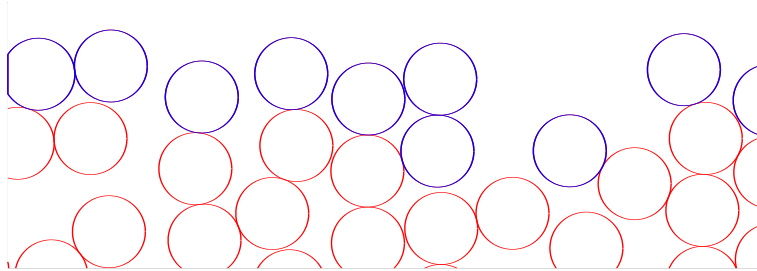


Figure 2.1: Microscopic snapshot of the off-lattice Eden model version C. Growth events result in active cells (in blue) placing a child at a random position touching their surface. The new cell position is selected such that it does not overlap with existing cells. Inactive cells (in red) are those which have no space to place a child in their neighbourhood.

mentary sandstones [31] or colloidal silicate particles [26, 98] and biological such as the morphology of cancer cells [24, 27, 67, 212]. The original model was proposed as a lattice-based representation for the development of bacterial colonies [47]. The lattice based models are very easy to simulate, but experience anisotropic growth due to the underlying lattice [210]. Due to this anisotropic behaviour numerical simulations to extract the surface properties are very cumbersome. Required convergence to the KPZ state is slow and large system sizes are needed to verify the universality class.

2.2.2 Off-lattice model

In order to overcome the anisotropy of the lattice, an off-lattice Eden model has been introduced [93, 210]. Here the cluster is composed of touching circles and the growth algorithm for the 2-dimensional off-lattice Eden model of type C follows the following prescription (illustrated in Figure 2.1). On a plane an active cell is placed, only active cells are capable of reproduction. At each time step, an active cell is selected randomly with equal probability and the range of possible directions along which an adjacent touching cell can be placed without overlapping existing cells is identified. A random direction is chosen uniformly from this permitted range and a new active cell is placed there. If no possible growth directions can be found, the cell is labelled as inactive and will subsequently no longer be considered for growth.

Several systematic studies of the surface of the the Eden model in different geometries and dimensions have been performed, as the model is well suited for

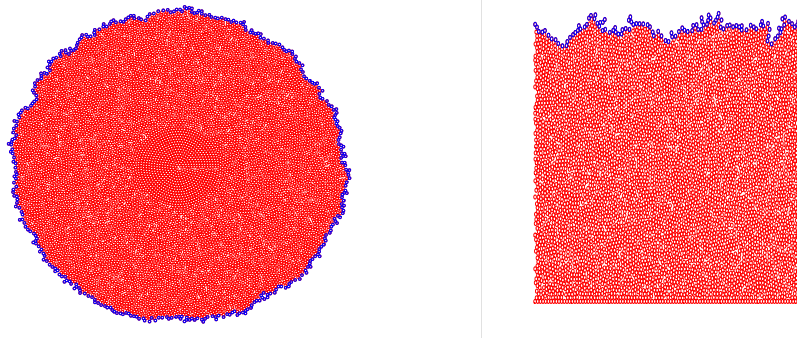


Figure 2.2: Simulations of the off-lattice Eden model. (a) Circular colony with approximately 10500 cells, an initial radius $r_0 = 15$, in units of cell diameter, and grown to a final radius of approximately 70. (b) Linear colony with approximately 5500 cells in a strip of width $L = 100$, grown to a final height of approximately 70. In each figure, cells are of diameter 1, red cells indicate the interior and blue cells indicate the colony surface.

finite-size scaling analysis [92, 119]. Figure 2.2 shows examples of off-lattice Eden cluster growth from (a) circle of seeds in \mathbb{R}^2 and (b) line of seeds in a strip of size L with periodic boundary conditions. The populations contain approximately 10500 and 5500 cells respectively. Active cells are marked in blue and exist mostly only on the cluster boundary called the surface. We see that the interior cells are uniformly distributed but the surface is uneven and rough. One of the trivial aspects of an Eden model is the compact character of the resulting cluster, with a solid core that has a fractal dimension equal to the dimension of space [47, 139]. Although the interior appears quite simple, the surface is non-trivial. Simulations of the Eden model show that despite the simplistic nature of the algorithm, the surface is highly irregular, where the irreversible dynamics lead to interesting effects arising in the scaling properties of the growing interface [92]. The scaling properties of the surface show a self-affine fractal geometry [5, 6, 17, 119] and the surface of the Eden model in $1 + 1$ dimensions is consistent with the KPZ scaling relation $\alpha + z = 2$.

In order to study the interface properties, it is convenient to start growth from an entire line of seeds, instead from a single seed or circle of seeds. In two dimensions, the cluster will grow on a strip subset of \mathbb{R}^2 of length L , with periodic boundary conditions at the edges of the strip and the evolution of the fluctuations is monitored by measuring the front height fluctuations [17, 108, 119].

These fluctuations are described by the roughness of the surface, which is given by the root mean squared displacement of the surface height as a function of t [17, 142], defined as

$$S(t) := \left\langle \frac{1}{L} \int_0^L [y(x, t) - h(t)]^2 dx \right\rangle^{1/2}, \quad (2.12)$$

where the average surface height is given by

$$h(t) := \left\langle \frac{1}{L} \int_0^L y(x, t) dx \right\rangle. \quad (2.13)$$

Starting from a flat surface the value $S(t)$ is expected to increase as

$$S(t) \propto t^\beta \quad \text{for } t \ll t_s,$$

where t_s is the expected interface saturation time. The power-law increase in the roughness does not continue indefinitely but is followed by a saturation regime due to a finite size effect, where for a fixed value of L the roughness is expected to reach a saturation value

$$S(t) \propto L^\alpha \quad \text{for } t \gg t_s.$$

The emergence of this saturation regime is linked to the appearance of lateral correlations on the surface which arise due to the growth rules and lead to height fluctuations spreading in the lateral direction. Although this spread is local, however, over time the information spreads globally. The typical distance over which the surface is correlated is characterized by the lateral correlation length denoted by ξ_{\parallel} . The value of t_s depends on the size of the system where $t_s \sim L^z$, and thus by

$$S(t_s) \sim t_s^\beta = L^{z\beta} = L^\alpha$$

we have the following scaling relation $z = \alpha/\beta$. At the beginning of the process the interface is uncorrelated, during growth ξ_{\parallel} grows with time. For a finite system, ξ_{\parallel} cannot grow indefinitely and when ξ_{\parallel} reaches the size of the system, the entire interface is correlated resulting in saturation of the interface roughness. Thus at the point of saturation

$$\xi_{\parallel} \sim L \sim t_s^{1/z},$$

and the dynamical relationship $\xi_{\parallel}(t) \sim t^{1/z}$ holds for all smaller times [17]. Note that for the radial surface, the roughness scales according to $S(r_0, t) \sim t^\beta$ and due to the continuous expansion in space the surface will never saturate [119].

As growing interfaces are common in nature it is no surprise that there exist an elegant characterization of them. Family and Vicsek found an existence of a

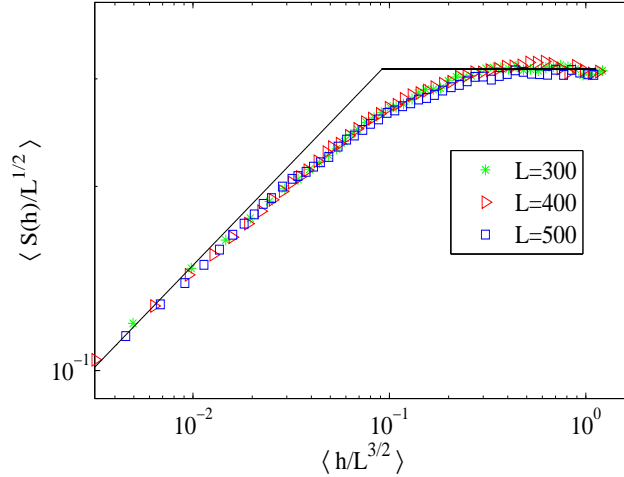


Figure 2.3: The roughness $S(t)$ for the lattice version of the Eden C model for several values of system size L and clusters growing on a strip geometry as in Figure 2.2(b). The roughness displays the correct power-law behaviour with exponents consistent with the KPZ universality class. As described in the text, the Family-Vicsek (2.14) rescaling of the axes is used to obtain a data collapse.

useful scaling for these rough interfaces [52]. The main properties of the surface $y(x, t)$ can be characterized by the Family-Vicsek scaling relation of the roughness with exponents as in (2.3) such that

$$S(t) = L^\alpha f(t/L^z) , \quad (2.14)$$

where the scaling function $f(u)$ has the property

$$f(u) \propto \begin{cases} u^\beta & u \ll 1 \\ 1 & u \gg 1 \end{cases} . \quad (2.15)$$

Such a scaling behaviour has been shown for many discrete models including ballistic deposition and continuum growth [17, 52, 84, 95, 142], and also holds for other universality classes such as Edward Wilkinson [48].

Figure 2.3 shows the behaviour of $S(t)$ for Eden clusters grown on the lattice from a line of seeds for several system sizes. The black lines indicate the expected power-law behaviour and using the Family-Vicsek (2.14) rescaling of the axes we achieve a data collapse. As described, this is consistent with the predictions from the continuous KPZ class, where the rough surface of Eden clusters are known to be

self-affine fractals and are characterised by the global roughness exponent $\alpha = 1/2$ and growth exponent $\beta = 1/3$.

2.2.3 Exact Solution of Eden models

Investigations in the radial distributions of surfaces obtained with large-scale simulations of several Eden radial clusters with different microscopic growth rules have been shown to be consistent with the KPZ interface distributions [55, 181]. The one-point radius distribution has been shown to satisfy

$$R(t) \simeq v_{\infty} t + \left(\left(\frac{D}{2\nu} \right)^2 \lambda t \right)^{1/3} \zeta,$$

where (ν, λ, D) are as in Eq. (2.1) and v_{∞} from (2.7). As one would expect the random variable ζ follows the GUE Tracy-Widom distribution for the largest eigenvalue. This is in complete agreement with the conjectures proposed for the governing behaviour of curved surfaces in the KPZ universality class. Further support of the distribution is given by measuring the cumulants, where the order $n + 1$ cumulants associated to radial distribution have also been measured to converge to the corresponding GUE cumulants [7].

2.3 Growth and pattern formation in biological systems

Pattern formation is ubiquitous in the natural world, fascinating patterns are observed in a wide range of different processes, from spatial distribution of simple single cell organisms to more complex cases such as the grazing patterns of flock of sheep [13, 53]. Recently there has been extensive investigations on the formation of patterns occurring in various fields of physics and biology [17, 195]. Some noticeable examples are systems such as alloys [170], fluids [142, 174], crystals [19], ceramics [115], polymers [12, 28], bacteria cells [136, 204], and viruses [88, 219]. Interestingly, despite fundamental differences in various systems where microscopic details differ, seemingly similar forms of patterns can be seen to emerge. Thus there should exist a universal mechanism which is largely responsible for the formation of these patterns [87].

From a statistical physics perspective, it is very important to understand the various mechanisms that govern pattern formation. One of the most intriguing questions is, how can complicated structures arise through the combination of simple interactions between the constituting components [84, 87]. In particular, the modelling of biological systems has so far been a challenge. The difficulty being the choice of model, which requires a detailed consideration of the microscopic rules. In

order to study biological systems, one must understand the underlying mechanism and should not use an arbitrary model with rules and dynamics set to reproduce data. Whereas, including all biological details can lead to unmanageable parameters, jeopardizing any potential for a theoretical understanding. It is therefore not surprising that the formation of patterns in biological systems have been given much attention from various scientific disciplines. In many cases, the emergence of the patterns is both a complex and fascinating feature [13, 136, 199].

A very good starting point is the formation of patterns in populations of simple biological objects such as single-cell organisms. These systems are composed of a vast number of cells and are found to be usually dominated purely by physical conditions [23, 105, 136, 199]. Experiments of microbial species reveal that they can display a range of colony formations which is also seen in other areas of physics [136, 155]. Although these colonies exhibit some species dependent effects, they are known to be within the rare domains of biological modelling where the combination of physical conditions and universality dominate over complicated biological mechanisms. Therefore the growth phenomena in these biological colonies can be discussed in physical terms [13, 109]. In particular, the dynamical properties in these systems can be understood by comparing the structure and interface to theoretical growth models, proposed for non-biological systems [95, 134]. Understanding pattern formation in such systems can greatly benefit the studies of more complicated patterns in biology and nature [155, 205].

There exist many advantages in using microbial species for the study of pattern formation. Firstly, one has a great deal of control over the cellular dynamics. Microbial species are known to depend sensitively on the conditions of their environment. For example, the rate of colony growth is determined by the amount of initial nutrients c_n , and the agar concentration c_a will determine the motility of the cells [123]. Investigations performed for when the petri dish is filled with hard agar shows that in this regime the cells hardly move and display no active motion, whereas on soft agar they actively move around. By controlling the cell reproduction and motion, one can therefore look at a wide variety of colony behaviour and this makes it possible to bridge non-biological and biological systems [136, 155, 199]. Another advantage is that the cell size of individual organisms is very ideal, using optical instruments the observed macroscopic growth can be related to the microscopic interactions and cellular motion. In general uncovering these relationships allow us to extract universal laws that not only govern these systems but also other more complicated systems [87, 136]. In addition, a vast number of studies exist which discern the characteristics of well known species such as *Escherichia coli*, *Saccha-*

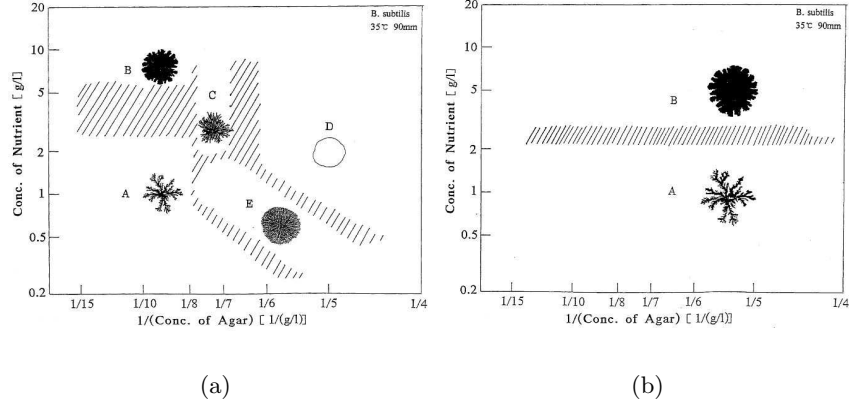


Figure 2.4: Morphological diagram of colonies expected for the bacterium *B. subtilis* grown on a petri dish. The diagrams display morphologies which also appear for various processes that belong to the field of non-equilibrium statistical mechanics. (a) The colony formation depend on the petri dish conditions such as the concentration of agar c_a and concentration of nutrients c_n . (b) Without cellular movement, the resulting structures are simple and display either Eden like or DLA like behaviour. The diagrams have been taken with permission from [155], copyright (1992) Physical Society of Japan.

romyces cerevisiae, *Salmonella typhimurium*, *Bacillus subtilis* and *Proteus mirabilis* [20, 36, 87, 99, 183, 187, 188].

In recent years there has been a thorough experimental investigation on the formation of colonies that several kinds of species can develop. These experiments are usually performed on a petri dish where a drop of solution containing cells is inoculated at the centre of the dish. In these colonies the two factors c_a and c_n are largely responsible for the development of the morphological structure and the patterns observed [136, 155, 208]. In particular complete phase diagrams have been obtained for the colonies of species such as *B. subtilis*, *P. mirabilis*, *E. coli*, *S. marcescens* [199]. These phase diagram display interesting regimes of colony growth, which include morphologies such as Diffusion limited aggregation (DLA), Dense branch morphology (DBM), Eden and perfect disks, all of which are known from non-equilibrium statistical mechanics. These growth patterns seem to be universal since they are observed across a broad range of systems. For instance, DLA, DBM and Eden are structures which are also observed for physical systems such as crystal growth [125], viscous fingering [176, 197], fluid flow on a porous media [160] and burning fronts [108, 122].

In these colonies, microscopic observations show that there exist two main distinct type of growth mechanisms (see Figure 2.4(a)). The first is without active movement of individual cells, here growth is seen to be static, leading parts of the colonies grow solely by cell division which leads to an increase in the population mass and colony area [155]. In such a region the colony is seen to form DLA and Eden like patterns. The other morphologies are only seen when there is an active movement of cells. This growth mechanism results in a constant dynamical change on microscopic length scales, where the cells appear to have a random motion. The cellular movement seems to be a mechanism which induces a morphological change. This is confirmed by carrying out experiments using immotile strains with no flagella. The phase diagram seen here are simple, where the morphological change in the colonies is reduced to DLA (low c_n) and Eden (high c_n) like patterns for all c_a , see Figure 2.4(b).

Recently there have been a number of models which have attempted to capture the morphological structure observed in the experiments of microbial colonies. The most common methods are surface growth models [108, 109, 136] and reaction diffusion based models [13, 105, 123, 214]. These models are used to describe the formation of structures on a macroscopic scale and do not capture the fundamental microscopic differences which exists between distinct species.

2.3.1 Space-limited population growth

Spatial competition is a common phenomenon in growth processes and can lead to interesting collective phenomena such as fractal geometries and pattern formation [17, 123, 136]. This is not only relevant in biological contexts such as range expansions of biological species [57, 211] or growth of micro-organisms, but as well in social contexts such as the dynamics of human settlements or urbanization [56]. These phenomena often exhibit universal features which do not depend on the details of the particular application, and have been studied extensively in the physics literature [12, 17, 19, 136, 142].

The main application of the results in this thesis is to investigate spatial competition in the growth of microbes on two dimensional geometries as shown in Figure 2.5, for which recently there have been several quantitative and experimental studies [71, 69, 112, 111]. In general, the growth patterns can be influenced by many factors, such as size, shape and motility of the individual organism [207], as well as environmental conditions such as distribution of resources and geometric constraints [155, 198], which in turn influence the proliferation rate or motility of the organisms [199]. We will focus on cases where active motion of the individuals

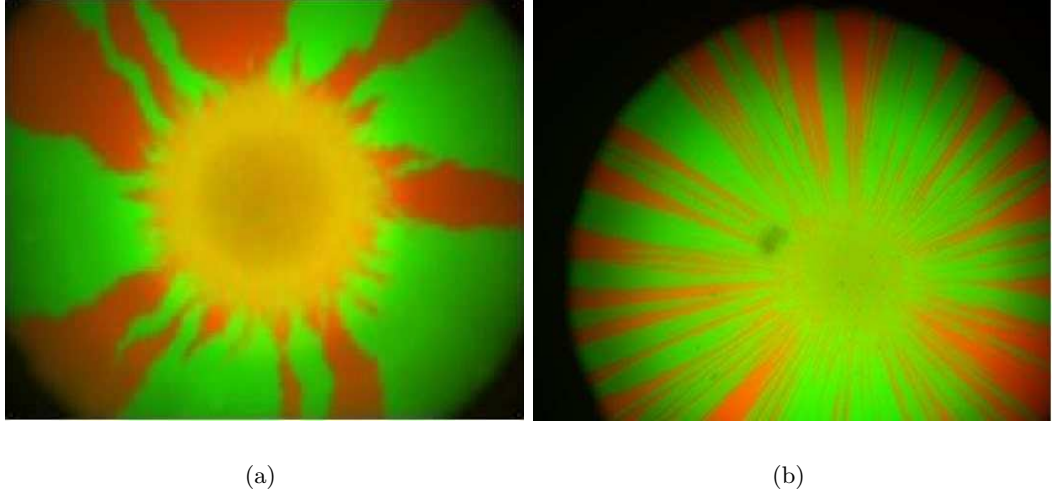


Figure 2.5: Fluorescent images of colonies of (a) *E. coli* and (b) *S. cerevisiae*. The scaling properties of both patterns are believed to be in the KPZ universality class, and the differences are due to microscopic details of the mode of reproduction and shape of the micro-organisms. The images have been taken with permission from [69], copyright (2007) National Academy of Sciences, USA.

can be neglected on the timescale of growth, which leads to static patterns and is also a relevant regime for range expansions. We further assume that there is no shortage of resources, where growth and competition of species is purely space limited and spatially homogeneous. This situation can be studied with colonies of immotile microbial species grown under precisely controlled conditions on petri dish with hard agar and rich growth medium. In this regime, the stochastic local multiplication of cells governs the development of a colony [205].

Under these conditions one expects the colony to form compact Eden-type clusters, which has recently been shown for various species including *S. cerevisiae*, *E. coli*, *B. subtilis* and *S. marcescens* [69, 155].

Due to the similarities between the clusters and patterns that emerge from the Eden model and microbial colonies, KPZ has been suggested as the universality class that describes colony growth. In recent detailed studies of *E. coli* and *S. cerevisiae* [5, 69, 71] quantitative evidence for the KPZ scaling of growth patterns has been identified. Figure 2.5 shows two fluorescent images of microbial populations in an increasing radial geometry taken from [69]. Here we can see striking differences in colony patterns for immotile *E. coli* and *S. cerevisiae* at the end of a growth

period of four days. For both species the microbial populations are made of two strains, which are genetically identical except for having different fluorescent labeling. Reproduction is asexual, and the fluorescent label carries over to the offspring. Although at the beginning of the experiments the strains are well mixed, during growth rough sector shaped segregated regions develop.

Compactness within the initial habitat and the use of immotile cells leads to the populations evolving only at the leading edge. As the colony grows, cells that are squeezed out of the colonization front no longer participate in the colonization process. From the initial well mixed population, sectors of single gene alleles emerge which compete for space and grow at the cost of those left behind and can either expand or lose contact to the population front. This drives a coarsening process, which leads to a gradual decrease in the number of sectors and is a consequence of genetic drift acting at the leading edge of the range expansion [70]. In the framework of this thesis, the domain coarsening process can be understood through the fluctuating path of the boundaries separating neighbouring sectors. A domain can be seen to be “dead” and no longer contributes to growth when the leading ends of its boundaries meet and annihilate. The sectors surviving this annihilation process grow in size at the cost of those left behind, and appear to surf on the wave front [70, 107].

A quantitative model and analysis of sector boundaries has been presented in [71, 111], where the assumption is made that the fluctuations of the motion taken by the leading tip of the domain boundary are diffusive. However, the authors also discuss that this idealization is not quite correct, since already in [69] the mean squared displacement of the sector boundaries was estimated from experimental data to grow superdiffusively. This superdiffusive behaviour can be attributed to the roughness of the population front, following works on competition interfaces [177] for rough surfaces in the KPZ universality class. Since the experiment uses immotile strains on hard agar, there is no noticeable change in the population behind the expanding front. Therefore Figure 2.5 provides a frozen record of the domain competition and coarsening process during colonization.

For *S. cerevisiae* the colony patterns share similar qualitative behaviour with the *E. coli* population. However, the domain boundaries are less rough compared to *E. coli*, leading to a finer pattern and a larger number of sectors. This behaviour can be attributed to the microscopic differences between *E. coli* and *S. cerevisiae*, where amongst other characteristics, noticeably, cell shape and reproduction time statistics are distinct [36, 183]. A dynamic scaling procedure undertaken by the authors shows that consistent with the morphological behaviour expected in Figure 2.2 we have

here Eden-like behaviour for both colonies.

In recent years the growth phenomena of random patterns have been studied extensively. Many growth models have been introduced to describe the patterns observed, many of which lie in the field of non-equilibrium statistical mechanics. Regardless of the complexity of colony formation, there exists basic mechanisms which determine the behaviour of their surface. Motivated by the universality of growth phenomena, in Chapter 3 we study the formation of the patterns seen in Figure 2.5. We will show that these patterns can be described by stochastic competition between domain boundaries, which can be discussed in terms of interacting particle systems. Our goal here is to relate the observed macroscopic growth of colony patterns to the main microscopic factors which govern the formation of the patterns observed. We exploit the fact that the global scaling behaviour of the interface is independent of the details which characterize the development on smaller length scale. In particular, by adapting the classical Eden model to include a similar geometrical background and cellular automaton rules as in the experiments, we show that it is possible to reproduce the patterns not just seen in Figure 2.5 but also for other microbial colonies, as can be found in [112]. We mainly focus on growth in a linear geometry, which allows us to perform a scaling analysis and monitor the scaling properties and interface fluctuations very effectively. Further connections to radially growing clusters are made in Chapter 7.

Chapter 3

Segregation patterns in growing populations

3.1 Introduction

In this chapter we investigate the spatial distribution of microbial populations. We intend to use the non-equilibrium statistical mechanics framework of KPZ and Eden growth, both introduced in the previous chapter to discuss the patterns seen in Figure 2.5 and in [112]. The goal is to understand the formation of such segregation patterns through purely a space-limited population growth with competing strains. The patterns can also be seen in Figure 3.1, indicating that the behaviour is independent of the growth geometry. Here the petri dish is initialized by touching it with a razor blade wetted by a liquid mixed culture containing fluorescently labeled cells. Due to the geometry, the colony is seen to expand vertically with height, and displays segregation behaviour similar to the radially growing colony. The qualitative emergence of these segregation patterns and connections to annihilating diffusions has been studied in [5, 69, 71, 111, 158]. However, the models used in these studies ignored all microscopic details of reproduction, such as anisotropy of cells [190] or reproduction time, and therefore could not explain or predict the differences observed for different species. A simple modification of the lattice based Eden model made in [5] shows that this Markovian model is capable of providing a good reproduction of the basic features of the *E. coli* experiments on a large scale, such as the KPZ behaviour, see Figure 3.2. This is a clear indication that segregation itself is an emergent phenomenon in these populations.

In general, we believe the differences in the colonies of *E. coli* and *S. cerevisiae* (as can be seen in Figure 2.5 and Figure 3.1) are a consequence of the differences

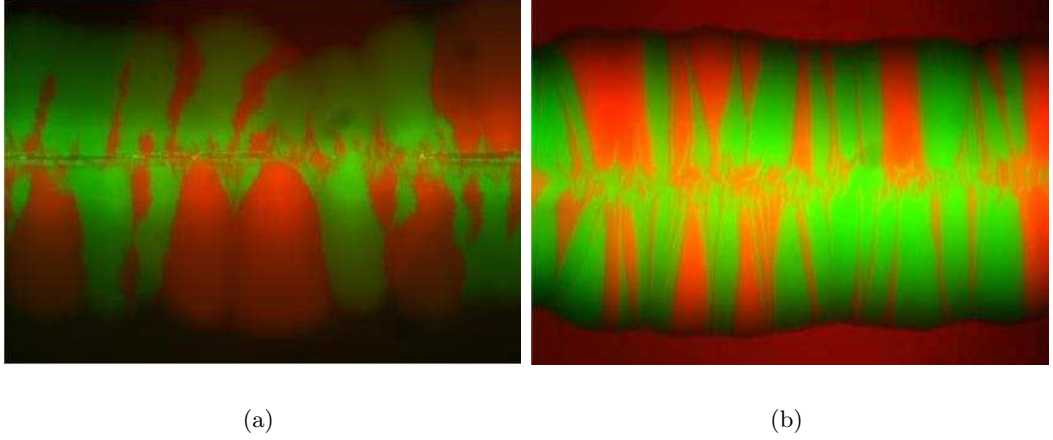


Figure 3.1: Fluorescent images of colonies of (a) *E. coli* and (b) *S. cerevisiae*. Linear experiments performed by touching a petri dish with a razor blade containing a mixture of cells. The colony then expands vertically as a function of height with the same features and patterns as in Figure 2.5. The images have been taken with permission from [69], copyright (2007) National Academy of Sciences, USA.

in the mode of reproduction and shapes of the microbes, which introduce local correlations that are not present in simplified models. In our analysis we focus on the effect of time correlations introduced by reproduction times that are not exponentially distributed (as is the case in continuous time Markovian simulations as in Figure 3.2), but have a unimodal distribution with smaller variation coefficient. This is very relevant in most biological applications (see e.g. [36, 37, 159]), and even in spatially isotropic systems the resulting temporal correlations lead to more regular growth and therefore smaller fluctuations of domain boundaries, with an effect on the patterns as seen in Figure 3.3.

To systematically study these temporal correlations, we introduce a generic one-parameter family of reproduction times, explained in detail in Section 3.2. We show that the reproduction time statistics of individuals has a significant impact on the sectoring patterns. We establish that the growth clusters and competition interfaces still show the characteristic scaling within the KPZ universality class, and the effect of the variation coefficient is present only in prefactors. We predict these effects quantitatively and find good agreement with simulation data; these results are presented in Section 3.3. More realistic reproduction time distributions with a higher number of parameters are considered in Section 3.4, where we show that to a good approximation the effects can be summarized in the variation coefficient

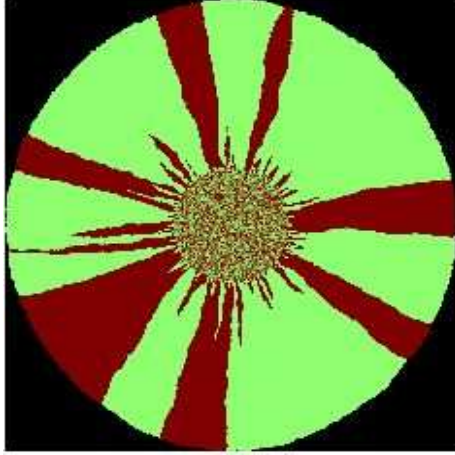


Figure 3.2: Monte Carlo sample of a lattice based Eden model type C, with cells of different colors and comparable initial population size to the colony in Figure 2.5(a). Both colonies share the same characteristic coarsening patterns. This is quite remarkable, since we have ignored all microscopic details of the reproduction mode of *E. coli* which is clearly not spatially homogeneous or Markovian (see [71] and references therein). This is a strong indication that the observed segregation is an emergent phenomenon which is to a large extent independent of microscopic details of reproduction.

and mapped quantitatively onto our generic one-parameter family of reproduction times. Therefore, our results are expected to hold quite generally for unimodal reproduction time distributions, and the variation coefficient alone determines the leading order statistics of the competition patterns.

3.2 δ -Family of Eden models

For regular reproduction times with small variation coefficient the use of a regular lattice would lead to strong lattice effects that affect the shape of the growing cluster [210]. To avoid this, we use the more realistic Eden growth model in a continuous domain in \mathbb{R}^2 with individuals modelled as circular hard-core particles with diameter 1, since we want to study purely the effect of time correlations and segregation patterns. This leads to generalized Eden clusters with stochastic growth dynamics as discussed in Chapter 2.

Let $\Psi(t)$ denote the general index set of particles p at time t , $(x_p, y_p) \in \mathbb{R}^2$ is the position of the centre of particle p , and $s_p \in \{1, 2\}$ is its type. We write $\Psi(t) = \Psi_1(t) \cup \Psi_2(t)$ as the union of the sets of particles of type 1 and 2. We also associate

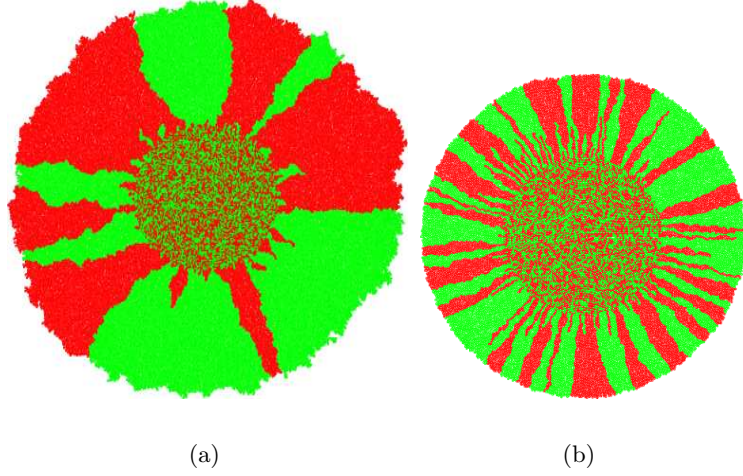


Figure 3.3: A smaller variation coefficient δ in reproduction times (see (3.4) and (3.6)) leads to more regular growth, smoother domain boundaries and finer sectors. Shown are simulated circular populations with (a) $\delta = 1$ and (b) $\delta = 0.1$. Both colonies have an initial radius of $r_0 = 50$, and they are grown up to simulation time $t = 50$ leading to final radii of approximately (a) 120 and (b) 95. The different colors denote cell types 1 and 2.

with each particle the time it tries to reproduce next, $T_p > 0$. Initially, T_p are i.i.d. random variables with cumulative distribution function F_δ with parameter $\delta \in (0, 1]$, which is explained in detail below. After each reproduction T_p is incremented by a new waiting time drawn from the same distribution. Note that we focus entirely on the neutral case, i.e. the reproduction time is independent of the type and both types have the same fitness. We describe the dynamics below in a recursive way.

Following a successful reproduction event of particle p at time $t = T_p$, a new particle with index $q = |\Psi(T_p-)| + 1$ is added to the set Ψ_{s_q} with the same cell type $s_q = s_p$, such that

$$\Psi_{s_p}(T_p+) = \Psi_{s_p}(T_p-) \cup \{q\} . \quad (3.1)$$

Here $\Psi(T_p-)$ and $\Psi(T_p+)$ denote the index set just before and just after the reproduction event, and $|\Psi(t)|$ denotes the size of the set $\Psi(t)$. The position of the new particle is given by

$$(x_q, y_q) = (x_p, y_p) + (\cos \phi, \sin \phi) , \quad (3.2)$$

where $\phi \in [0, 2\pi)$ is drawn uniformly at random. This is subject to a hard-core exclusion condition for circular particles, i.e. the Euclidean distance to all other

particle centres has to be at least 1, as well as to other constraints depending on the simulated geometry as explained below. Note that in our model the daughter cell touches its mother, which is often realistic but in fact not essential, and the distance could also vary stochastically over a small range. The new reproduction times of the mother and daughter are set as

$$T_p \mapsto T_p^{\text{old}} + T, \quad T_q = T_p^{\text{old}} + T', \quad (3.3)$$

where T, T' are i.i.d. reproduction time intervals with distribution F_δ . There can be variations on this where the mother and daughter have different reproduction times, which are discussed in Section 3.4. The next reproduction event will then be attempted at $t = \min \{T_q : q \in \Psi(T_p+)\}$. Reproduction attempts can be unsuccessful, if there is no available space for the offspring due to blockage by other particles. In this case the attempt is abandoned and T_p is set to ∞ , as due to the immotile nature of the cells this particle will never be able to reproduce.

The initial conditions for spatial coordinates and types depend on the situation that is modelled. In this chapter we mostly focus on an upward growth from a flat state in a strip of length L with periodic boundary conditions on the sides, where we take $\Psi(0) = \{1, \dots, L\}$ with $(x_p, y_p) = (p, 0)$, for all $p \in \Psi(0)$. The initial distribution of types can be either regular or random depending on whether we study single or interacting boundaries, and will be specified later. The strip geometry is used to analyze the scaling properties of the surface and thus to infer a quantitative description of the behaviour. However, this growth model can also be seen in experiments, see Figure 3.1.

In Section 3.3 for the main results of this chapter we use reproduction times T distributed as

$$1 - \delta + \text{Exp}(1/\delta), \quad \delta \in (0, 1], \quad (3.4)$$

i.e. T has an exponential distribution with a time lag $1 - \delta \in [0, 1)$ and a mean fixed to $\langle T \rangle = 1$ for all δ . The corresponding cumulative distribution function F_δ is given by

$$F_\delta(t) = \begin{cases} 0 & , t \leq 1 - \delta \\ 1 - e^{-(t-1+\delta)/\delta} & , t \geq 1 - \delta \end{cases}. \quad (3.5)$$

A plot of the probability density function of T can be seen in Figure 3.12(a) for two different values of δ . The variation coefficient of this distribution is given by the standard deviation divided by the mean, which turns out to be just

$$\frac{\sqrt{\langle T^2 \rangle - \langle T \rangle^2}}{\langle T \rangle} = \frac{\delta}{1} = \delta. \quad (3.6)$$

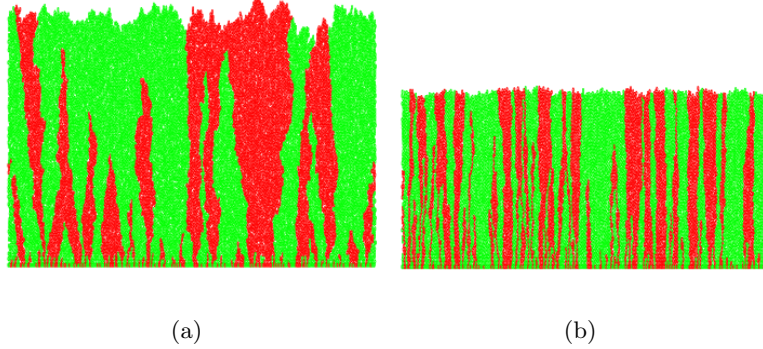


Figure 3.4: Populations in a linear geometry with periodic boundary conditions in lateral direction with (a) $\delta = 1$ and (b) $\delta = 0.1$. Both populations have lateral width $L = 300$, and the colonies are grown to a simulation time $t \approx 50$, leading to heights of approximately (a) 70 and (b) 40. The different colors denote cell types 1 and 2.

With this family we can therefore study reproduction which is more regular than exponential with a fixed average growth rate of unity (equivalent of setting the unit of time).

For $\delta = 1$ this is a standard Eden cluster, but $\delta < 1$ introduces time correlations. While the correlations affect the fluctuations, we present convincing evidence that they decay fast enough not to change the scaling exponents, so the system remains in the KPZ universality class. Furthermore we make quantitative predictions on the δ -dependence of non-universal parameters and compare them to simulations. The more synchronized growth leads to effects similar to the ones seen in experiments (Figure 2.5). To give a visual impression of the patterns produced by the model, in Figure 3.3 we show two growth patterns with $\delta = 1$ and 0.1. The initial condition is a circle, and the types are distributed uniformly at random. The patterns are qualitatively similar to the experimental ones in Figure 2.5 and Figure 3.1, and more regular growth leads to a finer sector structure. The same effect is shown in Figure 3.4 for the simulations in a linear geometry with periodic boundary conditions, which is analyzed quantitatively in the next Section. Smaller values of δ also lead to more compact growth and smaller height values reached in the same time, since the surface is effectively smaller due to a lower roughness.

3.3 Main Results

3.3.1 Quantitative analysis of the colony surface

In this Section we provide a detailed quantitative analysis of the δ family of models in the linear geometry with periodic boundary conditions (see Figure 3.4), starting with the dynamical scaling properties of the growth interface.

We regularize the surface to be able to define it as a function of the lateral coordinate x and time t as

$$y(x, t) := \max \{ y_p : p \in B(t), |x_p - x| \leq 1 \} . \quad (3.7)$$

In case of overhangs (which are very rare) we take the largest possible height, and due to the discrete nature of our model this leads to a piecewise constant function.

As discussed in Chapter 2 the surface of a standard Eden growth cluster is known to be in the KPZ universality class [47, 95], and a suitable scaling limit of $y(x, t)$ with vanishing particle diameter fulfills the KPZ equation (2.1)

$$\partial_t y(x, t) = v_0 + \nu \Delta y(x, t) + \frac{\lambda}{2} (\nabla y(x, t))^2 + \sqrt{D} \eta(x, t).$$

Here v_0 , of the order of unity, corresponds to the growth rate of the initial flat surface (related to the mean reproduction rate and some geometrical effects [17, 95]). For lateral growth models $v_0 \approx \lambda$ and we derive the value for this in Chapter 4. Here the surface tension term with $\nu > 0$ represents surface relaxation. For microbial colony formation we have $\lambda > 0$ and the non-linear term corresponds to an addition of material from cell duplication [84]. As before the fluctuations are described by space-time white noise $\eta(x, t)$, which is mainly related to the stochastic elements of cell division [205].

Note that the average surface height (2.13)

$$h(t) := \left\langle \frac{1}{L} \int_0^L y(x, t) dx \right\rangle,$$

is a monotone increasing function in t . It is also asymptotically linear and therefore we will later also use h as a proxy for time. The average growth velocity of height is δ -dependent, where as seen in Figure 3.4 the $\delta = 1$ colony grows faster than the $\delta = 0.1$ colony. This dependence does not lead to leading order contributions to the statistical properties of the surface or the structure of sectoring patterns.

Figure 3.5 shows a data collapse for the roughness (2.14)

$$S(t) = L^\alpha f(t/L^z) ,$$

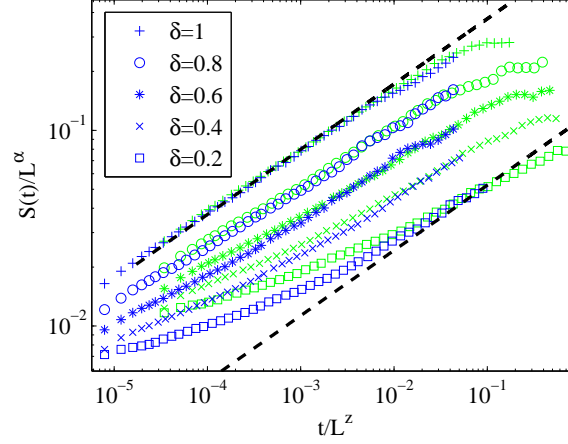


Figure 3.5: Family-Vicsek scaling (2.14) of the surface roughness $S(t)$. The data collapse under rescaling with $\alpha = 1/2$ and $z = 3/2$ occurs in a scaling window which is narrower for small δ due to intrinsic correlations. The different symbols correspond to different values of δ , and the color represents system size, $L = 1500$ (green) and $L = 4000$ (blue). The dashed lines indicate the expected slope $\beta = 1/3$. The data for $L = 1500$ has been averaged over 100 independent realizations and for $L = 4000$ over 30 independent realizations. The error bars are comparable to the size of the symbols.

for two system sizes, and for a number of different values of δ . As δ gets smaller, the surface becomes less rough due to a more synchronized growth. The dashed lines indicate the power law growth with exponent $\beta = 1/3$ in the scaling window. This window ends around $t/L^z \approx 1$ due to finite size effects, where the lateral correlation length reaches the system size and the surface fluctuations saturate. For small t the system exhibits a transient behaviour before entering the KPZ scaling regime due to local correlations resulting from the non-zero particle size and initial conditions. As we quantify later, these correlations are much higher for more synchronized growth at small δ , which leads to a significant increase in the transient regime. The transient time scale is independent of system size and vanishes in the scaling limit, so that the length of the KPZ scaling window increases with L . This transient time scale is directly related to time correlations that are introduced by more synchronized growth, and can be quantified by measuring the vertical correlation length τ . As we show later (3.14), the value of τ can be estimated to be higher for smaller δ values, and therefore increases the crossover time window in which the system exhibits the KPZ scaling behaviour. This behaviour can be observed in Figure 3.5 where for the

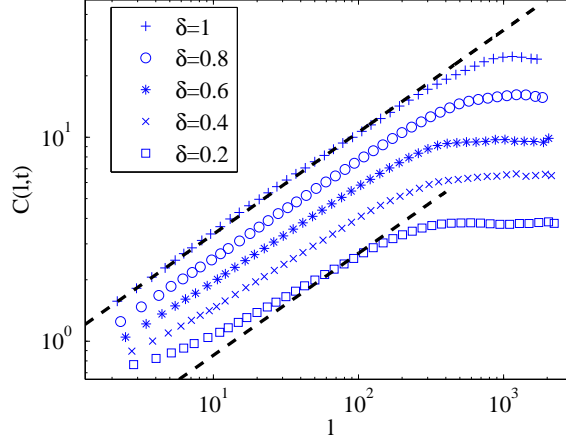


Figure 3.6: The height-height correlation function $C(l, t)$ for $L = 4000$ at $t = 11000$ for various values of δ . The data has been averaged over 30 independent realizations, and the error bars are comparable to the size of the symbols. The dashed lines indicate the expected slope $1/2$.

smallest value $\delta = 0.2$ the scaling regime is still hard to identify for the accessible system sizes.

Another characteristic quantity is the height-height correlation function defined as [8, 17, 117]

$$C(l, t) = \left\langle \frac{1}{L} \int_0^L (y(x, t) - y(x + l, t))^2 dx \right\rangle^{1/2}. \quad (3.8)$$

For a KPZ surface in $1 + 1$ dimensions, $C(l, t)$ obeys the scaling behaviour

$$C(l, t) \sim \begin{cases} (\frac{D}{2\nu} l)^{1/2} & l \ll \xi_{\parallel}(t) \\ (\frac{D}{2\nu})^{2/3} (\lambda t)^{1/3} & l \gg \xi_{\parallel}(t) \end{cases}, \quad (3.9)$$

and $\xi_{\parallel}(t)$ takes the form [6, 8, 17, 174]

$$\xi_{\parallel}(t) \sim (D/2\nu)^{1/3} (\lambda t)^{2/3}. \quad (3.10)$$

A detailed computation can be found in Chapter 4. For small values $C(l, t)$ grows as a power-law with l , and when l exceeds the lateral correlation length it reaches a value that depends on the time t and the parameters of (2.1). This is shown in Figure 3.6, where $C(l, t)$ is plotted for various values of δ , and the data agree well with the exponent $\alpha = 1/2$ for the KPZ class indicated by dashed lines.

The time correlations introduced by the partial synchronization can be estimated by considering a chain of N growth events where each particle is the direct descendant of the previous one. Each added particle corresponds to a height change Δy_i , and has an associated waiting time T_i with distribution (3.4). During time t there are $N(t)$ growth events, and since the average reproduction time is 1 with variance δ^2 , we have $\langle N(t) \rangle \approx t$ and $\text{var}(N(t)) \approx \delta^2 t$. The height of the last particle is $y_{N(t)} = \sum_i^{N(t)} \Delta y_i$, leading to

$$\text{var}(y_{N(t)}) = \langle \Delta y_i \rangle^2 \text{var}(N(t)) + \langle N(t) \rangle \text{var}(\Delta y_i) . \quad (3.11)$$

The terms in this expression correspond to two sources of uncertainty: (i) due to the randomness in T_i the number of growth events vary with $\text{var}(N(t))$, and (ii) the individual height increments are random with $\text{var}(\Delta y_i)$. This leads to

$$\text{var}(y_{N(t)}) \approx t \langle \Delta y_i \rangle^2 (\delta^2 + \epsilon^2) , \quad (3.12)$$

where $\epsilon = \sqrt{\text{var}(\Delta y_i)} / \langle \Delta y_i \rangle$ denotes the variation coefficient of the height fluctuations due to geometric effects.

The squared variation coefficient ϵ^2 arises due to geometric disorder and has been consistently fitted to values around 0.4. This value is compatible with the following very simple argument. Consider a single growth event around an isolated spherical particle with diameter 1, with direction θ chosen uniformly in a cone with opening angle $\pi/2$ around the vertical axis. This leads to $\langle \Delta y_i \rangle = \int_{-\pi/2}^{\pi/2} \cos \theta \frac{d\theta}{\pi} \approx 0.64$ and

$$\epsilon^2 \approx \left(\int_{-\pi/2}^{\pi/2} \cos^2 \theta \frac{d\theta}{\pi} - \langle \Delta y_i \rangle^2 \right) / \langle \Delta y_i \rangle^2 \approx 0.23 , \quad (3.13)$$

which is of the same order as the fitted values. Choosing only a slightly larger opening angle 0.55π of the cone leads to $\epsilon^2 \approx 0.39$ and $\langle \Delta y_i \rangle \approx 0.57$. These are in good agreement with the fitted values and with measurements of $\langle \Delta y_i \rangle$ (not shown). The latter show some dependence on δ , related also to the compactness of growth as seen in Figure 3.3 and Figure 3.4, but this does not contribute to our results on a significant level so we ignore this dependence. Actual growth events in the simulation are of course often obstructed by neighbouring particles, but the right order of magnitude of the parameters can be explained by the basic argument above.

We define the correlation time τ as the amount of time by which the uncertainty of the height of the chain becomes comparable to one particle diameter, $\text{var}(y_{N(\tau)}) = O(1)$. Since $\langle \Delta y_i \rangle$ is largely independent of δ , the time correlation induces a fixed intrinsic vertical correlation length

$$\tau \sim \frac{1}{\delta^2 + \epsilon^2} \quad (3.14)$$

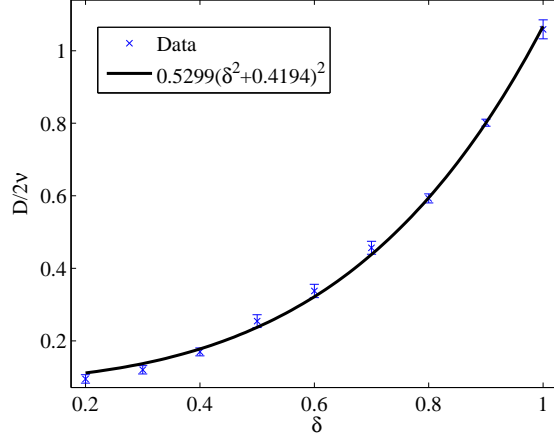


Figure 3.7: Dependence of the KPZ parameters $D/(2\nu)$ on δ . Data are obtained from (3.9) by fitting the prefactor of the power law in Figure 3.6, using that the proportionality constant is very close to 1 (cf. derivation (4.22) in the Chapter 4). The data are in good agreement with the prediction (3.16) with fitted parameters $\epsilon^2 \approx 0.42$ and $D/(2\nu)(\delta = 1) \approx 1.1$.

in the model. This correlation length reduces fluctuations and leads to an increase in the expected saturation time t_s of the system, namely $t_s/\tau \sim L^z$, a modification of the usual relation with the system size L . Analogous to the standard derivation of the time-dependence of the lateral correlation length, this leads to

$$\xi_{\parallel}(t) \sim (t/\tau)^{1/z} . \quad (3.15)$$

Together with (3.10), from the behaviour of the correlation length we expect

$$D/(2\nu) \sim (\delta^2 + \epsilon^2)^2 , \quad (3.16)$$

since λ is largely independent of δ (see Chapter 4, Section 4.3.3). This is shown to be in very good agreement with the data in Figure 3.7, for fitted values of ϵ and a prefactor. The fit value for ϵ is compatible with simple theoretical arguments (see above). So the very basic argument to derive an intrinsic vertical correlation length explains the δ -dependence of the surface properties very well. Measuring height in this intrinsic length scale, we observe a standard KPZ behaviour with critical exponents being unchanged, since the intrinsic correlations are short range (i.e. decay exponentially on the scale τ). This is in contrast to effects of long-range correlations where the exponents typically change, see e.g. studies with long-range

temporally correlated noise [9, 97, 143] or memory and delay effects using fractional time derivatives and integral/delay equations [33, 60, 85].

3.3.2 Domain boundaries

In this section we derive the superdiffusive behaviour of the domain boundaries between the species from the scaling properties of the interface. Since the boundaries grow locally perpendicular to the rough surface, they are expected to be superdiffusive, which has been shown in [45, 177, 178, 203] and has also been observed through dynamic scaling [69] of experimental data. The reason for the deviation of the boundary from a simple Brownian motion scaling is because the underlying dynamics of the domain boundaries depend on the surface enclosing the region [5, 22, 174]. The boundaries propagate locally normal to the surface, where the surface itself is a stochastic field which satisfies the Langevin equation (2.1), which leads to an increase in roughness of the dynamical behaviour in the trajectory. In order to confirm this quantitatively for our model, we perform simulations with initial conditions $\Psi_1(0) = \{0, \dots, [L/2] - 1\}$ and $\Psi_2(0) = \{[L/2], \dots, L - 1\}$, i.e. the initial types are all red on the right half and all green on the left half of the linear system as illustrated in Figure 3.9(a). Therefore we have two sector boundaries X^1 and X^2 with initial positions $X_0^1 = [L/2] - 1/2$ and $X_0^2 = L - 1/2$. After growing the whole cluster, we define the boundary X_h as a function of the height via the left most particle in a horizontal strip of width 1 and medium height h :

$$\begin{aligned} X_h^1 &= \max \{x_p + 1/2 : |y_p - h| < 1/2, p \in \Psi_1\} \\ X_h^2 &= \max \{x_p + 1/2 : |y_p - h| < 1/2, p \in \Psi_2\} , \end{aligned} \quad (3.17)$$

where we take the periodic boundary conditions into account. The simulations are performed on a system of size $L = 1000$, and run until a time of $t = 2000$, this is well before the expected time of complete annihilation, which is of order $L^{3/2}$ proportional to the saturation timescale in the KPZ class. Therefore we can treat the sector boundaries as two independent realizations of the boundary process which we just denote as $(X_h : h \geq 0)$.

It has been already noted in [177] that this process is expected to follow the same scaling as the lateral correlation length. For the mean square displacement

$$M(h) := \langle (X_h - X_0)^2 \rangle \quad (3.18)$$

we therefore get with (3.10) and (3.16),

$$M(h) \approx \sigma_\delta^2 h^{2H} \sim \xi_\parallel^2(h). \quad (3.19)$$

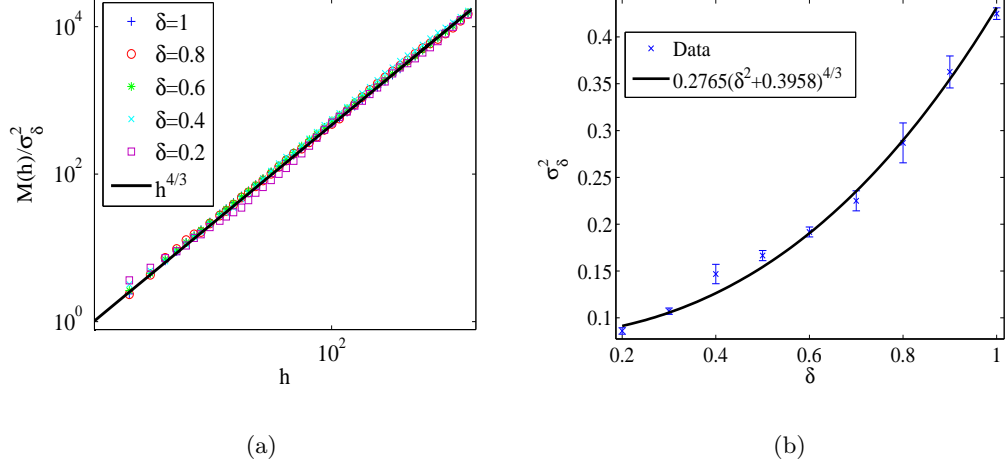


Figure 3.8: Scaling behaviour of the mean square displacement $M(h)$ (3.19). The system size is $L = 1000$, the data is averaged over 500 independent realizations and the error bars are comparable to the size of the symbols. (a) Data collapse of the normalized quantity $M(h)/\sigma_\delta^2$ as a function of height h for several values of δ . The values in the normalization σ_δ^2 are taken from the best fit shown as full line in (b). Each curve follows a power law with exponent $4/3$, the line corresponding to $h^{4/3}$ is shown as comparison. (b) The prefactor σ_δ^2 , where the data are best fits according to (3.19). The solid line used for the collapse in (a) follows the prediction $(\delta^2 + \epsilon^2)^{4/3}$ with fitted $\epsilon^2 \approx 0.40$, which is compatible with the fit in Figure 3.7.

Here $\sigma_\delta^2 \propto (\delta^2 + \epsilon^2)^{4/3}$ and the Hurst exponent is $H = 2/3$, which quantifies the superdiffusive scaling of the mean square displacement (3.18). This prediction is in very good agreement with data for the scaling of $M(h)$ and its prefactor as presented in Figure 3.8, and the fit value for ϵ^2 is consistent with the one in Figure 3.7. As before, for $D/(2\nu)$ the δ -dependence is absorbed by the prefactor, and the power law exponent $4/3$ for $M(h)$ remains unchanged from standard KPZ behaviour. In Chapter 4 we present a more detailed derivation of the prefactor σ_δ^2 and the Hurst exponent using the flow equations of the KPZ universality class and a mode coupling calculation. We can easily relate the domain boundaries exponent H to the dynamics of the surface by considering a simple scaling argument. As with the derivation of Eq. (2.1) in [95], the boundary evolves locally normal to the surface $y(x, t)$ and can be seen to satisfy the following dynamical equation

$$\frac{dX_h}{dh} = -\frac{\partial y(X_h, h)}{\partial x}, \quad (3.20)$$

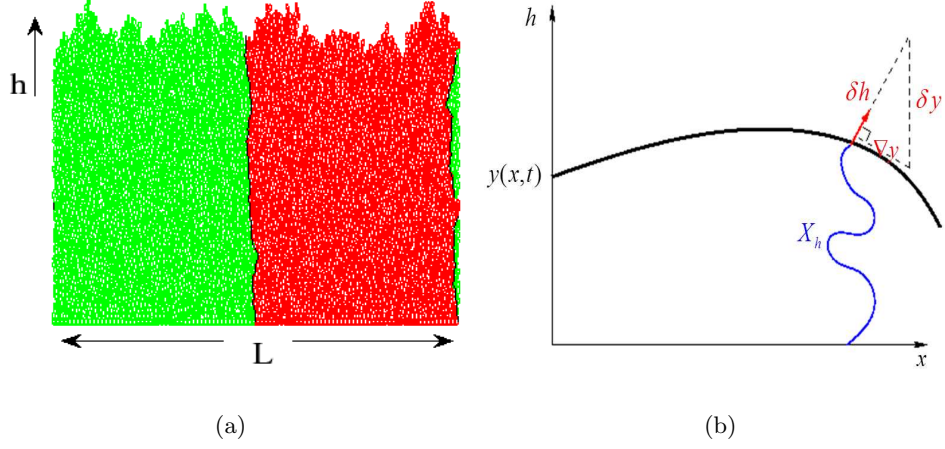


Figure 3.9: (a) Illustrating an example of the population used to study the boundary. Initial conditions are $\Psi_1(0) = \{0, \dots, [L/2] - 1\}$ and $\Psi_2(0) = \{[L/2], \dots, L - 1\}$ and subsequently the lateral movement of the boundary is measured as a function of height h . (b) Schematic analysis used to derive the equation of motion of the boundary path (3.20). The dynamical equation follows from the physical argument of lateral growth as in [95].

a schematic illustration is given in Figure 3.9(b). The exponent H is known to relate to the space-time scaling of the boundary X . It is expected that X has a self-similar property, namely that $(X_{bh}, h \geq 0)$ is distributed as $(b^H X_h, t \geq 0)$ holds for all $b > 0$. In order to find H we use (3.20) and adapt the self-affine transformation (2.2) such that we have,

$$\begin{aligned}
 h &\rightarrow h' = bh \\
 x &\rightarrow x' = b^{1/z}x \\
 y &\rightarrow y' = b^{\alpha/z}y.
 \end{aligned} \tag{3.21}$$

This leads to the following

$$\frac{dX_{bh}}{dh} = -b^{\alpha/z-1/z+1} \frac{\partial y}{\partial x},$$

using the exponent values, $\alpha = 1/2$ and $z = 3/2$, we have

$$\frac{dX_{bh}}{dh} = -b^{2/3} \frac{\partial y}{\partial x},$$

and since $X_{bh} \sim b^H X_h$ this gives $H = 2/3$.

We can further investigate the law of the process $(X_h, h \geq 0)$. The data presented in Figure 3.10(a) clearly support that X_h is a Gaussian process. A fractional Brownian motion (fBm) with stationary increments seems to be a natural model for the X_h in the KPZ scaling window. This is confirmed by the behaviour of the correlation function $\langle X_{h+\Delta h} X_h \rangle$, which is shown in Figure 3.10(b) for various δ and two values of the lag $\Delta h > 0$. For a fBm with mean square displacement (3.19) we expect

$$\langle X_{h+\Delta h} X_h \rangle \approx \frac{\sigma_\delta^2}{2} ((h+\Delta h)^{2H} + h^{2H} - |\Delta h|^{2H}) \quad (3.22)$$

for all $\Delta h > 0$ and $h > 0$ sufficiently large to have no effects from the flat initial condition. For simplicity we have assumed here that $X_0 = 0$.

This is in good agreement with the data, and we conclude that the sector boundaries can be modelled by fBm with superdiffusive Hurst exponent $H = 2/3$ and a δ -dependent prefactor σ_δ (3.19). We note that the exponent $H = 2/3$ has also been observed in experiments [69]. Further properties of fBm will be discussed in Section 5.3 and Section 6.2.

3.3.3 Sector patterns

It is well understood that under the assumption of diffusive scaling, how a single boundary dynamics leads to a prediction for sector statistics for well-mixed initial conditions [5, 71]. In Chapter 6 we provide an extended explanation of this. In this section we shortly review this approach and show that it carries over straight away to systems with $\delta < 1$ and fBm paths. The sector boundaries X_h^i interact by diffusion limited annihilation which drives a coarsening process, as can be seen in Figure 3.4 for two linear populations with different values of δ . Both systems have the same initial condition with a flat line of particles of independently chosen types, and the finer coarsening patterns for smaller values of δ result from the reduced boundary fluctuations due to the prefactor σ_δ (3.19).

Let $N(h)$ be the number of sector boundaries at height $h \geq 0$ as defined in (3.17). For systems of diffusion limited annihilation [4, 180] it is known that $N(h)$ is inversely proportional to the root mean square displacement, and decays according to

$$\langle N(h) \rangle \approx \frac{1}{\sqrt{4\pi M(h)}} \sim \frac{1}{\sigma_\delta} h^{-2/3} . \quad (3.23)$$

This prediction is confirmed in Figure 3.11, where we plot $\langle N(h) \rangle$ for various δ , and obtain a data collapse by multiplying the data with $\sqrt{4\pi\sigma_\delta^2/L}$, [4]. We include the system size L in the rescaling so that rescaled quantities are of order 1, and all data collapse on the function $h^{-2/3}$ without the prefactor.

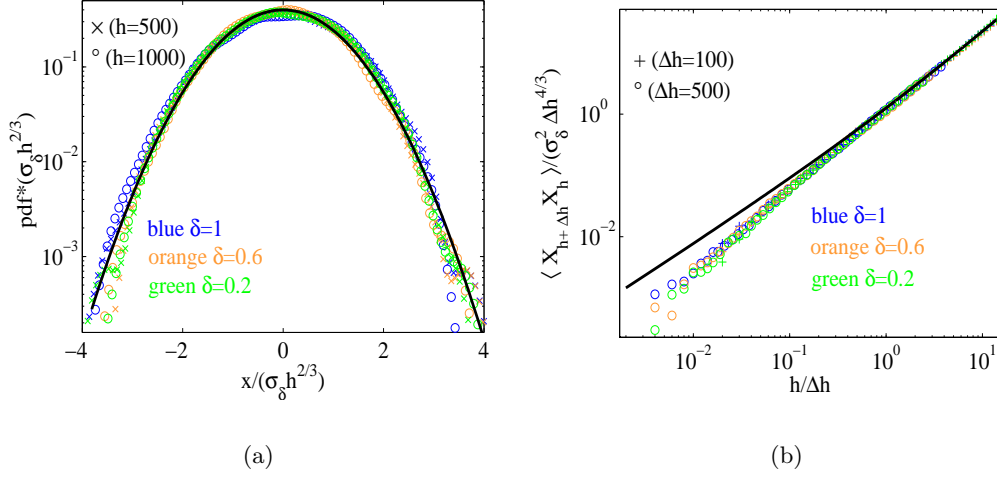


Figure 3.10: The sector boundary X_h behaves like a fractional Brownian motion. (a) The standardized probability density function (pdf) of X_h as a function of the rescaled argument $x/(\sigma_\delta h^{2/3})$ for different heights h and values of δ . The black solid parabola is the pdf of a standard Gaussian on a logarithmic scale. (b) The covariance function $\langle X_{h+\Delta h} X_h \rangle$ shows the behaviour (3.22), which is plotted as the solid black curve. After rescaling we get a data collapse as a function of $h/\Delta h$, which agrees well with the prediction if h is sufficiently large and the flat boundary conditions become irrelevant. Data are averages over 1000 realizations and the error bars are comparable to the size of the symbols.

Using (3.23), we can predict the expected number of sector boundaries at the final height in the simulations shown in Figure 3.4. For $\delta = 1$, the final height is $h \approx 70$ leading to $\langle N(h) \rangle \approx 7.6$, and for $\delta = 0.1$, $h \approx 40$ with $\langle N(h) \rangle \approx 32$. These numbers are compatible with the simulation samples shown which have 6 and 34 sector boundaries remaining, respectively.

In general, diffusion limited annihilation is very well understood, and there are exact formulas also for higher order correlation functions [4, 46, 135, 148, 180], which can be derived from the behaviour of a single boundary (3.19). This demonstrates that the behaviour of populations is fundamentally the same for all values of δ and characterized by the KPZ universality class, and the observed difference in coarsening patterns and segregation can be explained by the functional behaviour of the prefactors.

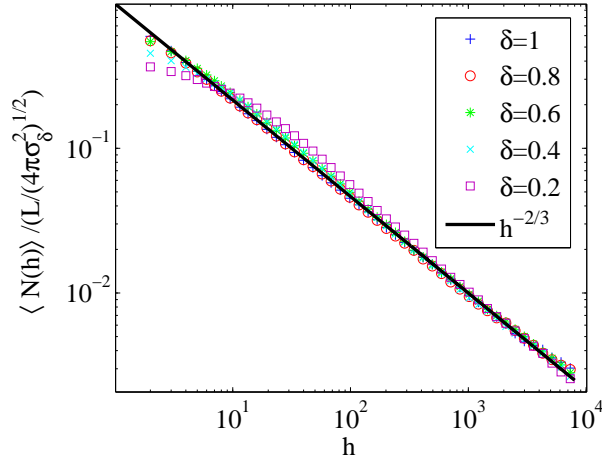


Figure 3.11: The average number of sector boundaries $\langle N(h) \rangle$ follow a power law (3.23) with exponent $-2/3$, which is indicated by the full line. The data are plotted for a system size $L = 1500$ and various values of δ (see legend), and collapse on the function $h^{-2/3}$ when rescaled by $L/\sqrt{4\pi\sigma_\delta^2}$. Data are averages over 500 realizations and the error bars are comparable to the size of the symbols.

3.4 Realistic reproduction times

In this section we study the effect of more realistic reproduction time distributions on the sectoring patterns, and how they can be effectively described by the previous δ -dependent family of distributions in terms of their variation coefficient. As an example, we focus on *S. cerevisiae*, which is one of the species included in [69], and for which reproduction time statistics is available [36, 37, 159] by the use of time lapsed microscopy. *S. cerevisiae* cells have largely isotropic shape so that spatial correlations during growth should be minimal, fitting the assumptions of our model. However, the results of this section cannot be applied directly to quantitatively predict the patterns in Figure 2.5, since the variation coefficients under the experimental conditions in [69] are not known to us.

When yeast cells divide, the mother cell forms a bud on its surface which separates from the mother after growth to become a daughter cell. The mother can then immediately restart this reproduction process, whereas the daughter cell has to grow to a certain size in order to be classed as a mother and be able to reproduce. We denote this time to maturity by T_m and the reproduction time of (mother) cells by T_r .

The results in [36, 37, 159, 164] suggest that Gamma distributions are a

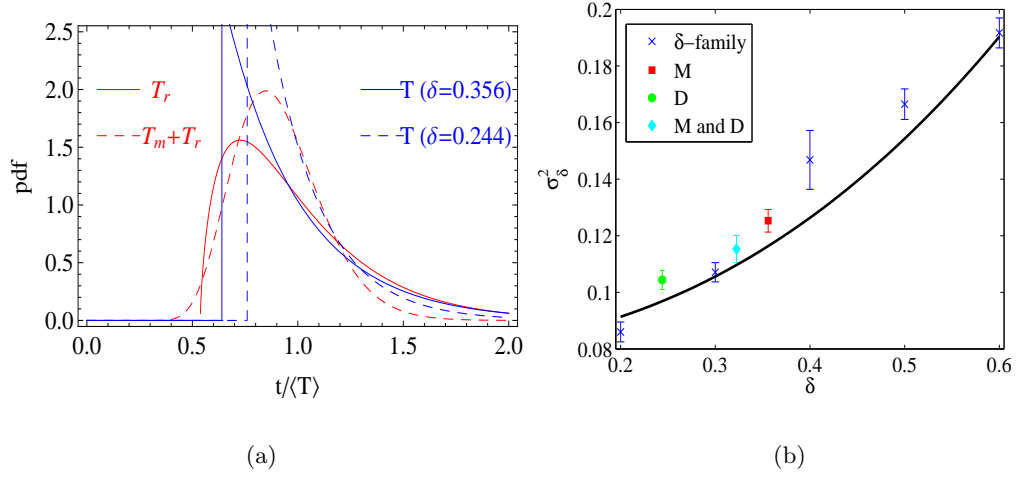


Figure 3.12: Comparison of realistic reproduction times with the δ model. (a) The probability density functions of reproduction times of mother cells T_r (full red line) and daughter cells $T_m + T_r$ (dashed red line) with normalized mean compared to T from (3.4) with corresponding δ (blue). (b) The prefactor of the mean square displacement σ_δ^2 as introduced in (3.19) and Figure 3.8. The data correspond to reproduction times T_r for all cells (denoted M), $T_m + T_r$ for all cells (denoted D) and the most realistic mixed model (denoted M and D) as explained in the text. All these cases are consistent with previous results from Figure 3.8.

reasonable fit for the statistics for T_m and T_r , where

$$T_r \text{ is distributed as } \rho_0 + \text{Gamma}(\rho_1, \rho_2), \quad (3.24)$$

with delay $\rho_0 > 0$. The parameters ρ_1, ρ_2 denote the shape and scale of the Gamma distribution, which has a probability density function

$$f_{\rho_1, \rho_2}(t) = t^{\rho_1-1} \frac{\exp(-t/\rho_2)}{\Gamma(\rho_1)\rho_2^{\rho_1}}, \quad t \geq 0.$$

The time to maturity is

$$T_m \text{ distributed as } \text{Gamma}(\rho_3, \rho_4), \quad (3.25)$$

and in [159] data are presented for which the parameters can be fitted to $\rho_0 \approx 1.0$, $\rho_1 \approx 1.7$, $\rho_2 \approx 0.51$, $\rho_3 \approx 9$ and $\rho_4 \approx 0.3$. The unit of ρ_0 , ρ_2 and ρ_4 are hours and ρ_1, ρ_3 are dimensionless numbers.

The random variables T_m and T_r may be assumed to be independent and the time

until a newly born daughter cell can reproduce is distributed as the sum $T_m + T_r$. Note that the expected value of reproduction times $\langle T_r \rangle = \rho_0 + \rho_1 \rho_2 = 1.86$ is smaller than that for times to maturity $\langle T_m \rangle = \rho_3 \rho_4 = 2.52$ but of the same order. The real time scale for these numbers is hours, but we are only interested in the shape of the distributions rescaled to mean 1 like our previous model.

The distribution (3.4) of δ -dependent reproduction times can be written as $T = 1 - \delta + \text{Gamma}(1, \delta)$, since exponentials are a particular case of Gamma random variables with shape parameter 1. The reproduction time T_r of mother and $T_m + T_r$ of daughter cells are also unimodal with a delay, and very similar in shape to T in our model. This can be seen in Figure 3.12(a), where we plot the probability densities renormalized to mean 1. Analogous to (3.6), we can compute the variation coefficients of T_r and $(T_m + T_r)$, which turn out to be 0.356 and 0.244, respectively. To confirm that the behaviour of sector boundaries can be well predicted by the variation coefficient, we present data of three simulations in Figure 3.12(b): one with reproduction times T_r for mother and $T_m + T_r$ for daughter cells as explained above, one with T_r for all cells, and one with $T_m + T_r$ for all cells. The mean square displacement $M(h)$ for these models also shows a power law with exponent $4/3$ analogous to Figure 3.8, and the prefactors σ_δ match well with our simplified model.

To estimate the variation coefficient in the model with mother and daughter cells, we measure the fraction of reproduction events of daughter cells to be $p_d = 0.88$, and $p_m = 0.12$ for mother cells. The reproduction time of the union of mother and daughter cells is then taken as

$$T \text{ distributed as } \Theta(T_m + T_r) + (1 - \Theta)T_r, \quad (3.26)$$

where the independent Bernoulli variable $\Theta = \text{Be}(p_d) \in \{0, 1\}$ indicates reproduction of a daughter. The variation coefficient of T turns out to be 0.322. In all three combinations of realistic reproduction times we find that the generic family of F_δ introduced in (3.4) provides a good approximation for the properties of domain boundaries in simulations. We expect this method of mapping realistic reproduction time distributions to our δ -dependent family to hold for a large class of microbial species which have similar unimodal distributions.

3.5 Conclusion

In this chapter we have introduced a generalization of the Eden growth model with competing species and with an adapted reproduction time statistics of the individuals. The latter is highly relevant in biological growth phenomena, and can have

significant influence on the sectoring patterns observed e.g. in microbial colonies. Although growth of immotile microbial species is the prime example, our results also apply to more general phenomena of space limited growth with inheritance, where the entities have a complex internal structure that leads to non-exponential reproduction times, such as colonization/range expansions or epidemic spreading of different virus strands. Our main result is that, as long as the reproduction time statistics have finite variation coefficients, the induced correlations are local and the macroscopic behaviour of the system is well described by the KPZ universality class. The dependence of the relevant parameters in the macroscopic description on the variation coefficient (a microscopic property of the system) is well understood by simple heuristic arguments, which we support with detailed numerical evidence.

Figures 3.3 and Figures 3.4 illustrate that changes in the variation coefficient δ of reproduction times lead to significant changes in the competition growth patterns in our model, and we are able to quantitatively predict this dependence. Our results show that these patterns are an emergent phenomenon, which can be characterized by the fluctuating paths of domain boundaries, with the only relevant parameter σ_δ . Therefore these systems can be described by an interacting particle system framework which we introduce in Chapter 5.

Our results on the effects of reproduction time statistics are quite relevant in real microbial colonies. Where our study indicates that the variation coefficient of reproduction times can have a strong influence on observed competition patterns. This coefficient has been measured for various species in the literature, where it is found that it depends on experimental conditions such as type of strain, concentration of nutrients, temperature etc. [50, 168, 189]. For example, it was found that for *S. cerevisiae* the coefficient for mother cells can vary between $\delta \approx 0.12 - 0.38$ and for daughter cells $\delta \approx 0.19 - 0.28$ depending on concentrations of guanidine hydrochloride. It has also been observed that δ can be as small as 0.047 for these yeast type organisms [187]. For *E. coli* values of $\delta \approx 0.32 - 0.51$ have been observed in [50, 154, 206], which is larger, and compatible with the observations in Figure 2.5. But for the experimental conditions in [69] with pattern growth the coefficient has not been determined and therefore the results in this paper cannot be readily applied to explain the differences in competition patterns between *S. cerevisiae* and *E. coli*. In particular, the latter have anisotropic rod shape which has probably a strong influence in the resulting colony. Another rod shaped bacterium, *Pseudomonas aeruginosa*, has variation coefficient $\delta \approx 0.14 - 0.2$ [154, 164]. This bacterium along with *E. coli* belongs to the gram-negative bacteria family. Despite obvious similarities between *P. aeruginosa* and *E. coli* in the shape of their cells,

their colonies display morphological differences [112], which fit qualitatively into our results.

In general, it is an interesting question if the simple mechanism of time correlations due to reproduction time statistics with variable variation coefficients is sufficient to quantitatively explain sectoring patterns in real experiments. It would be interesting to see how the results from our model compare to the influence on growth patterns and colony shape coming from factors such non-isotropic cell shape or correlations between mother and daughter cells. For example, an effective attraction between cells which is often observed in the growth of microbial colonies would influence the growth directions, and further smoothen the surface and the fluctuations of sector boundaries. For future research, it should also be possible to describe spatial effects due to non-isotropic particle shapes with the methods introduced in this chapter.

Chapter 4

Scaling functions and amplitude universality for the KPZ equation

4.1 Introduction

The universal scaling exponents of the KPZ universality class can be found through a combination of Galilean invariance and stationary distribution results (as seen in Chapter 2). However, there exists a more exact approach which reveals intrinsic details about the properties of the continuum equation and leads to characterizing the scaling functions for growth models. Through an extension of Wilson's equilibrium theory a dynamical renormalization group method has been developed to uncover dynamic properties of spin systems [81, 213]. Such a method can be extended and applied to stochastic equations similar to KPZ, where theoretical predictions can be obtained for many surface quantities [8, 59, 95, 143]. In particular, this method reveals flow equations which depend on the dimensions of space d and govern the behaviour of the parameters (ν, λ, D) in (2.1). From these equations one can obtain the exact values of the scaling exponents which is expected for the KPZ universality class (2.3). The analysis of the exponents given from the renormalization group theory only holds for dimensions $d \leq d_c$, where $d_c = 2$ is the critical dimension. In $d = 1$ spatial dimension, the study of a variety of stochastic growth models have shown results which agree with the renormalization-group predictions [72, 100, 117, 119, 139]. Most studies focus on extracting the asymptotic exponents α , β and z , while less attention is given to the connections between microscopic growth dynamics and the corresponding continuum equation. For dimensions $d \geq 2$ numerical simulations of

KPZ models suggest that the exponents depend on the values of the parameters in (2.1). For certain values of (ν, λ, D) the large scale behaviour is found to be governed by the Edward Wilkinson universality class [17].

For many complex systems, it is often difficult to directly obtain information on microscopic interactions and variables from the coarse-grained mesoscopic or macroscopic scale spatial structure. Thus, a more detailed study of the scaling behavior of the KPZ equation (2.1) as shown here is helpful in establishing a connection between discrete models and the continuum description. In addition, we also expect that our techniques can be employed in the analysis of other surface growth models and a variety of experiments where the surface properties are not necessarily described by the KPZ class. But in general models, where the concept of universal amplitude ratios and scaling functions depend on the existence of a continuum description.

The analysis we carry out will be applied to 1 + 1 dimensional KPZ equation (2.1) in a state of driven growth, this is when the interface moves with velocity v_0 such that we take $y \rightarrow y + v_0 t$. Using the combination of renormalization group theory with a mode coupling calculation and a scaling approach, which first appeared in [6, 8, 117], we derive expressions for amplitudes and scaling functions shown in the previous chapter. These will be the correlation function (3.8), the lateral correlation length $\xi_{\parallel}(t)$ (3.10), the behavior of the average $|\nabla y|^2$ and the prefactor σ_δ^2 of the mean squared displacement $M(h)$ as defined by (3.18). These are found as a function of the macroscopic parameters (ν, λ, D) in Eq. (2.1), and provide an analytical form for expressions of universal scaling functions. We note that, in contrast to the type of approaches used to estimate scaling exponents, where one would measure fluctuations of a quantity over a large scale and for large system sizes, our analysis provides an analytical expression for various quantities. Our predictions are confirmed by comparing to measurements of various quantities presented in Chapter 3.

4.2 Dynamic Renormalization group theory

The universality class of a growth model can be identified through determining the values of the scaling exponents α , β and z , these govern the behaviour of scaling functions such as the roughness (2.14) and the correlation function (3.8). For a large number of systems in statistical mechanics, the existence and measurements of universal scaling exponents has been a central problem. Through dynamic renormalization group theory one can do a systematic calculation of these scaling exponents

[95, 96].

For a growth phenomenon we are generally interested in the dynamic properties of the roughening process. Due to the stochastic and irreversible nature of the growth process, the equation of motion has no equilibrium counterpart and a suitable frequency space renormalization group method has been established to treat the dynamical properties of equations such as KPZ. The general method can be used to study the dynamical properties within various stochastic systems, where using stochastic equations such as Eq. (2.1) one can obtain theoretical predictions for scaling functions [17].

The dimensional analysis routine (2.2) used in Chapter 2 can be successfully applied to the EW equation (2.4), where it was shown to provide the exact values of the scaling exponents of the self-affine interface. However, it cannot be used to study all systems, and in our case does not work for the KPZ growth equation. Using the scale transformation (2.2), the KPZ equation (2.1) with $v_0 = 0$ becomes

$$\partial_t y = \nu b^{z-2} \Delta y + \frac{\lambda}{2} b^{z+\alpha-2} (\nabla y)^2 + b^{-d/2+z/2-\alpha} \sqrt{D} \eta(x, t).$$

As shown before, simply equating all powers of b to zero does not give the right values for exponents since under the transformation the parameters (ν, λ, D) change. This change in parameters can be expressed as

$$\begin{aligned} \nu &\rightarrow \nu b^{z-2} \\ \lambda &\rightarrow \lambda b^{z+\alpha-2} \\ D &\rightarrow D b^{-d+z-2\alpha}. \end{aligned} \tag{4.1}$$

Under the rescaling and mapping of (2.2) we get (4.1), which is a general evolution of the parameters through a length scale transformation. In general, this evolution can be followed through defining $J(\ell) := (\nu(\ell), \lambda(\ell), D(\ell))$, where we take the continuous length parameter ℓ , which is related to the rescaling parameter b by $b = e^\ell$. The dynamic renormalization group method allows a derivation of an equation which governs the rate of change of J under ℓ . Thus by performing (2.2) successively on (2.1) we obtain an evolution of the parameters J as a function of the old parameters, $J(1) = (\nu(1), \lambda(1), D(1))$ and the dynamical equations describing J are known as the KPZ flow equations [17]. These flow equations describe the rate of change in J

under the renormalization group transformation and in general take the form

$$\begin{aligned}\frac{d\nu}{d\ell} &= \nu R_\nu(\nu, \lambda, D) \\ \frac{d\lambda}{d\ell} &= \lambda R_\lambda(\nu, \lambda, D) \\ \frac{dD}{d\ell} &= D R_D(\nu, \lambda, D).\end{aligned}\tag{4.2}$$

If the non-linear term is absent ($\lambda = 0$) the exponents are subsequently given by the EW class. The properties of the KPZ equation depend on the number of spatial dimensions d . Where as we shall see, a small non-linearity λ vanishes under rescaling for $d > d_c = 2$ and diverges to “infinity” for $d < d_c$, so the non-linearity is an important term for $d < d_c$. Since an exact solution is known for $\lambda = 0$ [8], we can try and perturbatively solve the KPZ equation and once the solution is obtained up to the desired order of λ , we then apply the renormalization group procedure (4.1). This will lead to the flow diagrams describing the variation of the parameters under rescaling. The scaling exponents are those values which correspond to a stable fixed point of the flow equations. Physically the stable fixed point translates into the scale invariant property of the system, where the parameters of the KPZ equation do not change upon further application of the renormalization group transformation. In principle this fixed point is obtained by taking $(d/d\ell)J = 0$ i.e. solving the system $R_J = 0$. In this section we give a brief overview of the steps involved in the derivation of the flow equations of (ν, λ, D) via the dynamic renormalization group technique. This of course has been done before and a more detailed derivation can be found in [17, 59, 65, 95, 96, 143].

In order to treat the KPZ equation by a frequency space renormalization group method, we require Eq. (2.1) to be in a Fourier counterpart form. Then we employ a perturbation method, where in powers of the parameter λ , this leads to a series expansion for the Fourier solution of (2.1). The expansion is performed around the $\lambda = 0$ solution of (2.1), which corresponds to an exact solution $y(x, t)$ for the linear EW equation shown in Eq. (2.4). For convenience we give the form of this solution in Section 4.3. In general, the perturbation method leads to identifying how a small non-linearity λ effects the dynamical behaviour of an interface governed by the EW equation.

Using the Fourier components of the height function, defined by

$$y(x, t) = \int_{-\infty}^{\infty} \frac{dw}{2\pi} \int^{|k| < \psi} \frac{d^d k}{(2\pi)^d} \hat{y}(k, w) e^{-i(k \cdot x + wt)},$$

the momentum integrals are subject to an upper cut off ψ called the Brillouin zone, which in real space x represents the lattice spacing of the order $dx \sim 1/\psi$. The KPZ

equation in Fourier space becomes

$$-iw\hat{y}(k, w) = -\nu k^2\hat{y}(k, w) - \frac{\lambda}{2} \int \int \frac{d^d q d\Omega}{(2\pi)^{d+1}} q \cdot (k-q)\hat{y}(q, \Omega)\hat{y}(k-q, w-\Omega) + \sqrt{D}\hat{\eta}(k, w). \quad (4.3)$$

Since the noise is taken to be uncorrelated in space-time, its Fourier transform will satisfy $\langle \hat{\eta}(k, w) \rangle = 0$ and

$$\langle \hat{\eta}(k, w)\hat{\eta}(k', w') \rangle = (2\pi)^{-d-1} \delta(k+k')\delta(w+w').$$

Re-arranging the terms of (4.3) we write it as

$$\begin{aligned} \hat{y}(k, w) = G_0(k, w) & \left[\sqrt{D}\hat{\eta}(k, w) \right. \\ & \left. - \frac{\lambda}{2} \int \int \frac{d^d q d\Omega}{(2\pi)^{d+1}} q \cdot (k-q)\hat{y}(q, \Omega)\hat{y}(k-q, w-\Omega) \right] \end{aligned} \quad (4.4)$$

where $G_0(k, w)$ is known as the bare propagator [17] taking the form

$$G_0(k, w) = \frac{1}{\nu k^2 - iw}.$$

We can conveniently express (4.4) as

$$y(k, w) = G_0(k, w) \left[\sqrt{D}\hat{\eta}(k, w) + \lambda N[\hat{y}(k, w)] \right], \quad (4.5)$$

where $N[\hat{y}(k, w)]$ is the non-linear integral part. If $\lambda = 0$ we have an exact solution of the Edward Wilkinson equation

$$\hat{y}(k, w) = \sqrt{D}G_0(k, w)\hat{\eta}(k, w), \quad (4.6)$$

for $\lambda \neq 0$ we have a general form of $y(k, w)$ as in (4.4) where due to the non-linearity no solution in closed form exists.

Here the basic goal is to calculate $\hat{y}(k, w)$ perturbatively in powers of λ around the exact solution ($\lambda = 0$), where we assume that λ is a small parameter. We thus consider the general form of the solution (4.4) which can be expressed as

$$\hat{y}(k, w) = \sqrt{D}G(k, w)\hat{\eta}(k, w), \quad (4.7)$$

where $G(k, w)$ is the effective propagator and the perturbation expansion will lead to calculating contributions to (4.7) in powers of λ . This perturbation expansion can be computed using Feynman diagrams [17, 59], such a diagrammatic representation is shown in Figure 4.1 where the second integral in (4.4) can be represented by a vertex, see Figure 4.1(b).

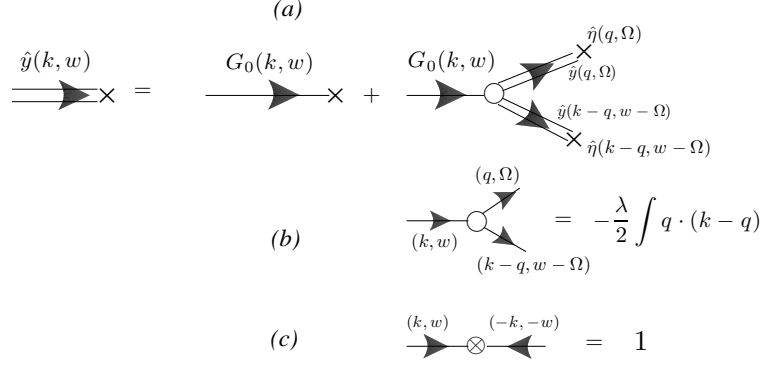


Figure 4.1: (a) Diagrammatic representation of Eq. (4.4) (taken from [17]). $G(k, w)$ is represented with a double arrow. Bare propagator $G_0(k, w)$ is represented with a single arrow. Each noise term appears as a \times symbol. (b) The integral over the variables q, Ω can be represented by a vertex. (c) Due to the Fourier transform of the noise and the δ correlations a conservation rule exists, where momenta going in are equal to momenta coming out.

As shown in Figure 4.1(a) a conservation rule is established, where the arguments of the integral sum up to (k, w) . We iterate the expansion by inserting the form of \hat{y} into the integrals of Eq. (4.4). This leads to the appearance of noise terms where after averaging, any odd number of noise terms disappear, and only an even number remain and give a Dirac δ function contribution.

The one iteration of (4.5) leads to

$$\hat{y}(k, w) = G_0(k, w) \left[\sqrt{D} \hat{\eta}(k, w) + \lambda N \left[G_0(k, w) [\hat{\eta}(k, w) + \lambda N [\hat{y}(k, w)]] \right] \right].$$

In the diagrammatic expansion a single iteration results in an one loop correction to (4.6), this is the perturbation expansion to order λ^2 and leads to the following corrections [17, 95], which are

$$\begin{aligned} \tilde{\nu} &= \nu \left[1 - \frac{\lambda^2 D}{2\nu^3} \frac{d-2}{4d} K_d \int_0^\psi ds s^{d-3} \right] \\ \tilde{\lambda} &= \lambda \\ \tilde{D} &= D \left[1 + \frac{\lambda^2 D}{2\nu^3} \frac{K_d}{4} \int_0^\psi ds s^{d-3} \right], \end{aligned} \quad (4.8)$$

where $K_d = S_d/(2\pi)^d$ and S_d is the surface area of a d -dimensional unit sphere.

The resulting integrals in (4.8) are then separated into two domains; one is the high frequency domain $[\psi/b, \psi]$ and the other is the low frequency domain

$[0, \psi/b]$ which contains a divergence term. This is the first step where all fast modes are removed. We find that the terms obtained from the expansion will diverge for $d < d_c = 2$ and we treat such a divergence by renormalizing the system. Since the first step changed the lattice space dx the second step is to use the self-affine transformation (4.1) to restore the original lattice spacing. This renormalization procedure leads to the renormalization group flow equations for the KPZ equation and can be found in [17, 95]. For a single iteration procedure, the one loop corrections to (ν, λ, D) are

$$\begin{aligned}\frac{d\nu}{d\ell} &= \nu \left[z - 2 + K_d \frac{\lambda^2 D}{\nu^3} \frac{2-d}{8d} \right], \\ \frac{d\lambda}{d\ell} &= \lambda [\alpha + z - 2], \\ \frac{dD}{d\ell} &= D \left[z - d - 2\alpha + \frac{\lambda^2 D}{\nu^3} \frac{K_d}{8} \right].\end{aligned}\tag{4.9}$$

Notice that as a result of the Galilean invariance property of the KPZ equation (2.1) which leads to the scaling relation $\alpha + z = 2$ we obtain no rescaling to the non-linear term λ .

In order to deduce the values of the scaling exponents (α, β, z) from (4.9) we introduce the mode coupling term $g^2 = \lambda^2 D / (2\nu^3)$, this satisfies

$$\frac{dg}{d\ell} = \frac{2-d}{2}g + K_d \frac{2d-3}{4d}g^3.$$

This equation has two fixed points $g_1 = 0$ and $g_2 = (2/K_d)^{1/2}$ and the second of these is a stable point [17]. Substituting g_2 into (4.9) and setting $dJ/d\ell = 0$, for $d = 1$ leads to the values of the scaling exponents as given in (2.3).

4.3 Mode coupling calculation

In this section we use a mode coupling method [6, 8], in order to compute analytical expression in $1 + 1$ dimensions for the correlation function Eq. (3.8). The scaling form of this has been shown in Eq. (3.9) with a similar result for ξ_{\parallel} . We also derive a representation for $\langle |\nabla y|^2 \rangle$ and the amplitude σ^2 (3.19).

The idea of the mode coupling approximation is that the properties of the solution to the KPZ equation (2.1) may be derived by first considering the linear Edwards-Wilkinson equation [48] i.e. Eq. (2.1) for $\lambda = 0$. We then employ the results from the renormalization group analysis, as shown in the previous section, to derive representations of scaling functions. In order to verify these representations, we

use the numerically measured coefficients $D/(2\nu)$ (3.16) and compare predictions to data from simulations of the δ -family of Eden models. We further consider the co-moving frame, so that $v_0 = 0$, and the equation then reads

$$\partial_t y(x, t) = \nu \Delta y(x, t) + \sqrt{D} \eta(x, t). \quad (4.10)$$

We denote by

$$\hat{y}(k, t) = \frac{1}{2\pi} \int_{-\infty}^{\infty} dx y(x, t) e^{-ikx}$$

the Fourier transform of the function $y(x, t)$. The evolution of the function $\hat{y}(k, t)$ satisfies

$$\partial_t \hat{y}(k, t) = -\nu k^2 \hat{y}(k, t) + \sqrt{D} \hat{\eta}(k, t). \quad (4.11)$$

Here $\hat{\eta}(k, t)$ is only the spatial Fourier transform of the white noise $\eta(x, t)$, where $\hat{\eta}(k, t)$ has a mean 0 with correlations

$$\langle \hat{\eta}(k, t) \hat{\eta}(k', t') \rangle = \frac{1}{2\pi} \delta(k + k') \delta(t - t'). \quad (4.12)$$

Solving the pde for \hat{y} in (4.11) leads to the expression

$$\hat{y}(k, t) = \sqrt{D} \int_0^t ds \hat{\eta}(k, s) e^{-\nu k^2(t-s)},$$

and subsequently the formal solution of (4.10) reads

$$y(x, t) = \sqrt{D} \int_{-\infty}^{\infty} dk e^{ikx} \int_0^t ds \hat{\eta}(k, s) e^{-\nu k^2(t-s)}. \quad (4.13)$$

For the mode coupling calculations we use the solution to the frequency space KPZ flow equations (4.9), which in $d = 1$ dimensions are given by [8, 17, 95, 124],

$$\begin{aligned} \nu(k) &= \nu_1 [(1 - \alpha_B) + \alpha_B/k]^{1/2}, \\ D(k) &= D_1 [(1 - \alpha_B) + \alpha_B/k]^{1/2}, \end{aligned} \quad (4.14)$$

and $\lambda(k) = \lambda_1$, where $k \sim b^{-1}$ and

$$\alpha_B = \frac{\chi \lambda_1^2 D_1}{4\pi^2 \nu_1^3}.$$

Here (λ_1, ν_1, D_1) are the parameters for $k \sim b^{-1} = 1$ where no renormalization has taken place. The relationship between k and b^{-1} has a proportionality constant χ and in [8] it is found to be approximately 1. For the δ -family of Eden models we also found it to be approximately 1, numerically we obtained 0.9722. In subsequent calculations below we keep the term χ in our expressions, since we compare our

exact results to numerical data. Note also the term $D/\nu = D_1/\nu_1$ is independent of the scale k . For convenience we express $\nu(k)$ in (4.14) as

$$\nu(k) = [A + B^2/(4k)]^{1/2}, \quad (4.15)$$

where $A = \nu_1^2(1 - \alpha_B)$ and $B = 2\nu_1\alpha_B^{1/2} = \frac{\sqrt{2\chi}}{\pi}\lambda\sqrt{D_1/2\nu_1}$. Note that in (4.15), the dominant term for $k^{-1} \sim b \gg 1$ is given by

$$\nu(k) \approx B/(2k^{1/2}).$$

We continue with a derivation of the correlation function $C(l, t)$.

4.3.1 Deriving the correlation function $C(l, t)$

The correlation function $C(l, t)$ defined in (3.8) can be represented as

$$C(l, t)^2 = \frac{2}{L} \int_0^L dx \langle y(x, t)^2 - y(l+x, t)y(x, t) \rangle. \quad (4.16)$$

Using the solution (4.13) we can compute

$$\begin{aligned} \frac{1}{L} \int_0^L dx \langle y(x+l, t)y(x', t) \rangle &= \frac{1}{L} \int_0^L dx \left\langle \int_{-\infty}^{\infty} \int_{-\infty}^{\infty} dk dk' e^{ik(l+x)} e^{ik'x} \int_0^t \int_0^t \right. \\ &\quad \left. \hat{\eta}(k, s) \hat{\eta}(k', s') e^{-\nu k^2(t-s)} e^{-\nu k'^2(t-s')} ds ds' \right\rangle. \end{aligned} \quad (4.17)$$

Taking the expectation, we have

$$\frac{1}{L} \int_0^L dx \langle y(x+l, t)y(x', t) \rangle = \frac{D}{2\pi} \int_{-\infty}^{\infty} e^{ikl} \int_0^t e^{-\nu k^2(2t-2s)} ds dk,$$

and evaluating the inner integral leads to

$$\frac{1}{L} \int_0^L dx \langle y(l+x, t)y(x, t) \rangle = \frac{D}{2\nu\pi} \int_0^{\infty} dk \frac{\cos(kl)}{k^2} [1 - e^{-2\nu k^2 t}], \quad (4.18)$$

where we have used that the Fourier transform is even in k . Taken together with the expression for $\int_0^L dx \langle y(x, t)^2 \rangle / L$ leads to the correlation function (4.16) of the Edwards-Wilkinson equation

$$C(l, t)^2 = \frac{D}{\nu\pi} \int_0^{\infty} dk k^{-2} (1 - \cos(kl)) [1 - e^{-2\nu k^2 t}]. \quad (4.19)$$

In order to compute the correlation function for the KPZ equation (2.1) we substitute the length scale dependent parameters $D(k)$ and $\nu(k)$ into (4.19), only considering the most dominant terms, we obtain

$$C(l, t)^2 = \frac{D_1}{\nu_1\pi} \int_0^{\infty} dk k^{-2} (1 - \cos(kl)) [1 - e^{-Bk^{3/2}t}]. \quad (4.20)$$

If we take $t \rightarrow \infty$ in Eq. (4.20) we get

$$C(l, t)^2 \rightarrow \frac{D_1}{\nu_1 \pi} \int_0^\infty dk k^{-2} (1 - \cos(kl)) = \frac{D_1}{2\nu_1} l. \quad (4.21)$$

Using $D/\nu = D_1/\nu_1$, we have

$$C(l, t) \approx \left(\frac{D}{2\nu} l \right)^{1/2} \quad \text{for } l \ll \xi_{\parallel}(t). \quad (4.22)$$

For finite time, numerical integration of (4.20) in the large l limit gives

$$\lim_{l \rightarrow \infty} C(l, t)^2 \approx 2.7 \frac{D}{\nu \pi} (Bt)^{2/3}.$$

Together with the definition (3.8) of the correlation length this leads to

$$\lim_{l \rightarrow \infty} C(l, t) \approx \left(5.4 \times 2^{1/3} \chi^{1/3} \left(\frac{D}{2\nu} \right)^{4/3} \pi^{-5/3} (\lambda t)^{2/3} \right)^{1/2}. \quad (4.23)$$

To obtain the expression for the lateral correlation length we have (4.22) for $l \ll \xi_{\parallel}(t)$, and so at $l = \xi_{\parallel}(t)$ the following holds,

$$\left(\frac{D}{2\nu} \xi_{\parallel}(t) \right)^{1/2} = \left(5.4 \times 2^{1/3} \chi^{1/3} \left(\frac{D}{2\nu} \right)^{4/3} \pi^{-5/3} (\lambda t)^{2/3} \right)^{1/2}$$

and this leads to

$$\xi_{\parallel}(t) \approx 5.4 \times 2^{1/3} \chi^{1/3} \left(\frac{D}{2\nu} \right)^{1/3} \pi^{-5/3} (\lambda t)^{2/3}. \quad (4.24)$$

4.3.2 Deriving $\langle |\nabla y|^2 \rangle$

In order to compute $\langle |\nabla y|^2 \rangle$ for the 1 + 1 dimensional KPZ equation (2.1) we first obtain $\langle |\nabla y|^2 \rangle$ for the EW equation (4.10). Define

$$\frac{\partial y}{\partial x} = \int_{-\infty}^{\infty} ik \hat{y}(k, t) e^{ikx} dk$$

and using (4.13) we get

$$\left\langle \left(\frac{\partial y}{\partial x} \right)^2 \right\rangle = -D \left\langle \int_{-\infty}^{\infty} \int_{-\infty}^{\infty} dk dk' k k' e^{ikx} e^{ik'x} \int_0^t \int_0^t ds ds' \hat{\eta}(k, s) \hat{\eta}(k', s') e^{-\nu k^2(t-s)} e^{-\nu k'^2(t-s')} \right\rangle.$$

Taking the expectation into the integral leads to

$$\left\langle \left(\frac{\partial y}{\partial x} \right)^2 \right\rangle = \frac{D}{2\pi} \int_{-\infty}^{\infty} dk k^2 \int_0^t ds e^{-\nu k^2(2t-2s)}$$

evaluating the integral we have

$$\left\langle \left(\frac{\partial y}{\partial x} \right)^2 \right\rangle = \frac{D}{2\nu\pi} \int_0^\infty dk [1 - e^{-2\nu k^2 t}].$$

In this form we can now use the mode coupling technique. We substitute in $D(k)$ and $\nu(k)$ from (4.14) and only consider the dominant terms, this leads to

$$\left\langle \left(\frac{\partial y}{\partial x} \right)^2 \right\rangle = \frac{D_1}{2\nu_1\pi} \int_{\psi_1}^{\psi_2} [1 - e^{-Bk^{3/2}t}] dk. \quad (4.25)$$

Here we are using the coarse-grained frequency interval $[\psi_1, \psi_2]$ where $dx \sim 1/\psi_2$ is the lattice spacing and $L \sim 1/\psi_1$ is the upper length cutoff for a system of size L . In particular we discretise the system, such that we now look at the discrete Fourier transform, namely for periodic boundary conditions in the strip geometry we have

$$\left\langle \left(\frac{\partial y}{\partial x} \right)^2 \right\rangle = \frac{D_1}{\nu_1 L} \sum_{m=0}^{L/2} [1 - e^{-Bk_m^{3/2}t}], \quad (4.26)$$

where $k_m = 2\pi m/L$ and we have used that the Fourier transform is even in k and for simplicity we took $dx \rightarrow 0$. Note that by taking t large we retrieve

$$\left\langle \left(\frac{\partial y}{\partial x} \right)^2 \right\rangle = \frac{D_1}{\nu_1 L} \sum_{m=0}^{L/2} = \frac{D_1}{2\nu_1}.$$

This expression is consistent with taking $l = 1$ in (4.22), for a discrete difference differential. In order to find a t dependent expression of (4.26), we re-arrange

$$\left\langle \left(\frac{\partial y}{\partial x} \right)^2 \right\rangle - \frac{D_1}{2\nu_1} = -\frac{D_1}{\nu_1 L} \sum_{m=0}^{L/2} e^{-Bk_m^{3/2}t}, \quad (4.27)$$

we take $u = Bt(2\pi/L)^{3/2}$ and $L \rightarrow \infty$. The sum in (4.27) will only have a significant contribution if m is large, and in this regime we can approximate the sum as an integral, so that we now have

$$\left\langle \left(\frac{\partial y}{\partial x} \right)^2 \right\rangle - \frac{D_1}{2\nu_1} = -\frac{D_1}{\nu_1 L} \int_0^\infty e^{-um^{3/2}} dm.$$

Numerically integrating leads to

$$\left\langle \left(\frac{\partial y}{\partial x} \right)^2 \right\rangle - \frac{D_1}{2\nu_1} = -\frac{D_1}{\nu_1 L} \frac{2}{3} \left((2\pi/L)^{3/2} Bt \right)^{-2/3} 1.35412,$$

and we have the following time dependent behaviour

$$\langle |\nabla y|^2 \rangle \approx \frac{D_1}{2\nu_1} - 0.902736 \left(\frac{D_1}{2\nu_1} \right)^{2/3} \pi^{-1/3} 2^{-1/3} \chi^{-1/3} \lambda^{-2/3} t^{-2/3}. \quad (4.28)$$

4.3.3 Deriving the prefactor σ_δ^2

Here we use the mode coupling calculation to find the coefficient σ_δ^2 of the mean squared displacement $M(h)$ as defined in (3.18) for the boundary process $(X_h : h \geq 0)$. As shown in (3.20) the evolution of the boundary as a function of height h is

$$\frac{dX_h}{dh} = -\frac{\partial y(X_h, h)}{\partial x}. \quad (4.29)$$

In order to motivate our method, consider a Brownian motion B_h with evolution equation of the form

$$\frac{dB_h}{dh} = \eta(h), \quad (4.30)$$

where $\eta(h)$ is a mean zero white noise process. Representing (4.30) in integral form we have

$$B_h = \int_0^h \eta(s) ds,$$

and in order to compute $M(h)$ we take

$$\langle B_h^2 \rangle = \left\langle \int_0^h \int_0^h \eta(s) \eta(s') ds ds' \right\rangle$$

which leads to $\langle B_h^2 \rangle = h$. Thus we compute the $M(h)$ of X_h by taking

$$M(h) = \sigma^2 h^{4/3} = \int_0^h \int_0^h ds ds' \langle u(x, s) u(x', s') \rangle, \quad (4.31)$$

where $u(\cdot, \cdot) = -\frac{\partial y(\cdot, \cdot)}{\partial x}$. Note that (4.31) has a spatial component which will contribute to the prefactor σ^2 . For convenience we take $x = x'$ and approximate this multiplicative factor by considering the spatial fluctuations of the boundary per unit growth event, this leads to

$$\epsilon^2 = \frac{1}{\pi_b - \pi_a} \int_{\pi_a}^{\pi_b} d\theta \cos^2(\theta),$$

by choosing the values of $\pi_a \approx 0.19\pi$ and $\pi_b \approx 0.81\pi$ we have $\epsilon^2 \approx 0.2613$. Note that we have chosen these values for the wedge $[\pi_a, \pi_b]$ since it corresponds well to the data.

We first compute $\langle \frac{\partial y(x, s)}{\partial x} \frac{\partial y(x, s')}{\partial x} \rangle$ for (4.13),

$$\begin{aligned} \left\langle \frac{\partial y(x, s)}{\partial x} \frac{\partial y(x, s')}{\partial x} \right\rangle &= -D \left\langle \int_{-\infty}^{\infty} \int_{-\infty}^{\infty} dk dk' k k' e^{ikx} e^{ik'x} \int_0^s \int_0^{s'} du dv \right. \\ &\quad \left. \hat{\eta}(k, u) \hat{\eta}(k', v) e^{-\nu k^2(s-u)} e^{-\nu k'^2(s'-v)} \right\rangle. \end{aligned} \quad (4.32)$$

Taking the expectation into the integral, evaluating the noise and taking $s > s'$ leads to

$$\left\langle \frac{\partial y(x, s)}{\partial x} \frac{\partial y(x, s')}{\partial x} \right\rangle = \frac{D}{2\pi} \int_{-\infty}^{\infty} dk k^2 \int_0^{s'} du e^{-\nu k^2 (s+s'-2u)},$$

integrating with respect to u gives

$$\left\langle \frac{\partial y(x, s)}{\partial x} \frac{\partial y(x, s')}{\partial x} \right\rangle = \frac{D}{2\nu\pi} \int_0^{\infty} dk [e^{-\nu k^2 (s-s')} - e^{-\nu k^2 (s+s')}]. \quad (4.33)$$

We now implement the mode coupling approximation, substituting in $D(k)$ and $\nu(k)$ from (4.14) into (4.33) and considering only the dominant terms, leads to

$$\left\langle \frac{\partial y(x, s)}{\partial x} \frac{\partial y(x, s')}{\partial x} \right\rangle = \frac{D_1}{2\nu_1\pi} \int_0^{\infty} [e^{-Bk^{3/2}(s-s')/2} - e^{-Bk^{3/2}(s+s')/2}] dk,$$

and numerically integrating

$$\left\langle \frac{\partial y(x, s)}{\partial x} \frac{\partial y(x, s')}{\partial x} \right\rangle \approx 0.90(B/2)^{-2/3} \frac{D_1}{2\nu_1\pi} [(s-s')^{-2/3} - (s+s')^{-2/3}].$$

Inserting this expression into (4.31), evaluating the double integral and combining everything gives

$$M(h) = 1.5032\epsilon^2 \left(\frac{D_1}{2\nu_1} \right)^{2/3} \pi^{-1/3} 2^{1/3} \chi^{-1/3} \lambda^{-2/3} h^{4/3}. \quad (4.34)$$

Note that our calculation shows agreement with numerical measurements (3.19) that $M(h) \sim h^{2H}$ with Hurst exponent $H = 2/3$.

The term λ in (2.1) represents lateral growth, in order to approximate the value of this we use the following geometrical argument. Consider the magnitude of the surface increase in a single growth event, since growth occurs locally perpendicular to the interface

$$\lambda \approx \frac{1}{\pi_b - \pi_a} \int_{\pi_a}^{\pi_b} d\theta \sin(\theta) \approx 0.85,$$

where as above we use the values $\pi_a \approx 0.19\pi$ and $\pi_b \approx 0.81\pi$. This value of λ agrees well with other surface measurements. For example, as shown in Chapter 2 the mean velocity of a KPZ surface is (2.7)

$$\langle y \rangle / t = v_0 + \frac{\lambda}{2} \langle (\nabla y)^2 \rangle.$$

and using (4.28) gives for large t

$$\lim_{t \rightarrow \infty} \langle y \rangle / t \approx v_0 + \frac{\lambda}{2} \left(\frac{D_1}{2\nu_1} \right). \quad (4.35)$$

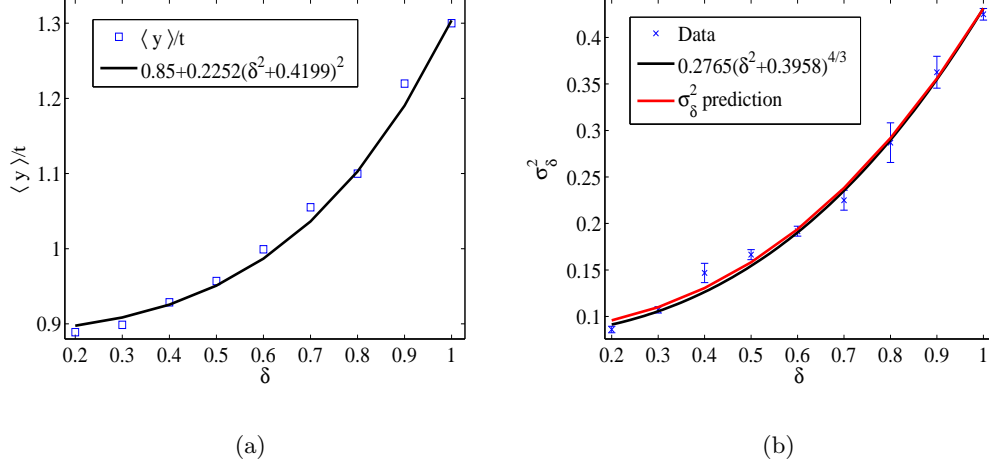


Figure 4.2: (a) Coefficient of the average surface height (2.7). For large times the mean $\langle y \rangle$ becomes linear and the prefactor follows the prediction (4.36) well. Here we find the prefactor of $\langle y \rangle$ by averaging over a window for large t , for a system size $L = 1500$ and 100 independent samples. (b) Coefficient of the mean square displacement of domain boundaries as shown in Figure 3.8. Here the red curve is the theoretical prediction (4.37) derived using the mode coupling technique. We see that it follows the data well and is almost exactly the same as the previous numerical fit (3.19) shown as the black curve.

In KPZ growth models the lateral growth rule leading to a Galilean invariant system leads to the appearance of an additive term v_0 and the gradient squared term multiplied by λ in the KPZ equation (2.1) being coupled as seen in [63, 95]. Through their derivation, we see that v_0 is approximately λ [17, 95]. In (4.35) we therefore have with (3.16) and $\lambda \approx 0.85$

$$\lim_{t \rightarrow \infty} \langle y \rangle/t \approx 0.85 + 0.2252(\delta^2 + 0.4194)^2. \quad (4.36)$$

In Figure 4.2(a) we compare this prediction to the measured values of the velocity and we see that the prediction works well with the data.

For σ_δ^2 we substitute into (4.34) the numerical values of χ , λ and ϵ and the form of $D/(2\nu)$ as in (3.16) giving

$$\sigma_\delta^2 \approx 0.2685(\delta^2 + 0.4194)^{4/3}. \quad (4.37)$$

In Figure 4.2(b) we compare this prediction to the prefactor of $M(h)$ as measured in Section 3.3.2 and shown in Figure 3.8. We can see that the prediction (4.37) agrees well with the data measured and the previously fitted curve (shown in black).

4.4 Conclusion

In this chapter we have shown how to obtain the scaling exponents of the KPZ universality class for $d = 1$ using a dynamic renormalization group method on the KPZ equation, which has been done before in [17, 95]. This method gives values of the exponents which agree with previous approaches shown in Chapter 2. By combining the flow equations for the parameters (ν, λ, D) with a mode coupling approach we have derived analytical forms for the expressions of the correlation function (3.8), the lateral correlation length (3.10), the $\langle |\nabla y|^2 \rangle$ term and coefficient σ_δ^2 of the boundary (3.19). The first two of these four have appeared in [6]. Although in computing σ_δ^2 we had to choose values for the wedge $[\pi_a, \pi_b]$, however, these values were also used in the calculation for (4.36) and both computations agree with the numerical data. The computation of the $M(h)$ (4.31) also shows the right exponent $H = 2/3$. In addition, we found a very good agreement with the simulation results for the data shown in Chapter 3 and our analysis demonstrates the relationship between the δ -family of Eden models and the hydrodynamical parameters (ν, λ, D) of the KPZ equation (2.1).

Chapter 5

Scale invariant growth processes in expanding space

5.1 Introduction

Non-equilibrium growth and spreading phenomena are ubiquitous processes in nature. Many examples are observed across different systems with a wide range of kinetic growth rules [177]. Key questions in the area attempt to investigate the inter-particle interactions, dependencies of particle dynamics on the growth rules and pattern formation. Typical patterns observed range from dendrite [170, 200], fractal [73, 121, 140], spiral and oscillatory [90, 146, 171] to branching and tree-like structures [28, 191]. In these systems the underlying geometry of the embedding space introduces added complexity to the behaviour observed [126], where the emergence of an isotropic behaviour of a given surface enclosing a region is modified by simply varying the growth space. This implies obvious changes in the overall morphology, but somewhat surprisingly, the statistics of the surface and inherent behaviour observed within the region change as well [9, 118]. Such behaviour can be seen from both experimental and theoretical studies [195]. For instance as discussed in Chapter 2, in the KPZ universality class models with flat initial surface the fluctuations have a Tracy-Widom distribution for the largest eigenvalue of GOE, in contrast to a GUE Tracy-Widom distribution for models with curved initial conditions [55, 181].

A particularly interesting regime emerges when competition is introduced into a model through allowing the propagation of several phases, providing a possible description of the patterns encountered in the growth of microbial colonies [5, 45, 155]. The indications are that the dynamical competition between distinct

and fluctuating patterns plays a key role in the kinetics leading to the final morphology as seen for the case of two species growth as in Chapter 3. Although the growth rules leading to the Eden interface are simple, the asymptotic behaviour is representative for all systems in the same universality class, characterized by a propagating front over two types of phases, which are non-mixing [178]. Despite these simple kinetics, the dynamical behaviour of each phase depends sensitively on the curvature of the surface, which has an effect on the power-law exponent of the mean squared displacement. Where as seen numerically in Chapter 3 and derived theoretically in Chapter 4, the meandering of the boundary of these phases deviates from the dynamics of a Brownian motion and has a super diffusive Hurst exponent of $2/3$ [6, 45].

In this chapter we discuss general scale invariant directed structures, many diverse forms of which are found across nature. Some examples include, DLA [192, 193, 216], domain boundaries of crystal growth [177], viscous fingering [160, 176, 197] and microbial growth [5, 6]. In such systems the scale invariant properties emerge from local rules describing particle interactions, these rules then dominate behaviour on larger length scales. We study such structures through modelling domain boundaries as trajectories of locally interacting particles with random motion. Such a treatment can be applied to many types of system which appear ubiquitously in nature, one being the landscape of river networks [191] and another the modelling of competition in populations of micro-organisms, as the colonies discussed in Chapter 3.

Depending on the particular application, the system exhibits different interactions between particles. Typical interactions for phase boundaries are coalescence $A + A \rightarrow A$ or annihilation $A + A \rightarrow \emptyset$, both of which can be usually understood by simple mean field scaling results [180]. Determining the dynamical behaviour in a closed form can however depend on several factors such as embedding geometry, system size and space-time symmetries. Understanding how these effects interplay to affect macroscopic observables is of much interest for the understanding of several physical processes, such as diffusion transport, diffusion controlled reactions and aggregation structure formation [17, 29, 110].

Although the motion of particles on a fixed domain such as the strip geometry has been looked at extensively [4, 148], in natural systems particles often interact on dynamic geometries. In such cases their behaviour can no longer be described by the classical motion of particles moving on a straight line. A case which is of much interest in this chapter, is how the particle movements and interactions are affected by being embedded in different geometries. The indications are that the

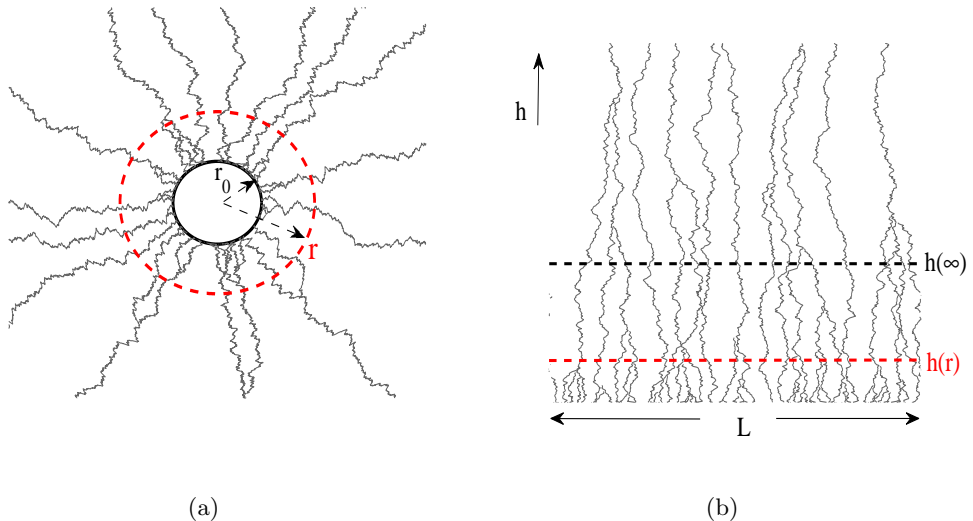


Figure 5.1: Expanding radial growth structure and the same structure on a fixed domain with periodic boundary conditions, illustrated for the case of coalescing Brownian motion. The distribution of the rescaled structure at radius r is identical to the distribution of the fixed domain structure at height $h(r)$ as given by (5.4), indicated by a dashed red line. This mapping (plotted in Figure 5.3) has a finite limit $h(\infty)$. Parameters are $L = 100$ with $r_0 = L/2\pi$, unit diffusion coefficient and initially 100 arms.

geometry plays a key role on the kinetics of fluctuating particles [5, 47, 126], leading to a deviation from the usual mean field results (cf. Figure 5.2).

To see to what extent the role of the embedding space influences the interaction between particles we compare behaviour between time-dependent domains and fixed domains. In this chapter, the behaviour on the fixed domain is used as a special reference to which we will compare behaviour from other geometries. For the fixed domain, statistics such as the number of particles or the inter-particle distance function have been extensively analysed and one is able to make predictions on not just the asymptotic behaviour but also on the dynamical behaviour [4, 180].

To describe our results in the most illustrative setting, we consider the growth of self-affine structures (e.g., domain boundaries) in isoradial geometry mainly in two dimensions. These structures consist of directed “arms”, which can be interpreted as locally scale invariant space-time trajectories of point particles moving in an expanding one dimensional space with periodic boundary conditions. For exam-

ple, Figure 5.1 illustrates the motion of diffusing particles which interact through coalescence which either move on a radially expanding domain or a fixed domain on a continuous sub-space of \mathbb{R}^2 . In the fixed domain case Figure 5.1(b) as a function of height h (vertical axis), the trajectories move in the lateral x direction. Each particle index with a label $i \in \{1, N(0)\}$ has an initial random displacement $x_i(0) \in [0, L)$, where $N(0)$ is the initial number of particles. As time h progresses, the particles perform a random motion subject to $x_i(h) \in [0, L)$, with periodic boundary conditions on the edges of the strip. This behaviour will form the basis of our study and has been investigated extensively many times. Figure 5.1(a) on the other hand, displays the trajectories of coalescing particles which reside on the surface of a one dimensional sphere, this space expands radially with radius $r \geq r_0$. The particles indexed $i \in \{1, N(0)\}$ are fixed on to the growing circumference and move laterally along the surface, where for all r the particle displacement is $y_i(r) \in [0, 2\pi r)$. In order to connect the two structures we take $r_0 = L/(2\pi)$ and both have the same initial number of particles. The asymptotic behaviour is dependent upon the geometry where for the radial structure the expanding embedding space plays a critical role on observable statistics, as illustrated in Figure 5.2(a).

In this chapter we focus solely on the unbiased case of stochastic motion, this is when particles have no drift and we consider several diffusive or super (sub) diffusive processes moving on a particular geometry. We use the fact that independent of the embedding geometry the local scale invariance properties hold for these processes to derive a mapping between growth phenomena in fixed and time-dependent domains (see Figure 5.2(b)). We exploit the absence of characteristic length and time scales to provide a simple and elegant theory, which applies directly to system of particles which exhibit interaction that is itself scale-free. This allows us to characterize reactions such as coalescence, annihilation or exclusion of point particles. We also extend our theory to discuss how non-zero interaction length scales can be treated such as non-zero particle diameter or particle branching. For particle motion we will consider three important scale invariant processes, these are Brownian motion, α -stable Lévy processes and fractional Brownian motion (fBm). The first two are Markovian, for which the mapping can be derived rigorously and for the non-Markovian fBm, correlations lead to a correction which we compute explicitly in Chapter 6.

This chapter is organized as follows, in Section 5.2 we derive the mapping function based on the preservation of local scaling laws and we give a detailed explanation on its properties. In Section 5.3 the mapping is applied to radially expanding structures and is mapped to structures in the fixed domain, here we

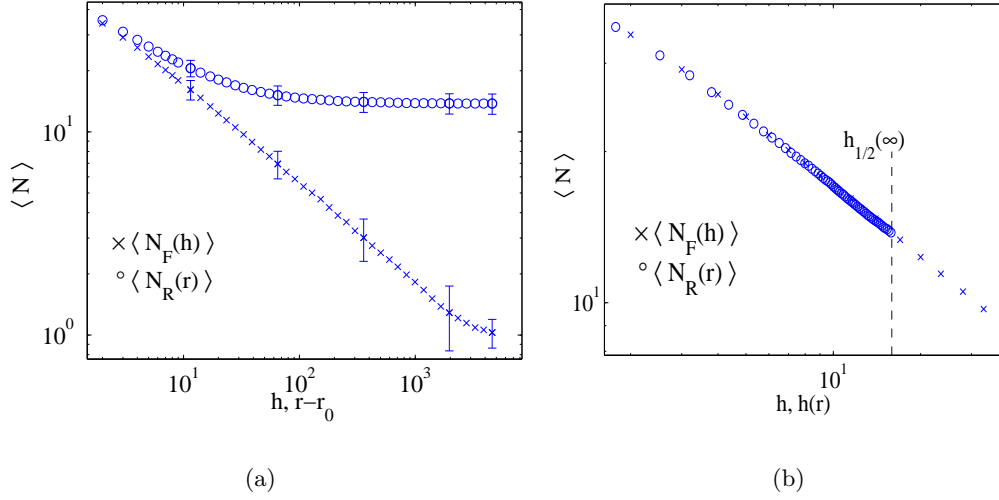


Figure 5.2: Illustration of geometrical affects of expanding domains for coalescing Brownian motions. We compare the average number of particles $\langle N \rangle$ in a fixed domain $[0, L)$ (\times) and in a radially expanding domain $[0, 2\pi r)$ (\circ) for $r \geq r_0$. For comparison we take $r_0 = L/2\pi$, where $L = 100$ and an initial number of 100 particles. (a) In the fixed domain, $\langle N_F(h) \rangle$ decreases to the value 1 corresponding to the absorbing state of the system (called fixation). However, in the corresponding radially expanding domain $\langle N_R(r) \rangle$ decreases to a value greater than 1. Data shown with error bars equal to the standard deviation. (b) Using the mapping (5.4) with $\gamma = 1/2$, we plot $\langle N_R(r) \rangle$ against $h(r)$ and get a data collapse. The value $h_{1/2}(\infty) = r_0$ is given in (5.6).

look at point particles. In Section 5.4 we extend our theory to describe isotropic structures which reside on a general time-dependent domains, here we also generalize our theory to consider expanding $n+1$ dimensional structures. Lastly in Section 5.5, we look at how to map behaviour in systems which exhibit non-local interactions such as when particles have a non-zero size or when particles can branch. These systems are very common in the real world (see [17, 88, 103, 149, 162, 176] for a more general overview) and thus an important extension of our theory.

5.2 Main results

In this section, we show the derivation of a mapping which maps behaviour between expanding structures and structures in the fixed domain as illustrated in Figure 5.1. For simplicity of presentation we focus on the radial geometry with radius $r(t) =$

$r_0 + t$ and compare it to a strip geometry. Extensions to more general geometries can be found in Section 5.4.

5.2.1 Mapping

Consider an isotropic radial structure with initial radius r_0 as shown in Figure 5.1(a), which is a particular example of radially coalescing Brownian motion. We consider directed radial growth where the displacement of each arm along the perimeter of the growing circle can be represented as

$$Y_r \in [0, 2\pi r) \quad \text{with} \quad r \geq r_0 \quad (5.1)$$

as a function of the radial distance r . In the analogous fixed domain geometry Figure 5.1(b), we model a single arm of a growth structure as a stochastic process $X := (X_h, h \geq 0)$ such that

$$X_h \in [0, L), \quad \text{and} \quad h \geq 0$$

with periodic boundary conditions at the edges. In order to connect the two geometries we take $r_0 = L/2\pi$. In each geometry the arms are taken to share the same local scale invariance property. Namely taking x, y as the lateral displacement of the process X and Y , respectively, we have

$$dx \sim (dh)^\gamma \quad \text{and} \quad dy \sim (dr)^\gamma, \quad (5.2)$$

where $\gamma > 0$ and proportionality constants in both cases are the same. Generic examples are self-similar processes where $(X_{bh}, h \geq 0)$ is distributed as $(b^\gamma X_h, h \geq 0)$ for all $b > 0$, such as fBm [21], or α -stable Lévy processes [34], which will be discussed later in more detail. Consider now the following coordinate transformation between the two geometries, (x, h) and (y, r) . Similar to the usual polar coordinates transformation, we have

$$x = \frac{r_0}{r} y, \quad (5.3)$$

so that now the rescaled radial arm has the same displacement domain as the fixed arm. Using (5.2) and (5.3) we have

$$\frac{dh}{dr} = \left(\frac{dx}{dy} \right)^{1/\gamma} = \left(\frac{r_0}{r} \right)^{1/\gamma},$$

and therefore

$$h(r) = \int_{r_0}^r \left(\frac{r_0}{s} \right)^{1/\gamma} ds = \begin{cases} \frac{\gamma}{1-\gamma} r_0 \left[1 - \left(\frac{r_0}{r} \right)^{\frac{1-\gamma}{\gamma}} \right], & \gamma \neq 1 \\ r_0 \log \left(\frac{r}{r_0} \right), & \gamma = 1 \end{cases}. \quad (5.4)$$

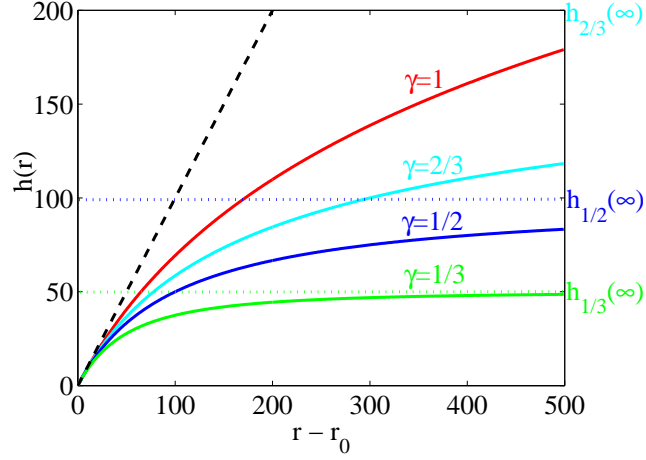


Figure 5.3: The mapping (5.4), for several values of γ , with $r_0 = 100$. Initially the mapping $h(r)$ behaves as the identity $r - r_0$ (black dashed line) and converges to the limit $h_\gamma(\infty) = r_0\gamma/(1 - \gamma)$ (color dotted) as $r \rightarrow \infty$. The value $h_\gamma(\infty)$ corresponds to the height h in the fixed domain where the behaviour is equivalent to $r \rightarrow \infty$ in the radially growing structure. (See also Figure 5.2).

For a single arm matching the initial condition $Y_{r_0} = X_0$ leads to an identical distribution

$$\frac{r_0}{r} Y_r \stackrel{\text{dist.}}{=} X_{h(r)},$$

for all $r \geq r_0$. Our main result is now that the same holds for the entire growth structure which is characterized as a collection of arms $\{Y_r\}$ and $\{X_h\}$:

$$\left\{ \frac{r_0}{r} Y_r \right\} \stackrel{\text{dist.}}{=} \{X_{h(r)}\} \quad \text{for all } r \geq r_0, \quad (5.5)$$

provided that the arms interact locally. Examples of such interactions include coagulation, annihilation or exclusion. Figure 5.1 illustrates the correspondence given by the mapping for coalescing Brownian motions, where the red dashed line indicates where the distribution of the two structures are equal.

5.2.2 Basic properties of the mapping

Figure 5.3 shows the mapping function (5.4) for several values of γ . For $r \rightarrow r_0$ we have $h(r) \simeq r - r_0$, for all $\gamma > 0$, so that initially there is no effect on the particles from the expanding domain, since for r close to r_0 , the fixed and the radial domain are locally equivalent. The non-linear behavior of $h(r)$ encodes the effect of the

expanding geometry, where for $\gamma > 0$, the large r behaviour is

$$h_\gamma(\infty) = \lim_{r \rightarrow \infty} h(r) = \begin{cases} \frac{\gamma}{1-\gamma} r_0, & \gamma < 1 \\ \infty, & \gamma \geq 1 \end{cases}. \quad (5.6)$$

The behaviour of the fixed structure at height $h_\gamma(\infty)$ is equivalent to the infinite radius behaviour of the radially growing structure (see Figure 5.1). This asymptotic behaviour is dependent on the value of γ , and for $\gamma < 1$ will differ from the analogous asymptotic behaviour in the fixed domain. For fixed structures it is known that fixation always occurs for interactions with an absorbing state such as coagulation or annihilation. This fixation state is due to the finite size of the system, where as $h \rightarrow \infty$ with probability one there will be one or no arm remaining for coalescing or annihilating structures, respectively, see Figure 5.2(a).

Coalescing or annihilating structures in the fixed domain $[0, L)$ are observed in neutral models for competition in spatial populations, such as the ones described in Chapter 3. The fixation time τ to reach the absorbing state scales with the size L of the system, where by standard arguments

$$\tau \sim L^{1/\gamma} \sim r_0^{1/\gamma}.$$

For large systems ($L, r_0 \rightarrow \infty$), typically τ is much larger than $h_\gamma(\infty) \sim r_0$, leading to a non-trivial limit for the statistics of the radial process. This is because for structures with $\gamma < 1$, the expansion rate of space, which is linear in r exceeds the lateral spread of random wandering of the particles, where due to the increasing distance between particles, eventually they no longer interact and the probability of fixation occurring is very low. So the statistics for these sub-ballistic structures such as the number of particles no longer change and reach a value which is random, as indicated by the non-zero standard deviation in Figure 5.2(a). In fact the whole rescaled structure converges to a non-trivial limit where

$$\left\{ \frac{r_0}{r} Y_r \right\} \xrightarrow{\text{dist.}} \{X_{h_\gamma(\infty)}\} \quad \text{as } r \rightarrow \infty.$$

For structures with $\gamma \geq 1$, the particle motion is equivalent to a (super) ballistic trajectory which exceeds the spatial expansion, where from (5.6) we have $h_\gamma(\infty) = \infty$. Here, despite the continuous expansion in space, the asymptotic behaviour for the rescaled radial process will be the same as the analogous behaviour in the fixed domain and we have

$$\left\{ \frac{r_0}{r} Y_r \right\} \xrightarrow{\text{dist.}} \{X_\infty\} \quad \text{as } r \rightarrow \infty.$$

Therefore for structures with $\gamma \geq 1$ fixation will always occur with probability 1. We can also express the mapping (5.4) independently of the system size. Introducing dimensionless variables $r' = r/r_0$ and $h' = h/r_0$ leads to

$$h'(r') = \begin{cases} \frac{\gamma}{1-\gamma} \left(1 - (1/r')^{\frac{1-\gamma}{\gamma}}\right) & , \gamma \neq 1 \\ \log(r') & , \gamma = 1 \end{cases}, \quad (5.7)$$

for all $r' \geq 1$, where for $\gamma = 1$ we recover the generic conformal map from the exterior of the unit circle to a strip. This notation shows that r_0 plays merely the role of a length scale, and γ is the only important parameter of the mapping.

5.3 Applications to self-similar models

In this section, we use the mapping (5.4) to characterize radially growing structures as time-rescaled structures in the fixed domain. These systems consist of space-time trajectories of point particles and we focus on coalescence as an example of local interaction. Where in simulations when a particle jumps over another it is removed from the list of all particles. We illustrate the use of (5.4) on structures where the arms are distributed according to either fractional Brownian motion (fBm) [21, 43, 68], or α -stable Lévy process [11, 34].

The fBm $B^H = (B_t^H, t \geq 0)$ with Hurst exponent $H \in (0, 1)$ is a centered Gaussian process with continuous paths and variance

$$\langle (B_t^H)^2 \rangle = \sigma^2 t^{2H}.$$

The process B^H exhibits local scale invariance (5.2) with $\gamma = H$ and when $H = 1/2$, the process is a standard Brownian motion. The α -stable Lévy process is a good model for structures where the position of the arms exhibit super-diffusive behaviour due to jumps in their trajectories [30, 58, 185]. An α -stable Lévy process $L^\alpha = (L_t^\alpha, t \geq 0)$ is a stochastic process with $\alpha \in (0, 2)$, it has stationary independent increments. These processes are Markovian with discontinuous paths and increments with infinite variance, and when $\alpha \in (0, 1)$ their absolute first moment will also be infinite. Another key property is that the fractional moments of L_t^α scale as

$$\langle |L_t^\alpha|^q \rangle \propto (\sigma_\alpha t)^{q/\alpha}, \quad (5.8)$$

where $0 < q < \alpha$ [30, 75, 144]. In practice, the parameter α can be greater than 2, but in this case the increments dL_t^α have finite mean and variance, and such a process scales as a Brownian motion. α -stable Lévy processes satisfy (5.2) with

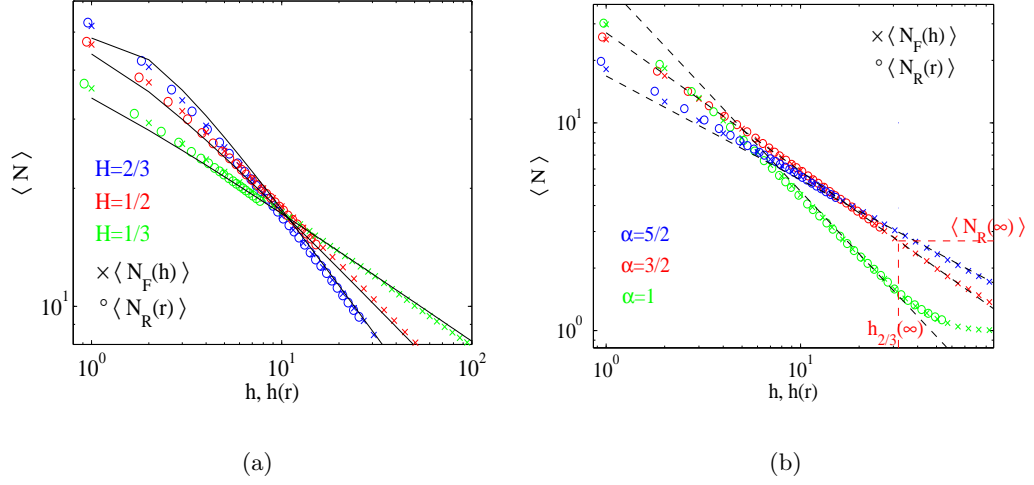


Figure 5.4: Numerical confirmation of the mapping (5.4) between radial geometry (\circ) and fixed domain (\times) for $\langle N \rangle$: (a) Particles perform fBm with $\gamma = H$. (b) Particles perform α -stable Lévy process with $\gamma = \max\{1/\alpha, 1/2\}$. Data is gathered for $L = 100$ with $r_0 = L/2\pi$ and 100 initial particles. Solid black lines indicate exact predictions (see Section 6.3.1) and dashed lines indicate predictions for the long time state of the system (see Section 6.3.2). The asymptotic behaviour (5.14) is illustrated for the $\alpha = 3/2$ data in (b) by a red dashed line.

$\gamma = \max\{1/\alpha, 1/2\}$. A more detailed description of both fBm and the α -stable Lévy process is given later in Section 6.2.

For simulations, at each time increment we take the absolute value of dL_t^α to be distributed by the Pareto distribution with pdf

$$p_\alpha(x) = \alpha b^\alpha / x^{\alpha+1} \quad \text{for } x \geq b, \quad (5.9)$$

where $b = dt^{1/\alpha}$ and dt being the simulation time-increment.

For illustration we will show data such as the average number of particles, denoted as $\langle N \rangle$ and the average inter-particle distance squared, denoted as $\langle D^2 \rangle$ and defined as

$$D^2 = \sum_{i=1}^N (x_{i+1} - x_i)^2. \quad (5.10)$$

Here the particles are ordered such that x_i and x_{i+1} are nearest neighbour particle positions and $x_{i+1} > x_i$.

Figure 5.4 shows $\langle N_F(h) \rangle$ and $\langle N_R(r) \rangle$, plotted against h and $h(r)$ respectively, for several values of H and α . In each case we get a good data collapse with

the fixed structure and the radial data converges to $\langle N_F(h_\gamma(\infty)) \rangle$ as explained in Section 5.2.2.

The behaviour in the fixed domain can be analytically computed (see Section 6.3.1 and Section 6.3.2). The solid black lines in Figure 5.4 correspond to exact analytical predictions, where we find that

$$\langle N_F(h) \rangle = L \left[\frac{1}{\sqrt{\pi\sigma^2 h^{2H}}} \sum_{n=-\infty}^{\infty} \left[\exp\left(-\frac{(1-2nL)^2}{4\sigma^2 h^{2H}}\right) - \exp\left(-\frac{L^2 n^2}{\sigma^2 h^{2H}}\right) \right] + \frac{\vartheta_3\left(0, e^{-\frac{L^2}{\sigma^2 h^{2H}}}\right)}{\sqrt{\pi\sigma^2 h^{2H}}} \right], \quad (5.11)$$

and $\vartheta_3(\cdot, \cdot)$ is the elliptic theta function of third kind (see Appendix A for the full expression). Using (5.11) the limiting value $\langle N_R(\infty) \rangle$ can be computed exactly, where by using (5.6) we have

$$\langle N_R(\infty) \rangle = 2\pi r_0 \left[\frac{(1-H)^{2H}}{\sqrt{\pi\sigma^2 (r_0 H)^{2H}}} \sum_{n=-\infty}^{\infty} \left[\exp\left(- (1-H)^{2H} \frac{(1-4n\pi r_0)^2}{4\sigma^2 (r_0 H)^{2H}}\right) - \exp\left(- (1-H)^{2H} \frac{(2\pi r_0 n)^2}{\sigma^2 (r_0 H)^{2H}}\right) \right] + \frac{(1-H)^{2H} \vartheta_3\left(0, e^{-\frac{(2\pi r_0)^2 (1-H)^{2H}}{\sigma^2 (r_0 H)^{2H}}}\right)}{\sqrt{\pi\sigma^2 (r_0 H)^{2H}}} \right], \quad (5.12)$$

the values of σ^2 are dependent on the implementation of the simulation and numerically we extract $\sigma^2 \approx 2.3, 1$ and 0.5 for $H = 1/3, 1/2$ and $2/3$, respectively.

The dashed black line in Figure 5.4 corresponds to a power law behaviour occurring in a scaling window of intermediate h . Where for the Lévy case

$$\langle N_F(h) \rangle = L/(\pi\sigma_\alpha h^{2/\alpha})^{1/2}, \quad (5.13)$$

Using (5.13) and (5.6) the corresponding asymptotic behaviour for the radial structure is

$$\langle N_R(r) \rangle \rightarrow \begin{cases} 2\sigma_\alpha^{-1} \pi^{1/2} \left(\frac{r_0^{1-\alpha}}{\alpha-1}\right)^{-1/\alpha}, & \alpha > 1 \\ 1, & \alpha \leq 1 \end{cases} \quad \text{as } r \rightarrow \infty \quad (5.14)$$

and this limit is indicated for the $\alpha = 3/2$ data by the red dashed lines. The values for σ_α have been extracted numerically from the data and are approximately $\sigma_\alpha \approx 1.4, 4$ and 10.8 for $\alpha = 1, 3/2$, and $5/2$, respectively.

Figure 5.5 shows the behaviour of $\langle D^2 \rangle$ for (a) fBm data and (b) Lévy data. In each case $\langle D_F^2 \rangle$ and the analogous $\langle D_R^2 \rangle$ are increasing functions, and in the fixed domain $\langle D_F^2(h) \rangle$ will converge to L^2 . In the radial domain, since $\langle N_R(r) \rangle$ converges

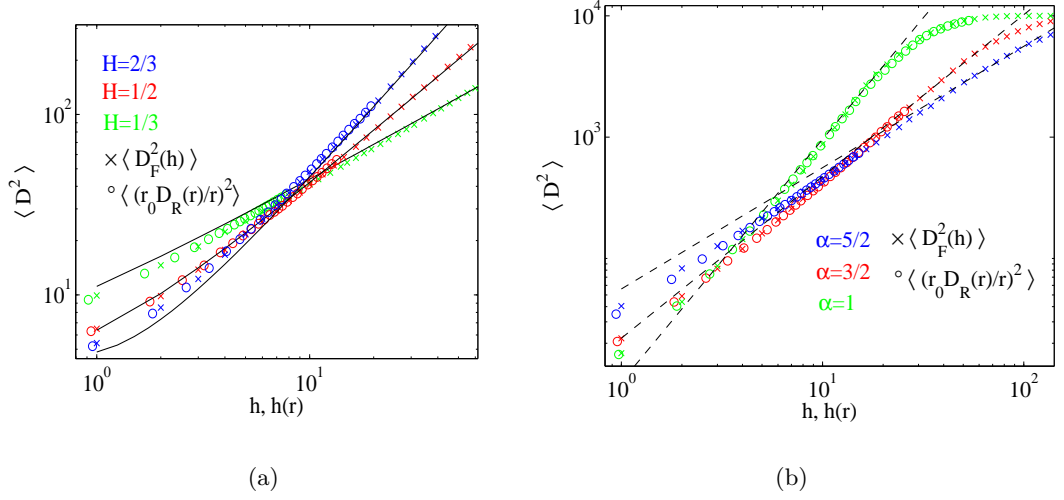


Figure 5.5: Numerical confirmation of the mapping (5.4) between radial geometry (o) and fixed domain (x) for $\langle D^2 \rangle$: (a) Particles perform fBm with $\gamma = H$. (b) Particles are an α -stable Lévy process with $\gamma = \max\{1/\alpha, 1/2\}$. For each radial process, plotting $\langle (r_0 D_R(r)/r)^2 \rangle$ vs $h(r)$ gives a data collapse. Data is gathered for $L = 100$ with $r_0 = L/2\pi$ and 100 initial particles. Solid lines indicate an exact prediction (see Section (6.3.1)) and dashed lines indicate the long time power law behaviour of the density (see Section (6.3.2)).

to a fixed value, we have $\langle D_R^2(r) \rangle \sim (2\pi r / \langle N_R(r) \rangle)^2 \rightarrow \infty$ as $r \rightarrow \infty$. We use the rescaled behaviour $\langle (r_0 D_R(r)/r)^2 \rangle$, where by plotting against $h(r)$ we attain a good data collapse. The full black lines indicate the exact prediction and the dashed black lines indicate the power law behaviour, which are also derived in Section 6.3.1 and Section 6.3.2, respectively.

5.4 Generalized geometries

In the previous section we have shown how behaviour in radially growing structures can be mapped to behaviour in structures growing on a fixed domain. In this section we generalize our theory by considering structures that evolve on a general isotropic domain $[0, L(t))$ in one dimension with periodic boundary conditions.

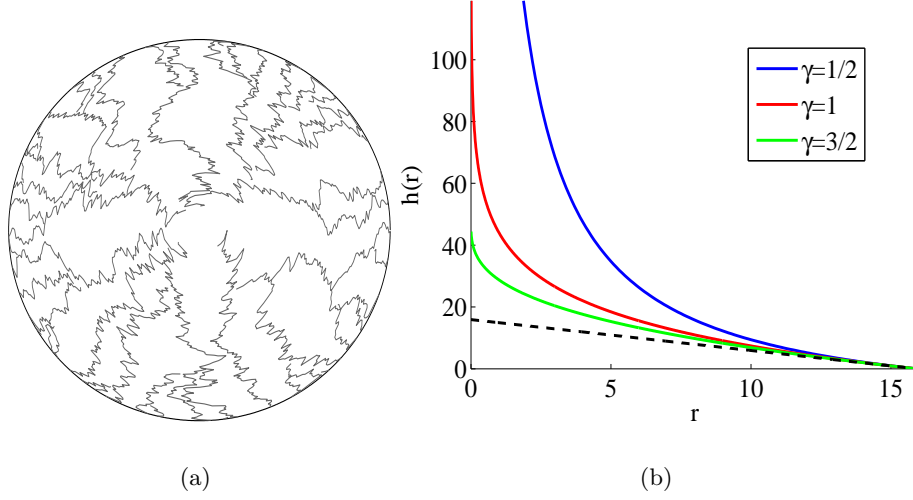


Figure 5.6: (a) Radially decreasing coalescing Brownian structure with $r_0 \approx 15.9155$, each particle performs a directed path inwards. (b) The inward mapping (5.15) for $r_0 \approx 15.9155$ and several values of γ . Analogous to the outward mapping (5.4) the initial behaviour is linear where $h(r) \simeq r_0 - r$ (black dashed line). The asymptotic behaviour depends on γ , where for $\gamma > 1$ the mapping has a finite limit. Despite this finite value all inward radial structures will fixate.

5.4.1 Decreasing radial domain

We start by considering decreasing radial structures where the length of the domain decreases uniformly as a function of the radius. This particular geometry has received attention in [126] for competition interfaces in an inward growing Eden growth model. Figure 5.6(a) shows an illustration of such a coalescing structure, where particles diffuse with $\gamma = 1/2$ on a decreasing radial domain. We easily adapt the mapping $h(r)$ to take into account the decreasing radius, where (5.4) becomes

$$h(r) = \int_r^{r_0} \left(\frac{r_0}{s}\right)^{1/\gamma} ds = \begin{cases} \frac{\gamma r_0}{1-\gamma} \left[\left(\frac{r_0}{r}\right)^{\frac{1-\gamma}{\gamma}} - 1 \right], & \gamma \neq 1 \\ r_0 \log\left(\frac{r_0}{r}\right), & \gamma = 1 \end{cases}, \quad (5.15)$$

where r_0 is the initial radius. The function (5.15) is shown in Figure 5.6(b), the initial behaviour is $h(r) \simeq r_0 - r$ and as $r \rightarrow 0$ the limit depends on γ .

Comparing the mapping for inward growing structures (5.15) to outward growing structures (5.4) we see that (5.15) has a finite limit for $\gamma > 1$, whilst the limit is infinite in (5.4), and this is the opposite for $\gamma < 1$. Although for $\gamma > 1$ (5.15)

has a finite limit

$$h_\gamma(\infty) = \frac{\gamma}{\gamma-1} r_0,$$

the analogous structure on the fixed domain will typically have already fixated at $h_\gamma(\infty)$. Since for $\gamma > 1$ the fixation time τ scales as

$$\tau \sim L^{1/\gamma} \ll L \sim r_0 \sim h_\gamma(\infty),$$

so the inward growing structure fixates as well. The special case of $\gamma = 1$ corresponds to a mirror point, where the limit $h_\gamma(\infty) = \infty$ in (5.4) and (5.15) stays the same.

In Figure 5.7(a) and (b) we illustrate the use of (5.15) for particles that perform fBm with $\gamma = H$. Due to the decreasing size of the domain, $\langle N_R(r) \rangle \rightarrow 1$ as $r \rightarrow 0$. By plotting $\langle N_R(r) \rangle$ vs $h(r)$ and $\langle (r_0 D(r)/r)^2 \rangle$ vs $h(r)$ we obtain a data collapse with the fixed model. Similar behaviour is seen in Figure 5.7(c) which shows $\langle N \rangle$ for Lévy structures. The mapping (5.15) with $\gamma = \max\{1/\alpha, 1/2\}$ works well and plotting $\langle N_R(r) \rangle$ vs $h(r)$ gives a data collapse.

5.4.2 Motion on a general evolving domain

Consider as before $X := (X_h, h \geq 0)$ an arm in the fixed domain, the displacement of this process lies in domain $[0, L(0))$ for all $h \geq 0$. Take $Y := (Y_t, t \geq 0)$ to be an arm in a homogeneous, time dependent domain, taking values in $[0, L(t))$ for all $t \geq 0$, where $L(t)$ is a general continuous function such that $L(t) > 0$ for all $t \geq 0$. Note that the radially increasing/decreasing domain is given by $L(t) = 2\pi r(t)$ with $r = r_0 \pm t$. We assume as before that the local scale invariance property (5.2) holds. The coordinate transformation (5.3) then generalizes to

$$x = \frac{L(0)}{L(t)} y, \tag{5.16}$$

leading to

$$\frac{dh}{dt} = \left(\frac{dx}{dy} \right)^{1/\gamma} = \left(\frac{L(0)}{L(t)} \right)^{1/\gamma}.$$

Therefore

$$h(t) = \int_0^t \left(\frac{L(0)}{L(s)} \right)^{1/\gamma} ds. \tag{5.17}$$

Analogous to (5.4), for t close to 0 we have $h(t) \simeq t$ and if $L(t) \gg t^\delta$ for some $\delta > \gamma$, then we have

$$\lim_{t \rightarrow \infty} h(t) < \infty.$$

Thus provided (5.17) exists, we can always map structures that reside on arbitrary homogeneous domains of size $L(t)$ to structures evolving on a fixed domain. We

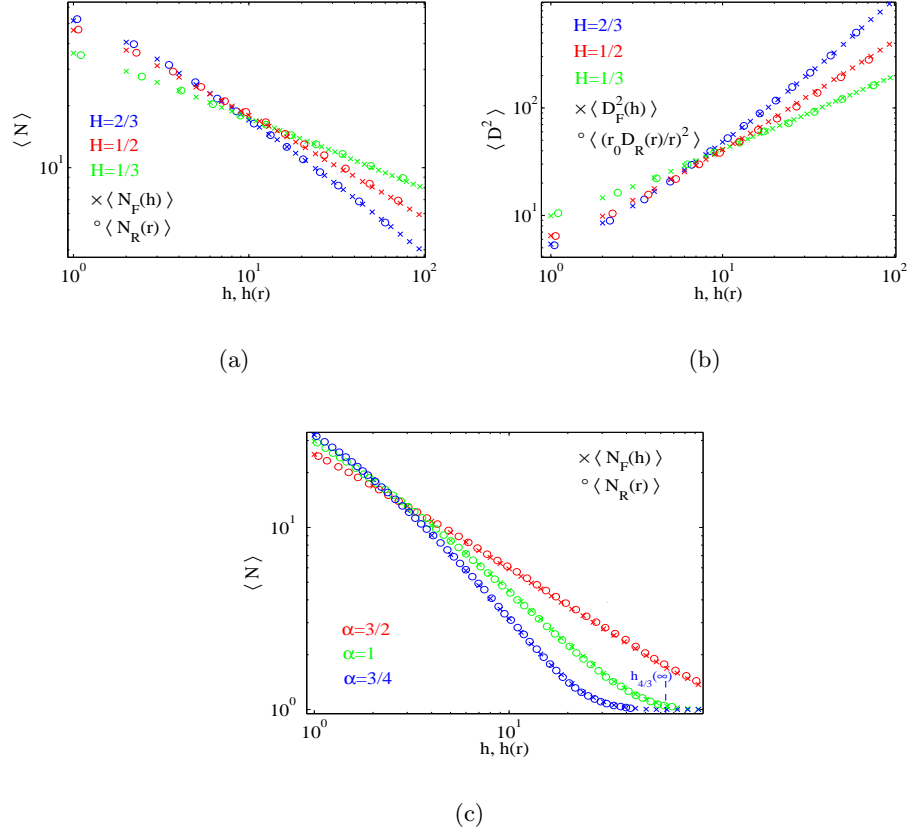


Figure 5.7: Numerical confirmation of the mapping between fixed (\times) and decreasing radial (\circ) structures. Here we take $L = 100$ and $r_0 = L/2\pi$ and an initial 100 arms. We use the mapping (5.15) with $\gamma = H$ for fBm data (a), (b) and $\gamma = \max\{1/\alpha, 1/2\}$ for Lévy data (c).

provide a rigorous derivation of (5.17) for fBm and α -stable Lévy structures in Section 6.2.

As an example, we use (5.17) to look at the behaviour of a structure evolving in an exponentially increasing domain

$$L(t) = L(0) \exp(t/c) \quad (5.18)$$

where $c > 0$. This is equivalent to studying random walks with an exponentially decreasing jump size which has received a considerable amount of interest, see [42, 104, 114, 166, 167, 182]. These processes have a variety of practical applications including simulated annealing and the modelling of the displacement of quantum

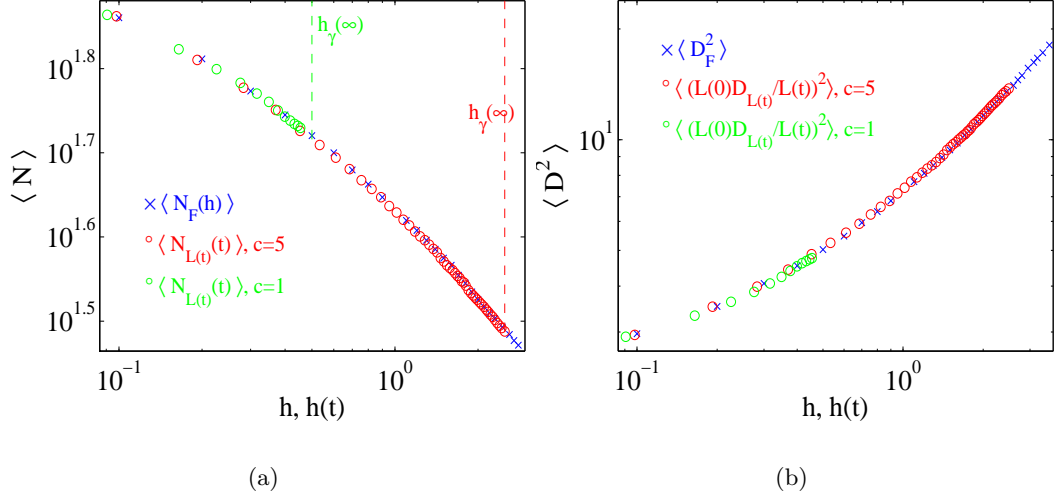


Figure 5.8: Illustrating the use of (5.17) for coalescing Brownian motion ($\gamma = 1/2$), here we map the behaviour of a growing isotropic structure (\circ) to the analogous behaviour in the fixed structure (\times). We choose $L(t) = 100 \exp(t/c)$, with $c = 1$ and $c = 5$, and initially 100 particles. By plotting (a) $\langle N_{L(t)}(t) \rangle$ and (b) $\langle (L(0)D_{L(t)}(t)/L(t))^2 \rangle$ against $h(t)$ we obtain a data collapse. In (a) the color vertical dashed lines correspond to the limit $h_\gamma(\infty) = c\gamma$.

particles [25]. For this $L(t)$ using (5.17) we have

$$h(t) = c\gamma \left(1 - \exp\left(-\frac{t}{c\gamma}\right) \right), \quad (5.19)$$

and subsequently $h(t)$ has the limit

$$h_\gamma(\infty) = \lim_{t \rightarrow \infty} h(t) = c\gamma.$$

Note that by the choice of $L(t)$ this limit does not depend on $L(0)$. In Figure 5.8 we illustrate the use of the mapping (5.19) for coalescing Brownian structures with $\gamma = 1/2$. As in previous examples, the behaviour is mapped to the fixed domain by plotting $\langle N_{L(t)}(t) \rangle$ and $\langle (L(0)D_{L(t)}(t)/L(t))^2 \rangle$ against $h(t)$.

5.5 Generalized local interactions

In this section we extend our theory to consider systems with non-local interactions. These will be coagulating structures where particles either have a non-zero size $d > 0$ or structures with particles that coagulate and branch. We illustrate the

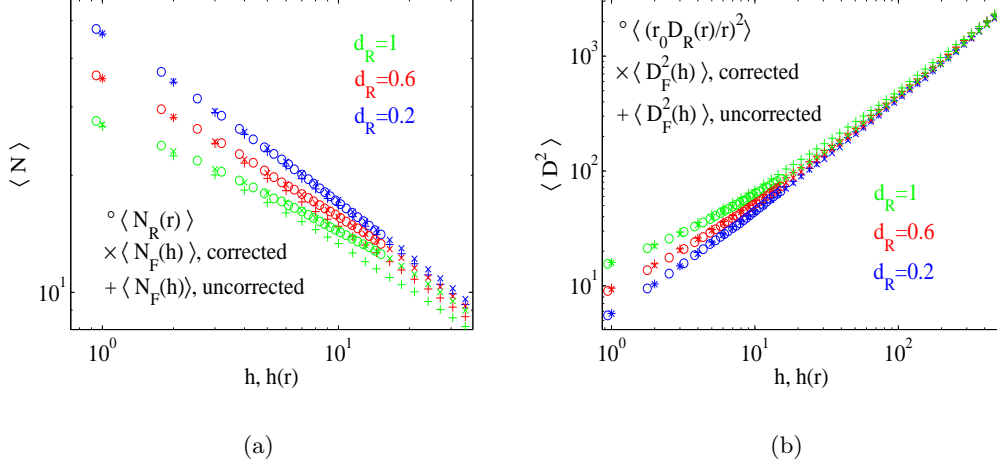


Figure 5.9: Mapping the radially increasing structure to the fixed structure for a system with non-local interactions. Here particles perform Brownian motion. In the radial (fixed) case particles have a size d_R (d_F) and they coalesce when the distance between their centers is less than d_R (d_F). We use (5.4) with $\gamma = 1/2$, initially we have 100 particles and $r_0 = L/(2\pi)$ with $L = 100$. By plotting against $h(r)$ we map (a) $\langle N_R(r) \rangle$ and (b) $\langle (r_0 D_R(r)/r)^2 \rangle$ and obtain a good data collapse. In each case the relationship (5.20) is used to obtain an exact mapping (shown by corrected label), compared to an approximate mapping (shown by uncorrected label) when (5.20) is not used i.e. $d_F \equiv d_R$.

mapping (5.4) for radially increasing structures and fixed domain structures, which are composed of particles that perform Brownian motion with $\gamma = 1/2$.

5.5.1 Finite size particles

In most real world systems particles have a non-zero size, which influences the interactions between particles and the formation of structures containing these particles [110]. Here we look at coalescing particle systems, where each particle has an isotropic shape with a diameter $d > 0$. Introducing such a length scale in the interactions means that particles will now coagulate when the distance between their centers is less than d . As long as this is much smaller than the system size i.e. $d \ll L$, the corrections introduced are small (see Figure 5.9). We can include these corrections into the mapping by preserving the particle size in each domain relative

to the system size. Taking d_R as the fixed diameter in the radial geometry, we have

$$d_F(h) = \frac{r_0}{r(h)} d_R, \quad (5.20)$$

where $d_F(h)$ is the rescaled diameter in fixed geometry such that

$$d_F(0) = d_R \quad \text{and} \quad d_F \rightarrow 0 \quad \text{as} \quad h \rightarrow h_\gamma(\infty).$$

The function $r(h)$ in (5.20) is the inverse of (5.4) and for general $\gamma \neq 1$ it has the form

$$r(h) = \frac{\gamma^{\gamma/(1-\gamma)} r_0^{1/(1-\gamma)}}{\left(\gamma r_0 - (1-\gamma)h\right)^{\gamma/(1-\gamma)}}, \quad (5.21)$$

diverging if $h \rightarrow h_\gamma(\infty)$.

In Figure 5.9(a) and (b) we look at such systems for a range of d_R values. By using the mapping (5.4) with $\gamma = 1/2$ we are able to map the radially growing structure to the fixed structure. As before this illustration is shown for the behaviour of $\langle N_R(r) \rangle$ and $\langle (r_0 D_R(r)/r)^2 \rangle$, where we plot against $h(r)$ to obtain a data collapse. Note here for the fixed structure simulations we include the data where the correction (5.20) is applied (\times) and where it is ignored ($+$) i.e. we choose $d_F \equiv d_R$. We can see that the inclusion of (5.20) provides an exact mapping between the behaviours in the two domains and that these corrections are small if d_R is small. The introduction of particle size only has affect on the initial behaviour, where initially the distance between particles is small and due to $d_R > 0$, more coalescing events take place. As time increases, the distance between particles increase and the behaviour becomes largely independent of d_R .

5.5.2 Structures in $n + 1$ dimensions

It is interesting to note that mapping Eq. (5.17) does not depend on the dimensions n of the state space. It holds for an $n + 1$ dimensional isotropic growing structure, where in each spatial direction- i the displacement $Y_i \in [0, L(t)]$, where $L(t) > 0$ for all $t \geq 0$. We can still characterize the behaviour of this $n + 1$ dimensional evolving structure by mapping it to a fixed structure, where in each spatial direction- i the displacement X_i is in the fixed domain $[0, L(0)]$. In order to do this, we require the local scale invariance property (5.2) to hold in all spatial directions $i = 1, \dots, n$

$$dX_i \sim (dh)^\gamma \quad \text{and} \quad dY_i \sim (dt)^\gamma. \quad (5.22)$$

In this case the mapping (5.17) stays exactly the same. It is also possible to include anisotropy in (5.22) where there can be a possible i -dependence of the multiplicative

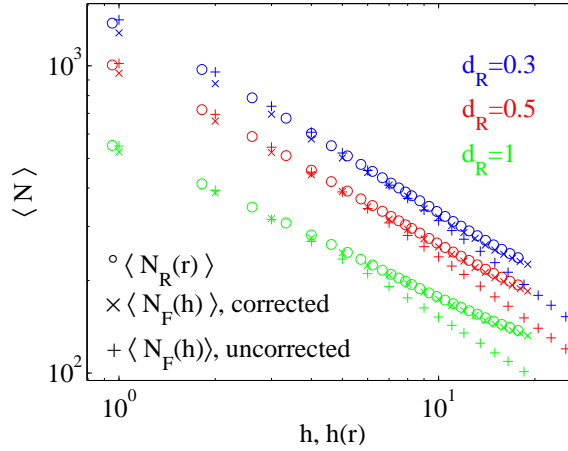


Figure 5.10: Illustrating the use of (5.4) by mapping the radially increasing structure to the fixed structure for a 2 + 1-dimensional system with $r_0 = 20$ and particle diameter d_R (d_F) for radial (fixed) structure. We take the initial density to be 1 where the number of particles is approximately $4\pi r_0^2$, which is equal to the surface area. By plotting against $h(r)$ we map $\langle N_R(r) \rangle$ exactly when (5.20) is used (shown by corrected label), compared to an approximate mapping (shown by uncorrected label) when (5.20) is not used i.e. $d_F \equiv d_R$.

factors but γ should be identical in all directions. In Figure 5.10 we show that such a characterization works well in $n = 2$ dimension, where using (5.4) we map the data of $\langle N \rangle$ from a growing sphere $S^2(r)$ to a fixed sphere $S^2(r_0)$. As above, particles have a given size $d > 0$ and we use the correction (5.20) on the fixed structure as indicated by (\times) to obtain an exact match as oppose to an approximate match indicated by (+) when (5.20) is not used i.e. $d_F \equiv d_R$.

5.5.3 Branching coalescing structures

A similar treatment is possible for more general interactions with intrinsic length scales. Here we treat coagulating and branching structures. These structures have much interest due to the wide variety of applications in natural and physical processes, some examples include the modelling of surnames in genealogy [163], or the propagation of neutrons in a nuclear reactor [162]. The use of branching processes appears quite naturally in the discipline of biology where it can be used to explain populations of biological cells, genes or biomolecules [103]. In this section we study spatial models of particle branching, this specific type of model has applications in areas such as microbiology and epidemiology [88, 149]. We generalize the diffus-

ing coalescing model studied in Section 5.2 by adding the mechanism of particle branching to the system. In order to connect the growing radial domain to the fixed domain, we define a relationship between the branching rate R_F in fixed domain and R_R in the growing radial domain such that the number of birth events in each domain are equal. Let $N_R(\Delta r)$ be the number of births in the radial domain in the interval $[r, r + \Delta r]$ and let $N_F(\Delta h)$ denote the number of births in the fixed domain in the interval $[h, h + \Delta h]$. Then $R_F = N_F(\Delta h)/\Delta h$ and $R_R = N_R(\Delta r)/\Delta r$, by using (5.4) and assuming $N_F(\Delta h) = N_R(\Delta r)$, we have

$$\frac{R_R}{R_F} = \frac{N_R(\Delta r)/\Delta r}{N_F(\Delta h)/\Delta h} = \frac{\Delta h}{\Delta r} = \frac{r_0^2}{r^2}.$$

In order to map the behaviour in the radial domain to the fixed domain with fixed rate R_F we use the relationship

$$R_R(r) = \left(\frac{r_0}{r}\right)^2 R_F. \quad (5.23)$$

For the inverse, where we map behaviour from the fixed domain to the radially increasing domain with fixed rate R_R we use

$$R_F(h) = \left(\frac{r(h)}{r_0}\right)^2 R_R, \quad (5.24)$$

where $r(h)$ is given in (5.21) with $\gamma = 1/2$.

We consider two types of models where particles branch. In each case the particles perform Brownian motion and coalesce upon contact and they branch after a random time exponentially distributed with mean $1/R$ where $R > 0$ is the branching rate. In one model, which we call “uniform”, the new particle is placed uniformly in the domain. In the second model which we call “local” the new particle is placed in a local neighbourhood around its mother. For the local model, in order for the particles to not coalesce instantaneously, the mother and child move independently for a simulation time $1/R$.

In Figure 5.11 we map the radially growing structure to the fixed domain structure for the two branching models. Using (5.4) and the relationship (5.23) we plot $\langle N_R(r) \rangle$ against $h(r)$ to attain a data collapse. In both cases, we show that our theory can be extended to include the non-local interaction of branching. The black solid (dashed) curves shown in Figure 5.11(a) (Figure 5.11(b)) are a prediction for $\langle N_F(h) \rangle = L\rho(h)$ (see Eq. (5.27) below).

For the uniform branching model we can adapt previous results on the rate equation found in [4, 126, 135, 18] to characterize the behaviour of the density $\rho_F(h)$.

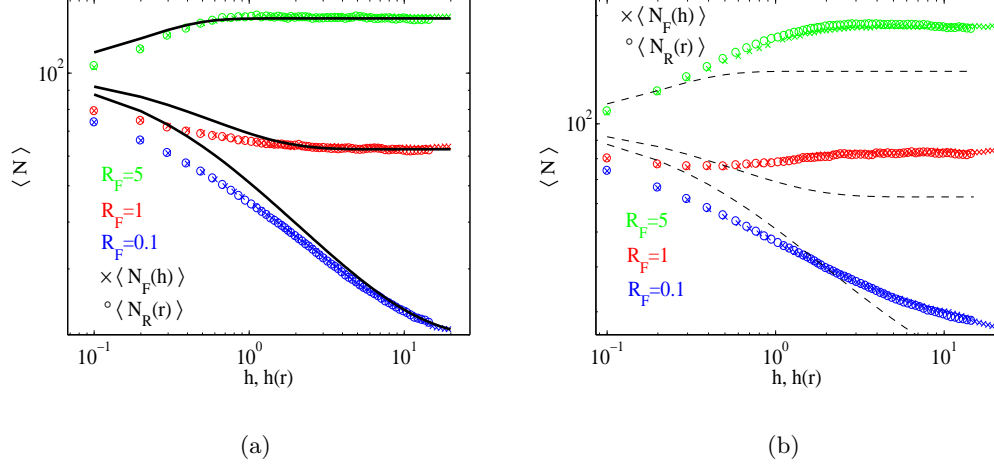


Figure 5.11: Mapping the behaviour of $\langle N \rangle$ from the growing radial structure to the fixed domain for the branching models (a) uniform and (b) local. We use (5.4) with the relationship (5.23), simulations performed for system with 100 initial particles, $L = 100$ and $r_0 = L/(2\pi)$. We use several values for R_F and in each case plot $\langle N_R(r) \rangle$ against $h(r)$ to obtain a data collapse. In (a) the solid black curves are the analytical prediction (5.27). To illustrate the difference between the branching mechanisms this is also shown in (b) as dashed black curves.

For just coalescing Brownian structures, the rate equation governs the large height behaviour of the density $\rho(h)$ in the fixed domain and reads

$$\frac{d\rho}{dh} = -\frac{\pi\rho^3}{2}, \quad (5.25)$$

with solution $\rho(h) \sim h^{-1/2}$. Eq. (5.25) governs the long time behaviour of diffusion-limited systems which undergo a coagulation process in one spatial dimension. The term on the right hand side is a reaction term which accounts for the diffusive elements of the stochastic walkers, it assumes generic spatial initial conditions such as particles placed uniformly in an interval [18]. The form of Eq. (5.25) will be discussed further in Section 6.3.2.

Using Eq. (5.25), we consider a density dependent input which has no spatial dependency and thus the particles appear homogeneously in space. This reflects the branching reaction in the uniform branching model [18, 135], and leads to an additive term in the rate equation such that

$$\frac{d\rho}{dh} = -k_1\rho^3 + k_2\rho, \quad (5.26)$$

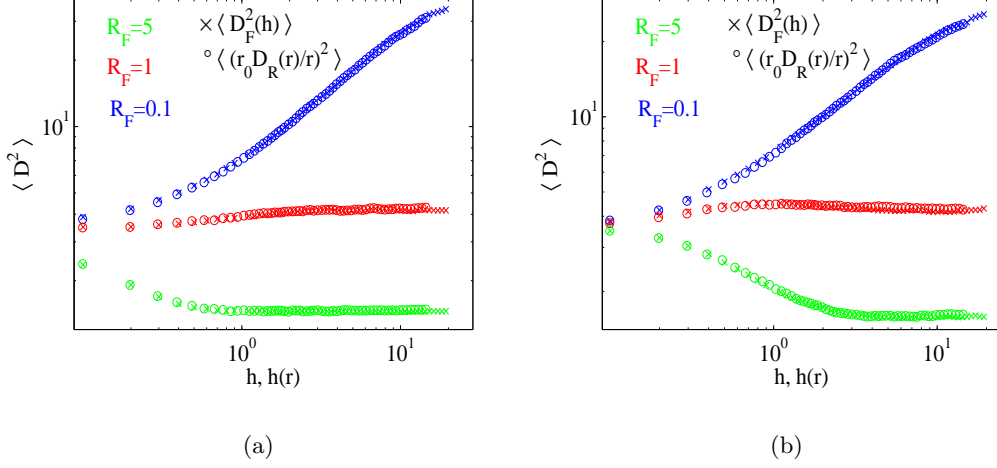


Figure 5.12: Mapping the behaviour of $\langle D^2 \rangle$ from the growing radial structure to the fixed domain for the branching models (a) uniform and (b) local. We use (5.4) with the relationship (5.23), simulations are performed with $r_0 = L/(2\pi)$ and $L = 100$ with 100 initial particles. We use several values for R_F and in each case plot $\langle (r_0 D_R(r)/r)^2 \rangle$ against $h(r)$ to obtain a data collapse.

where $k_1 = \pi/2$ and k_2 is a model dependent constant proportional to R_F . We find $k_2 \approx 0.6158R_F$, where the value 0.6158 was fitted to the data. Solving (5.26) gives

$$\rho(h)/\rho(0) = \begin{cases} \left[\frac{k_2}{k_1} \left(1 - \frac{1}{k_1 \exp(2k_2(h+c_1))+1} \right) \right]^{1/2}, & k_1 < k_2 \\ \left[\frac{k_2}{k_1} \left(1 + \frac{1}{k_1 \exp(2k_2(h+c_2))-1} \right) \right]^{1/2}, & k_2 < k_1 \end{cases} \quad (5.27)$$

where $c_1 = -\text{Log}[k_2 - k_1]/2k_2$ and $c_2 = -\text{Log}[k_1 - k_2]/2k_2$. If $k_1 = k_2$ in (5.27) then $\rho(h) = \rho(0)$ for all $h \geq 0$.

In Figure (5.12) we also illustrate the mapping (5.4) for the data $\langle D^2 \rangle$. Unlike in the purely coalescing case, here $\langle D_F^2(h) \rangle$ reaches a stationary number which depends on R_F . This stationary state occurs due to a balance between the coalescing and branching events. We use the relationship (5.23) and plot $\langle (r_0 D_R(r)/r)^2 \rangle$ against $h(r)$ to obtain a data collapse.

We illustrate the inverse mapping (5.21) with $\gamma = 1/2$ in Figure 5.13 for the system density $\langle \rho \rangle$. Here in order to map the density from the fixed domain to the growing radial domain along with (5.21), we also use the relationship (5.24) in simulating the fixed structure and we plot $\langle N_F(h)/(2\pi r(h)) \rangle$ vs $r(h)$ to obtain a data collapse. The data shows that $\langle N_R(r) \rangle$ is linear for large r and this dependence

is computed analytically below, see (5.31). In (a) the full black line and in (b) the dashed black line correspond to the expression (5.29) which is an analytical prediction for the density $\rho(r)$ for the uniform model.

In order to obtain an analytical expression for the growing radial domain, we modify the density equation (5.26) by using the relation (5.24) between the rates R_F and R_R , this leads to

$$\frac{d\rho}{dh} = -k_1\rho^3 + k_2\left(\frac{r_0}{r_0 - h}\right)^2 \rho, \quad (5.28)$$

where now $k_2 \approx 0.6158R_R$. Using (5.4), the solution to (5.28) can be expressed as

$$\rho(r) = \frac{e^{k_2 r} r_0}{r} \left[e^{2k_2 r_0} + 2k_1 \left[-e^{2k_2 r_0} r_0^2 / t + 2k_2 r_0^2 \Phi(2k_2 t) \right]_{r_0}^r \right]^{-1/2}, \quad (5.29)$$

where $\Phi(x) = \int^x e^t / t dt$. For large r (5.29) can be expressed as

$$\rho(r) \approx \frac{1}{r} \left[2k_1 \left(-\frac{1}{r} + 2k_2 e^{-2k_2 r} \Phi(2k_2 r) \right) \right]^{-1/2}, \quad (5.30)$$

and for $r \rightarrow \infty$

$$e^{-2k_2 r} \Phi(2k_2 r) \approx \frac{1}{2k_2 r} + \frac{1}{(2k_2 r)^2} + O(1/r^3).$$

Combining this with (5.30) gives

$$\lim_{r \rightarrow \infty} \rho(r) = \left(\frac{k_2}{k_1} \right)^{1/2}, \quad (5.31)$$

this limit is indicated on the right panel in Figure 5.13(a).

In Figure 5.14 we also illustrate the inverse mapping (5.21) with the relationship (5.24) to map $\langle D^2 \rangle$ from the fixed domain to the radially increasing domain for the two branching models. By plotting $\langle (r(h)D_F(h)/r_0)^2 \rangle$ vs $r(h)$ we obtain a good data collapse with $\langle D_R^2(r) \rangle$. We have already noted that $\langle D_R^2(r) \rangle \sim (2\pi r / \langle N_R(r) \rangle)^2$ and by (5.31) we have $\langle N_R(r) \rangle \sim r$ for r large, therefore $\langle D_R^2(r) \rangle$ converges to a constant which is dependent on R_R .

5.6 Discussion

In this chapter we have studied the behaviour of two and three dimensional growth structures which are scale invariant systems composed of interacting particles. Particular applications of our results include systems with diffusion-limited reactions.

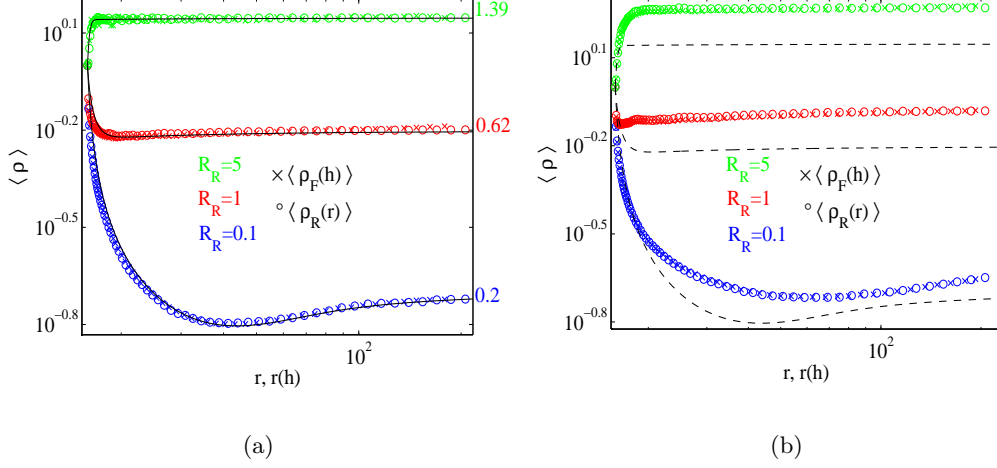


Figure 5.13: Mapping the behaviour of $\langle \rho \rangle$ from the fixed domain to the growing radial domain for the branching models (a) uniform and (b) local. We use the inverse mapping (5.21) with the relationship (5.24), simulations performed with $L = 100$ and $r_0 = L/(2\pi)$ with 100 initial particles. The mapping is illustrated for several values of R_R and in each case we plot $\langle N_F(h) \rangle / (2\pi r(h))$ vs $r(h)$ to get a data collapse. The solid black curves in (a) are the analytical prediction (5.29) with limits (5.31) indicated on the right panel, these curves (black dashed) are also shown in (b) for comparison.

These reactions are seen to occur in a variety of physical processes such as ionic recombination [147], electron-hole recombination [186], atmospheric dust [41], colloids [129], micellar systems [54] and polymers in solution [96]. In order to describe how such systems depend on the embedding geometry we derived a mapping (5.17). This allows us to map the behaviour from a time-dependent domain to the behaviour in the fixed domain, for which we can make predictions on the analytical form of the statistics [135, 180]. Much of our examples have focused on the growing radial geometry, however, we have also shown how to treat general time-dependent domains $[0, L(t))$. We have proposed that our theory can be extended to general n -dimensional structures and have illustrated this for coalescing Brownian motions moving on a surface of a growing 2 dimensional sphere. It is interesting to note here that the mapping (5.17) does not depend on the spatial dimension.

Although we have restricted our analysis to coalescing systems where particles undergo the reaction $A + A \rightarrow A$, our results also hold for annihilating systems with the reaction $A + A \rightarrow \emptyset$. This case will be considered in Chapter 7 to model

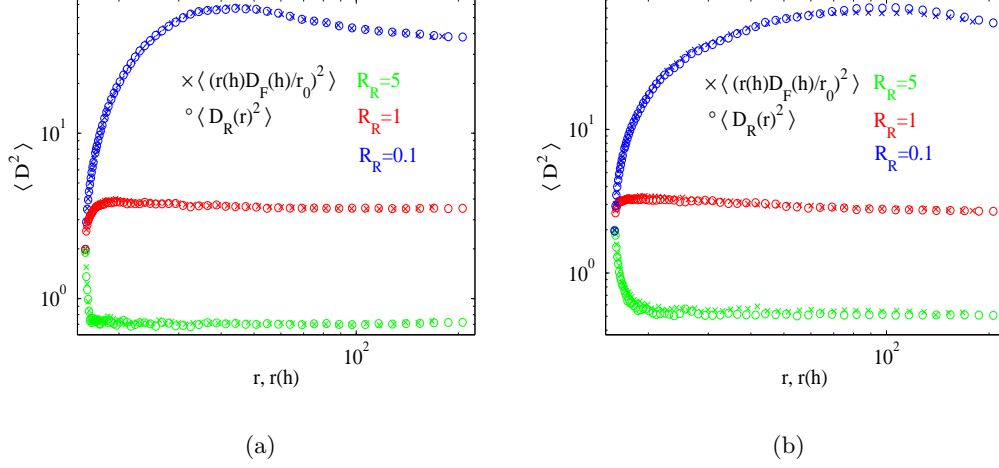


Figure 5.14: Mapping the behaviour of $\langle D^2 \rangle$ from the fixed structure to the growing radial structure for the branching models (a) uniform and (b) local. We use (5.21) with the relationship (5.24), simulations are performed with $r_0 = L/(2\pi)$ and $L = 100$ with 100 initial particles. We use several values for R_R and in each case plot $\langle (r(h)D_F(h)/r_0)^2 \rangle$ against $r(h)$ to obtain a data collapse with $\langle D_R^2(r) \rangle$, this can be seen to converge to a constant as $r \rightarrow \infty$.

systems of domain boundaries for competing microbial colonies. We have also shown how to treat structures with non-local interactions, where we focused on systems with particles that have a non-zero size and branching. A particular application for our branching results is the modelling of competition in bacteria populations with mutation, here the phase boundaries will annihilate and branch.

The only crucial condition for our approach are an isotropic evolution of the general time-dependent domains and local scale invariance which has the same exponents in all spatial directions. In general, one can interpret this as a homogeneous time-dependent metric on a fixed domain. The mapping (5.17) then provides an exact description for the statistics of locally interacting particles on the time-dependent domain and is a result which is quite remarkable.

As we shall show in the next chapter, the mapping can be derived rigorously for Markovian systems such as Brownian motions and α -stable Lévy processes. For non-Markovian systems such as fBm, the noise has long range correlations and we find (5.4) to be not exact but a very good approximation, which already shown in Section 5.3 gives a good data collapse.

Chapter 6

Exact results on scale invariant growth

6.1 Introduction

Particles undergoing stochastic motion are universal in nature. At the core of many systems, microscopic particle dynamics and local neighbourhood interactions tend to define observable global patterns [19, 93, 125]. The most common point motion has to be the Brownian motion, which has been studied extensively (see [61, 156] for a general review). Due to the central limit theorem leading to Gaussian fluctuations, it has profound applications in a wide variety of scientific disciplines. However, in many real world systems which on smaller scales consist of interactions between particles, the path taken by a particle can undergo steps which deviate from the conditions required by the central limit theorem. When such cases occur, the behaviour will no longer be described by Gaussian fluctuations or continuous paths with stationary increments. Indeed, for many systems, local correlations rarely die out but can manifest themselves so that the motion of particles becomes correlated in time, such paths are seen when there exist an inherent memory in the system, as is the case for many non-equilibrium growth and spreading phenomena [126, 177] and for the domain boundary fluctuations which lead to fractional Brownian motion paths (see Chapter 3). Many examples can be seen in nature of paths not being Brownian motion, one such is the trajectories produced by animals foraging for food, in such cases, long flights can occur in their paths which cannot be accounted by local diffusion, however, such behaviour can be modelled using processes such as α -stable Lévy processes [30, 34, 75]. It is thus necessary to have a theory which describes the properties of various systems with a range of motion.

In the previous chapter, we derived a mapping (5.17) using the local scale invariance properties of the trajectories (5.2) and coordinate transformation between the state spaces. The mapping $h(t)$ has been shown to describe the behaviour of directed isotropic structures on the time-dependent domain $[0, L(t))$ in terms of the analogous behaviour of structures on the fixed domain $[0, L(0))$. In particular, the full statistics of the time-dependent structures can be obtained by looking at the fixed structure at height $h(t)$, illustrated by (5.5). This result is particularly interesting since the fixed domain has been studied extensively and there exists a number of exact results, for more details see [4, 126, 135, 148, 180]. The mapping is based on a heuristic derivation and has been verified numerically for inward/outward radial structures and for the example where $L(t) = L(0) \exp(t/c)$.

In this chapter, we present a mathematically rigorous derivation of the mapping (5.17) using standard stochastic calculus for structures with arms distributed according to the self-similar processes: Brownian motion, α -stable Lévy process and fractional Brownian motion (fBm). The Markovian systems (Brownian motion and α -stable Lévy process) have independent increments and are therefore ‘uniquely’ determined by their local scale invariance property. Thus the derivation of the mapping leads to the same form as in (5.17). For the non-Markovian fBm, however, correlations lead to a correction which we compute explicitly. Further we use the Chapman-Kolmogorov equation to compute analytical expressions for the average number of particle $\langle N \rangle$ and the average inter-particle distance squared $\langle D^2 \rangle$ for the fixed domain system. These have already been shown to have a good agreement with the data, as shown in Figure 5.4 and Figure 5.5 (black solid lines and dashed lines).

6.2 Rigorous derivation of the mapping

In this section we derive the mapping $h(t)$ for the self-similar processes mentioned above.

Definition 6.2.1. *A \mathbb{R} -valued stochastic process $X = (X_t, t \geq 0)$ is **self-similar** if its finite-dimensional distributions satisfies for some $\gamma > 0$ the following property*

$$\mathbb{P}(X_{bt_0} \leq x_0, \dots, X_{bt_n} \leq x_n) = \mathbb{P}(b^\gamma X_{t_0} \leq x_0, \dots, b^\gamma X_{t_n} \leq x_n) \quad (6.1)$$

for all $t_0 > 0, \dots, t_n > 0$, x_0, \dots, x_n in \mathbb{R} and $b > 0$ [21].

As before in each structure we consider the directed arms to be described by stochastic processes. Let

$$Y := (Y_t, t \geq 0)$$

be the displacement of a particle on a time-dependent domain $[0, L(t))$ and

$$X := (X_h, h \geq 0)$$

be the displacement of a particle on the fixed domain $[0, L(0))$. We take $L(t) > 0$ for $t \geq 0$ to be a continuous-differential function such that

$$L \in C^1([0, \infty), (0, \infty)).$$

In Langevin form we have the stochastic differential equations (SDE's)

$$dX_h = d\xi_h \tag{6.2}$$

and

$$dY_t = Y_t dt \frac{\dot{L}(t)}{L(t)} + d\xi_t, \tag{6.3}$$

where the first term in (6.3) corresponds to the stretching of space and the second to the inherent fluctuations of the process. The term $d\xi$ represents the noise of the process given by a self-similar process as shown below.

Define a rescaled process $Z := (Z_t, t \geq 0)$, via

$$Z_t = \frac{L(0)}{L(t)} Y_t. \tag{6.4}$$

By using **Itô formula** (see Section B.4 and [156] page 44) the process Z_t satisfies

$$dZ_t = -\frac{L(0)\dot{L}(t)}{L(t)^2} dt Y_t + \frac{L(0)}{L(t)} dY_t,$$

and substituting (6.3) leads to the stochastic differential equation

$$dZ_t = \frac{L(0)}{L(t)} d\xi_t. \tag{6.5}$$

The stochastic process Z evolves on the same fixed domain as X and we will show that under a suitable time change $h(t)$ both processes are equivalent i.e. have the same distribution on the path space

$$(Z_t, t \geq 0) \stackrel{\text{dist.}}{=} (X_{h(t)}, t \geq 0).$$

6.2.1 Brownian motion

Definition 6.2.2. A stochastic process $B := (B_t, t \geq 0)$ on \mathbb{R} is a standard Brownian motion if B_t is a continuous Gaussian process with $B_0 = 0$, $\langle B_t \rangle = 0$ and covariance $\langle B_t B_s \rangle = \min\{t, s\}$ for all $t, s \geq 0$.

In particular this implies $B_t \sim N(0, t)$ which has a probability density function (pdf)

$$p(x, t) = \frac{1}{\sqrt{2\pi t}} \exp\left(-\frac{x^2}{2t}\right), \quad (6.6)$$

for all $t > 0$. It is well known that a Brownian motion satisfies the self-similar property (6.1) with $\gamma = 1/2$. This can be seen through: $\langle B_{bt}^2 \rangle = bt$ which means

$$B_{bt} \sim N(0, bt) \sim b^{1/2} N(0, t) \sim b^{1/2} B_t.$$

To derive the mapping, we take $\xi = B$ in (6.5), and we look at the integral form of (6.5) such that

$$Z_t = \int_0^t \frac{L(0)}{L(s)} dB_s. \quad (6.7)$$

Writing Z_t in the stochastic **Itô integral** form (6.7), as we explain in detail below it is known that such a process is a continuous martingale and Z_t can be written as a time-changed Brownian motion such that $Z_t = B_{h(t)}$.

Definition 6.2.3. *A stochastic process $X = (X_t, t \geq 0)$ is a (continuous time) martingale if it satisfies the following properties:*

- (i) $\mathbb{E}[|X_t|] < \infty$ for all $t \geq 0$.
- (ii) For $t \geq s \geq 0$, $\mathbb{E}[X_t | \mathcal{F}_s] = X_s$, where \mathcal{F}_s is the filtration of the process X and it can be taken to be the σ -algebra generated by the process $(X_u, 0 \leq u \leq s)$ (see Section B.3).

A simple computation shows that Brownian motion is a martingale. Take $t > s$ then

$$\mathbb{E}[B_t | \mathcal{F}_s] = \mathbb{E}[B_t - B_s | \mathcal{F}_s] + \mathbb{E}[B_s | \mathcal{F}_s]$$

and since a Brownian motion has stationary independent increments

$$\mathbb{E}[B_t - B_s | \mathcal{F}_s] = \mathbb{E}[B_{t-s}] = 0,$$

so we have

$$\mathbb{E}[B_t | \mathcal{F}_s] = \mathbb{E}[B_s | \mathcal{F}_s] = B_s.$$

For the rescaled process Z it is known that this is a continuous martingale (see Section B.3 and [106] page 100). We also see this intuitively by using (6.7) and taking

$$\mathbb{E}[Z_t | \mathcal{F}_{s'}] = \mathbb{E}\left[\int_0^t \frac{L(0)}{L(s)} dB_s | \mathcal{F}_{s'}\right]$$

where $t > s'$, this leads to

$$\mathbb{E}[Z_t | \mathcal{F}_{s'}] = \int_0^t \frac{L(0)}{L(s)} \mathbb{E}[dB_s | \mathcal{F}_{s'}]$$

and since

$$\mathbb{E}[dB_s | \mathcal{F}_{s'}] = \begin{cases} 0, & s \geq s' \\ dB_s, & s < s' \end{cases}$$

therefore

$$\mathbb{E}[Z_t | \mathcal{F}_{s'}] = \int_0^{s'} \frac{L(0)}{L(s)} dB_s = Z_{s'}.$$

Since $L(0)/L(s)$ is a continuous function, the rescaled process Z is therefore a continuous martingale.

We summarize our result in the following theorem:

Theorem 6.2.4. *Let $L(0)/L(t) : [0, \infty) \rightarrow (0, \infty)$ be continuous such that for all $t > 0$*

$$h(t) = \int_0^t \left(\frac{L(0)}{L(s)} \right)^2 ds < \infty.$$

Then the stochastic process $Z := (Z_t, t \geq 0)$, given by

$$Z_t = \int_0^t \frac{L(0)}{L(s)} dB_s,$$

is a continuous martingale and a time-changed Brownian motion such that

$$(Z_t, t \geq 0) = (B_{h(t)}, t \geq 0).$$

Proof. We have shown Z to be a continuous martingale and a rigorous proof of Z being a time-change Brownian motion is given in [106] page 204, which follows from Lévy's theorem (B.3.1). The essence of the proof can be summarized in the following heuristics: for all $t \geq 0$ the process Z has the same path space as B , so consider

$$dB_{h(t)} = B_{h(t+dt)} - B_{h(t)} \sim B_{h(t+dt)-h(t)}$$

and since $dh = (L(0)/L(t))^2 dt$ this leads to

$$B_{h(t+dt)-h(t)} \sim B_{(L(0)/L(t))^2 dt} \sim \frac{L(0)}{L(t)} B_{dt}.$$

With $B_{dt} = B_{t+dt} - B_t = dB_t$ therefore

$$B_{h(t+dt)-h(t)} \sim \frac{L(0)}{L(t)} dB_t$$

and when integrated gives Z_t . □

This is a rigorous verification of the mapping (5.17) for Brownian motion with $\gamma = 1/2$.

6.2.2 α -stable Lévy process

Definition 6.2.5. A stochastic process $L^\alpha = (L_t^\alpha, t \geq 0)$, with $\alpha \in (0, 2)$ is an α -stable Lévy process if it has stationary independent increments and a pdf $p_\alpha(x, t)$ whose Fourier transform takes the form

$$\hat{p}_\alpha(k, t) = \exp(-\sigma_\alpha t |k|^\alpha), \quad (6.8)$$

with $\sigma_\alpha > 0$.

α -stable Lévy Processes are Markovian with discontinuous paths and increments with infinite variance, and when $\alpha \in (0, 1)$ their absolute first moment will also be infinite [30, 58, 185]. Another key property is that the fractional moments of L_t^α scale as

$$\langle |L_t^\alpha|^q \rangle^{1/q} \propto t^{1/\alpha}, \quad (6.9)$$

where $0 < q < \alpha$ [30, 75, 144]. The process L^α is self-similar (6.1) with $\gamma = 1/\alpha$, this can be seen using (6.8) and by taking $t \rightarrow bt$

$$\hat{p}_\alpha(k, bt) = \hat{p}_\alpha(b^{1/\alpha} k, t),$$

and this is the Fourier transform of the pdf of $b^{1/\alpha} L_t^\alpha$.

When the arms X (6.2) and Y (6.3) are α -stable Lévy processes we have

$$dX_h = dL_h^\alpha \quad \text{and} \quad dY_t = Y_t dt \frac{\dot{L}(t)}{L(t)} + dL_t^\alpha,$$

through a generalization of **Itô calculus**, [11, 34], the rescaled process Z (6.5) can be expressed in Langevin form as

$$dZ_t = \frac{L(0)}{L(s)} dL_t^\alpha. \quad (6.10)$$

The process Z then is also a time-changed α -stable Lévy process (see [11] page 237) which we show below. By using the property 6.9) on (6.5) we match the q -moment of dX and dZ , leading to

$$(dh)^{q/\alpha} = \left(\frac{L(0)}{L(s)} \right)^q (dt)^{q/\alpha}.$$

Re-arranging gives the mapping (5.17) with $\gamma = 1/\alpha$ such that

$$h(t) = \int_0^t \left(\frac{L(0)}{L(s)} \right)^\alpha ds.$$

To see that the stochastic process $Z = (Z_t, t \geq 0)$ is indeed a time-changed α -stable Lévy process, we use the following approach. The Chapman-Kolmogorov

equation which governs the evolution of the pdf of Z_t can be shown to satisfy (see [34] page 11)

$$\frac{\partial p_\alpha}{\partial t} = \left(\frac{L(0)}{L(t)} \right)^\alpha \frac{\partial^\alpha p_\alpha}{\partial |z|^\alpha}, \quad (6.11)$$

where the operator $\frac{\partial^\alpha}{\partial |z|^\alpha}$ is a fractional-derivative and can be defined in Fourier space as

$$F \left[\frac{\partial^\alpha f(z)}{\partial |z|^\alpha} \right] = -|k|^\alpha \hat{f}(k),$$

with F as the Fourier operator. By taking the time transformation

$$h(t) = \int_0^t \left(\frac{L(0)}{L(s)} \right)^\alpha ds,$$

using the chain rule and substituting this time transformation into (6.11), we get the Chapman-Kolmogorov equation

$$\frac{\partial p_\alpha}{\partial h} = \frac{\partial^\alpha p_\alpha}{\partial |z|^\alpha}. \quad (6.12)$$

This is the evolution equation for a pdf of a standard α -stable Lévy process L_h^α , therefore we have shown Z is a time-changed α -stable Lévy process. Our results are summarized in the following theorem

Theorem 6.2.6. *The rescaled stochastic process $Z := (Z_t, t \geq 0)$ (6.10) is a time-changed standard α -stable Lévy process such that*

$$(Z_t, t \geq 0) \stackrel{\text{dist.}}{=} (L_{h(t)}^\alpha, t \geq 0) \quad (6.13)$$

with

$$h(t) = \int_0^t \left(\frac{L(0)}{L(s)} \right)^\alpha ds.$$

Note that when $\alpha > 2$, the increments dL_t^α have finite mean and variance, therefore the central limit theorem holds and L_t^α will scale as a Brownian motion with $\gamma = 1/2$ as in theorem (6.2.4).

6.2.3 Fractional Brownian motion

In this section we consider a rigorous derivation of the mapping for structures where the displacement of the arms performs fractional Brownian motion (fBm) [21, 43, 68]. We start with a derivation for structures on a radially increasing domain, this is performed since we want to compare the form of the corrected mapping with (5.4). We then consider motion on a general evolving domain $[0, L(t))$.

Definition 6.2.7. A stochastic process $B := (B_t^H, t \geq 0)$ is a standard **fractional Brownian motion** (fBm) with Hurst exponent $H \in (0, 1)$ if $B_0^H = 0$, $\langle B_t^H \rangle = 0$, $B_t^H \sim N(0, t^{2H})$ is a continuous Gaussian process with pdf

$$p(x, t) = \frac{1}{\sqrt{2\pi t^{2H}}} \exp\left(-\frac{x^2}{2t^{2H}}\right) \quad (6.14)$$

and covariance

$$\langle B_t^H B_s^H \rangle = \frac{1}{2}(t^{2H} + s^{2H} - |t - s|^{2H}),$$

for all $t, s \geq 0$.

When $H = 1/2$, the process is a standard Brownian motion and for $H \neq 1/2$ the process is not Markovian or a martingale since it has long range correlations in time and correlated increments [21]. The fBm exhibits local scale invariance (6.1) with $\gamma = H$, since

$$\langle B_{bt}^H, B_{bs}^H \rangle = \frac{b^{2H}}{2}(t^{2H} + s^{2H} - |t - s|^{2H}) = \langle b^H B_t^H, b^H B_s^H \rangle,$$

therefore

$$B_{bt}^H \sim N(0, (bt)^{2H}) \sim b^H N(0, t^{2H}) \sim b^H B_t^H.$$

When the arms are fBm, as before the rescaled process (6.5) on the radial domain can be written in integral form as

$$Z_r = \int_{r_0}^r \frac{r_0}{s} dB_s^H. \quad (6.15)$$

If $H \neq 1/2$ this integral w.r.t fBm cannot be written as a time-changed fBm [83], so the mapping (5.4) strictly does not hold. This is due to memory effects coming from the non-Markovian correlated noise dB_t^H leading to non-independent increments. Nevertheless since for all $r \geq r_0$ the rescaled radial process Z_r has the same state space and law as the fixed process $B_{h(r)}^H$, using fractional calculus we compute and match the mean-squared displacement of Z_r with $B_{h(r)}^H$ for fixed $r \geq r_0$ and $h(r)$ respectively. We represent Z_r in (6.15) as a memory kernel integral with respect to a standard Brownian motion, (see [21] page 48), which leads to

$$Z_r = \int_{r_0}^r \left(K_H * \frac{r_0}{(\cdot)}\right)(s) dB_s \quad (6.16)$$

and the operator K_H is defined below (6.23). In the form (6.16), we match the mean squared displacement of Z_r with $B_{h_H(r)}^H$ such that we have

$$h_H(r) = \left[H(2H - 1) \int_{r_0}^r \int_{r_0}^r \frac{r_0^2}{xy} |x - y|^{2H-2} dx dy \right]^{1/2H}. \quad (6.17)$$

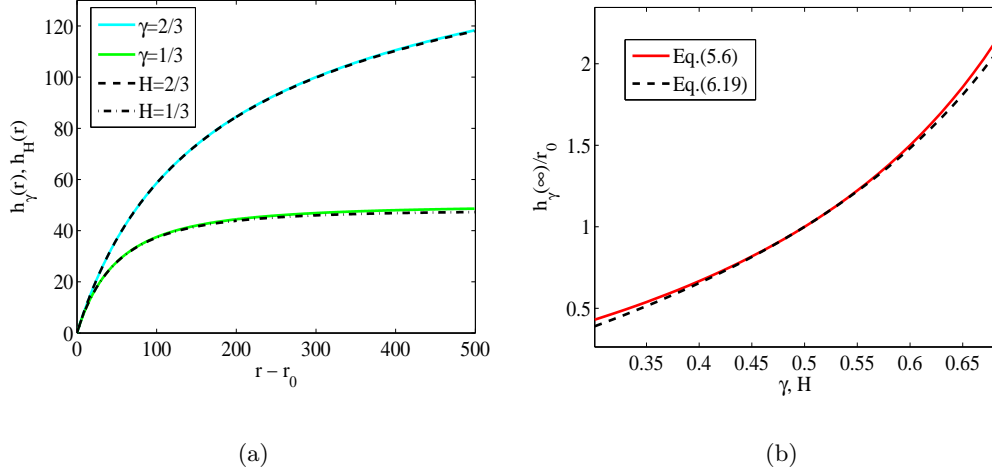


Figure 6.1: Comparison of the mapping (5.4) (full color) and (6.18) (black dashed) for $H = \gamma$ and $r_0 = 100$. (a) Both curves are very similar and behave as $r - r_0$ for r close to r_0 . For large r the functions differ, as shown in (b) the limits $h_\gamma(\infty)$ don't match.

We can also express (6.17) using hypergeometric functions

$${}_2F_1[a, b, c, z] = \sum_{k=0}^{\infty} (a)_k (b)_k / (c)_k z^k / k!,$$

where we denote $(a)_k = a(1+a) \cdots (k-1+a)$. In this notation (6.17) reads

$$h_H(r) = \left[H r_0^2 \int_0^{r-r_0} \left[\frac{(r-r_0-y)^{-1+2H} {}_2F_1 \left[1, -1+2H, 2H, \frac{r_0-r+y}{r_0+y} \right]}{(r_0+y)^2} + \frac{y^{-1+2H} {}_2F_1 \left[1, 1, 2H, -\frac{y}{r_0} \right]}{r_0(y+r_0)} \right] dy \right]^{1/2H}. \quad (6.18)$$

This second representation also holds for $H = 1/2$ where it simplifies to (5.4) with $\gamma = 1/2$. Note that although for $H \neq 1/2$ the expression of (6.18) differs from (5.4), however, visual comparisons of (6.18) and (5.4) shown in Figure 6.1(a) for $H = 1/3$ and $H = 2/3$ show that they are very close.

The small radius behaviour can be found by taking $r \in [r_0, r_0 + \epsilon]$ in (6.17) where ϵ is small, which leads to

$$\lim_{\epsilon \rightarrow 0} \frac{h_H(\epsilon + r_0)}{\epsilon} = \lim_{\epsilon \rightarrow 0} \left[H(2H-1) \int_0^1 \int_0^1 \frac{r_0^2 |x-y|^{2H-2}}{(r_0 + \epsilon x)(r_0 + \epsilon y)} dx dy \right]^{1/2H} = 1.$$

So $h_H(r) \simeq r - r_0$ for r close to r_0 . Note that (6.17) and (5.4) will mostly differ when r is large (see Figure 6.1(b)), where in the limit as $r \rightarrow \infty$ we have

$$\begin{aligned} \lim_{r \rightarrow \infty} h_H(r) &= r_0 \left[H(2H-1) \int_0^\infty \int_0^\infty \frac{|x-y|^{2H-2}}{(x+1)(y+1)} dx dy \right]^{1/2H} = \\ &= r_0 \pi^{\frac{1}{2H}} \left(\frac{H(2H-1)}{(H-1) \sin(2\pi H)} \right)^{\frac{1}{2H}}. \end{aligned} \quad (6.19)$$

Comparing this value to (5.6) we have

$$\lim_{r \rightarrow \infty} h_H(r) \begin{cases} = h_\gamma(\infty) = \frac{\gamma}{1-\gamma} r_0, & \gamma = H = 1/2 \\ < h_\gamma(\infty) = \frac{\gamma}{1-\gamma} r_0, & \gamma = H \neq 1/2 \end{cases}.$$

We now proceed to derive a general form of the mapping (5.17) using an **Itô isometry** approach and consider the general isotropic evolving domain $[0, L(t))$.

Theorem 6.2.8. *Let $L(t) > 0$ for all $t \geq 0$ be continuous. Then for the rescaled process*

$$Z_t = \int_0^t \frac{L(0)}{L(s)} dB_s^H \quad (6.20)$$

the following holds:

$$Z_t \stackrel{\text{dist.}}{=} B_{h_H(t)}^H \quad \text{for all } t \geq 0, \quad (6.21)$$

where

$$h_H(t) = \left(H(2H-1) \int_0^t \int_0^t \frac{L(0)^2}{L(s)L(s')} |s-s'|^{2H-2} ds ds' \right)^{1/2H}.$$

Note that this result is weaker than the previous Markovian cases since it only holds for fixed times and not on the path space. Due to correlations it is not true here that Z_t is a time-changed fBm.

Proof. Take $L(0)/L(t)$ to be continuous, it is known from [21] that (6.20) can be represented

$$Z_t = \int_0^t \left(K_H * \frac{L(0)}{L(\cdot)} \right)(s') dB_{s'}, \quad (6.22)$$

where B_t is a standard Brownian motion. The form of the operator is

$$\left(K_H * \frac{L(0)}{L(\cdot)} \right)(s') = \int_{s'}^t \frac{L(0)}{L(s)} \frac{\partial k_H(s, s')}{\partial s} ds \quad (6.23)$$

where

$$\frac{\partial k_H(s, s')}{\partial s} = c_H \left(\frac{s}{s'} \right)^{H-1/2} (s-s')^{H-3/2},$$

and

$$c_H = \left(\frac{H(2H-1)}{\beta(2-2H, H-1/2)} \right)^{1/2} \quad \text{with} \quad \beta(a, b) = \frac{\gamma(a+b)}{\gamma(a)\gamma(b)}.$$

Define

$$f(s') = \frac{c_H L(0)}{s'^{H-1/2}} \int_{s'}^t \frac{s^{H-1/2} (s-s')^{H-3/2}}{L(s)} ds$$

such that

$$Z_t = \int_0^t f(s') dB_{s'}. \quad (6.24)$$

The rescaled process $\{Z_t\}_{t \geq 0}$ lies on the fixed domain $[0, L(0))$, it will be a Gaussian process [83] such that for $t \geq 0$

$$Z_t \stackrel{dist}{=} B_{h_H(t)}^H.$$

Applying the **Itô isometry** (see [156] page 29)

$$\langle (B_{h_H(t)}^H)^2 \rangle = \int_0^t \left(K_H * \frac{L(0)}{L(\cdot)}(s') \right)^2 ds' \quad (6.25)$$

and further using the isometry of K_H (see [179] page 187) we have

$$\langle (B_{h_H(t)}^H)^2 \rangle = H(2H-1) \int_0^t \int_0^t \frac{L(0)^2}{L(s)L(s')} |s-s'|^{2H-2} ds ds'. \quad (6.26)$$

Since for a standard fBm $\langle (B_{h_H(t)}^H)^2 \rangle = h_H(t)^{2H}$, we therefore have the following representation for a general $L(t)$

$$h_H(t) = \left(H(2H-1) \int_0^t \int_0^t \frac{L(0)^2}{L(s)L(s')} |s-s'|^{2H-2} ds ds' \right)^{1/2H}. \quad \square$$

6.3 Analytical derivation for $\langle N_F \rangle$ and $\langle D_F^2 \rangle$

In this section we derive expressions for the analytical behaviour of the statistics in the fixed domain, as seen in Figure 5.4 and Figure 5.5. For the fBm structures the predictions are exact whereas for the Lévy case we adapt previously known results on the long time behaviour of the density. In both cases our derivation extends on previous known methods to consider the stochastic processes described in the previous section. For the fBm case we adapt the empty interval method in [4], and in addition our formula is derived for finite system sizes $L < \infty$. In the Lévy case we cannot use the empty interval method since the resulting fractional pde which governs $E(x, t)$ is not well posed, so we only look at the regime where the behaviour of the density is governed by a rate equation as found in [126].

6.3.1 Computing statistics for fractional Brownian motion

We use the method of empty intervals to find the inter-particle distribution function (Ipdf), this can be used to predict the average number of particles $\langle N_F(t) \rangle$ for particles with reaction $A + A \rightarrow A$. For a general review on the theory see [4, 135, 148, 180] and references therein. Define $E(x, t)$ to be the probability that at time $t \geq 0$, two arbitrary consecutive particles are at a distance x away from one another. The concentration of particles say $\rho(t)$ is defined to be

$$\rho(t) = -\frac{\partial E}{\partial x} \Big|_{x=0}.$$

For a fixed system with finite size L , we define the function $E : [0, L] \times \mathbb{R}_+ \rightarrow [0, 1]$. The method of empty intervals relies on the Chapman-Kolmogorov equation of the process, where for the standard Brownian motion case this has been derived in [18]. For Brownian motion the square of the spatial increment is $(\Delta x)^2 = dt$, however, for general fBm we take $(\Delta x)^2 = 2Ht^{2H-1}dt$, this leads to $E(x, t)$ satisfying the following partial differential equation [68],

$$\frac{\partial E}{\partial t} = 2\sigma^2 H t^{2H-1} \frac{\partial^2 E}{\partial x^2} \quad (6.27)$$

where σ^2 is a constant and is the prefactor of the mean squared displacement such that $\langle X_t^2 \rangle = \sigma^2 t^{2H}$. Note also that for fBm the empty interval method does not take into account the temporal correlations of the trajectories and as such will only give an approximation of the statistics. The solution of the pde (6.27) should satisfy the Dirichlet boundary conditions

$$E(0, t) = 1 \quad \text{and} \quad E(L, t) = 0 \quad (6.28)$$

and initial condition

$$E(x, 0) = 1_{x \leq 1}. \quad (6.29)$$

This initial condition corresponds to a deterministic fixed particle distance of 1. It is solely used in order to obtain an analytical expression in closed form. It has been already noted in [4] that any sort of generic initial conditions can be taken and do not effect the long time behaviour i.e. $t \gg 1$. We consider the transformed equation

$$\frac{\partial E}{\partial T} = \sigma^2 \frac{\partial^2 E}{\partial x^2} \quad (6.30)$$

obtained from (6.27) by taking the substitution $T = t^{2H}$. To solve (6.30), we construct a free-space Greens function, $V(x, T)$, which is a solution to the adjoint equation

$$-\frac{\partial V}{\partial T} - \sigma^2 \frac{\partial^2 V}{\partial x^2} = \delta(x - x')\delta(T - T'). \quad (6.31)$$

The solution of (6.31) for fixed x' and T' can be found to be

$$V(x, T, x', T') = \begin{cases} \frac{1}{\sqrt{(4\sigma^2(T'-T)\pi)}} \exp\left(-\frac{(x-x')^2}{4\sigma^2(T'-T)}\right), & T \leq T' \\ 0, & T > T' \end{cases}. \quad (6.32)$$

Using the free-space Greens function $V(x, T, x', T')$ we construct a particular Greens function $G(x, T, x', T')$ that satisfies the following

$$\int_0^L \int_0^{T'} \left[G(x, t) \left[\frac{\partial E}{\partial T} - \sigma^2 \frac{\partial^2 E}{\partial x^2} \right] - E(x, t) \left[-\frac{\partial V}{\partial T} - \sigma^2 \frac{\partial^2 V}{\partial x^2} - \delta(x-x')\delta(T-T') \right] \right] dt dx = 0,$$

which simplifies to

$$\int_0^L \left[E(x, T) G(x, T) \right]_{T=0}^{T=T'} dx + \sigma^2 \int_0^{T'} \left[E \frac{\partial G}{\partial x} - G \frac{\partial E}{\partial x} \right]_{x=0}^{x=L} dT = -E(x', T'). \quad (6.33)$$

We take the Greens function $G(x, T, x', T')$ to satisfy the boundary condition $G(0, T, x', T') = 0$ and $G(L, T, x', T') = 0$. This leads to $G(x, T, x', T')$ taking the following form

$$G(x, T, x', T') = \sum_{n=-\infty}^{\infty} [V(x - 2nL, T, x', T') - V(x - 2nL, T, -x', T')] \quad (6.34)$$

where $G(x, T, x', T')$ also satisfies the pde (6.31).

Substituting the form of $G(x, T, x', T')$ into (6.33) and using the boundary conditions (6.28) and initial condition (6.29) leads to

$$E(x', T') = \int_0^1 G(x, 0, x', T') dx + \sigma^2 \int_0^{T'} \frac{\partial G}{\partial x} \Big|_{x=0} dT.$$

Further evaluation gives

$$E(x', T') = \int_0^1 G(x, 0, x', T') dx + \frac{2}{\sqrt{\pi}} \sum_{n=-\infty}^{\infty} \int_{\frac{|x'+2nL|}{\sqrt{4\sigma^2 T'}}}^{\infty} \exp(-u^2) du.$$

Using the definition for the concentration of particles $\rho(T)$ such that

$$\rho(T) = -\frac{\partial E(x, T)}{\partial x} \Big|_{x=0},$$

this leads to the following

$$\begin{aligned} \rho(T) = & \frac{1}{\sqrt{\pi\sigma^2 T}} \sum_{n=-\infty}^{\infty} \left[\exp\left(-\frac{(1-2nL)^2}{4\sigma^2 T}\right) - \exp\left(-\frac{L^2 n^2}{\sigma^2 T}\right) \right] + \\ & \frac{\vartheta_3\left(0, e^{-\frac{L^2}{\sigma^2 T}}\right)}{\sqrt{\pi\sigma^2 T}}, \end{aligned} \quad (6.35)$$

with $\vartheta_3(\cdot, \cdot)$ the elliptic theta function of third kind (see Appendix A for the full expression). The average number of particles $\langle N_F(t) \rangle$ takes the form

$$\begin{aligned} \langle N_F(t) \rangle = L \left[\frac{1}{\sqrt{\pi\sigma^2 t^{2H}}} \sum_{n=-\infty}^{\infty} \left[\exp\left(-\frac{(1-2nL)^2}{4\sigma^2 t^{2H}}\right) - \right. \right. \\ \left. \left. \exp\left(-\frac{L^2 n^2}{\sigma^2 t^{2H}}\right) \right] + \frac{\vartheta_3\left(0, e^{-\frac{L^2}{\sigma^2 t^{2H}}}\right)}{\sqrt{\pi\sigma^2 t^{2H}}} \right], \end{aligned} \quad (6.36)$$

where we have used $\langle N_F(t) \rangle = L\rho(t^{2H})$.

In order to calculate an analytical prediction for $\langle D_F^2(t) \rangle$ we use the inter-particle distance pdf given by

$$p(x, t) = \rho(t)^{-1} \frac{\partial^2 E}{\partial x^2}. \quad (6.37)$$

Using (6.37) we have

$$\langle D_F^2(t) \rangle = -2\rho(t)^{-1} \int_0^L x \frac{\partial E}{\partial x} dx,$$

this leads to

$$\begin{aligned} \langle D_F^2(t) \rangle = -2\rho(t)^{-1} \int_0^L \left[\frac{1}{\sqrt{4\pi t^{2H} \sigma^2}} \sum_{n=-\infty}^{\infty} \left[2 \exp\left(-\frac{(x-2nL)^2}{4t^{2H} \sigma^2}\right) - \right. \right. \\ \left. \exp\left(-\frac{(x-2nL+1)^2}{4t^{2H} \sigma^2}\right) - \exp\left(-\frac{(x+2nL-1)^2}{4t^{2H} \sigma^2}\right) \right] - \\ \left. \frac{\vartheta_3\left(\frac{\pi x}{2L}, e^{-\frac{\pi^2 \sigma^2 t^{2H}}{L^2}}\right)}{L} \right] dx. \end{aligned} \quad (6.38)$$

6.3.2 Computing statistics for α -stable Lévy process

In order to compute the prediction $\langle N_F(t) \rangle$ for coalescing Lévy structures in the fixed domain, we use the general rate equation from [4, 126, 18], this governs the long time dynamics of the density $\rho(t)$. The form of the rate equation follows from (6.35), where as $T = t^{2H} \rightarrow \infty$ and for large system sizes (i.e. $L \rightarrow \infty$) we have

$$\rho(t) = \frac{1}{\sqrt{\pi\sigma^2 t^{2\gamma}}},$$

where we have used $\gamma = H$. Therefore $\rho(t)$ can be seen to satisfy

$$\frac{d\rho}{dt} = -\gamma(\pi\sigma^2)^{\frac{1}{2\gamma}} \rho^{1+1/\gamma}$$

and as for α -stable Lévy processes we have $\gamma = 1/\alpha$, thus the density will satisfy

$$\frac{d\rho}{dt} = -\frac{(\pi\sigma_\alpha)^{\alpha/2}\rho^{1+\alpha}}{\alpha}, \quad (6.39)$$

where σ_α is prefactor as in (6.8). Solving (6.39) leads to

$$\rho(t) = \frac{1}{\sqrt{\pi\sigma_\alpha t^{2/\alpha}}} \quad (6.40)$$

and the number of particles is

$$\langle N_F(t) \rangle = \frac{L}{\sqrt{\pi\sigma_\alpha t^{2/\alpha}}}. \quad (6.41)$$

The form of $\langle D_F^2(t) \rangle$ follows from the following argument. From (6.38) the long time and large scale (i.e. $L \rightarrow \infty$) behaviour for fBm structures is

$$\langle D_F^2(t) \rangle = 4\sigma^2 t^{2\gamma},$$

where $\gamma = H$. For the analogous fixed Lévy structures using that $\gamma = 1/\alpha$, we have

$$\langle D_F^2(t) \rangle \sim t^{2/\alpha}, \quad (6.42)$$

this has been shown in Figure 5.5(b) with fitted prefactors, but in particular giving the right power law behaviour.

Chapter 7

Growth, competition, range expansions and beyond

7.1 Summary of the main results

In this thesis we have investigated stochastic pattern formation occurring in evolving structures which consist of directed arms. A natural example which has been studied in Chapter 3 is growth of two dimensional colonies consisting of competing species. Here the domain boundaries can be interpreted as trajectories of particles moving and interacting on a fixed domain or an evolving domain. In general, as shown in Chapter 5 we treat such systems as locally scale invariant, space-time trajectories of particles under spatially homogeneous but time dependent metric, and map those into more easily tractable systems with constant metric. One of the main benefits of our work is an exact description of asymptotic states, which are found by using predictions for statistics in the fixed domain. Our results are widely applicable, including several natural and physical systems [42, 69, 79, 88, 114].

For the radially growing case we derived the general mapping (5.4) in Chapter 5

$$h(r) = \int_{r_0}^r \left(\frac{r_0}{s}\right)^{1/\gamma} ds = \begin{cases} \frac{\gamma}{1-\gamma} r_0 \left[1 - \left(\frac{r_0}{r}\right)^{\frac{1-\gamma}{\gamma}}\right], & \gamma \neq 1 \\ r_0 \log\left(\frac{r}{r_0}\right), & \gamma = 1 \end{cases}.$$

This mapping is dependent on the local scale invariance exponent of the trajectories. For Brownian motion ($\gamma = 1/2$) and α -stable Lévy processes ($\gamma = \max\{1/\alpha, 1/2\}$) the form of $h(r)$ is exact and for fractional Brownian motion ($\gamma = H$) it is shown to be a good approximation (see Section 5.3).

We have shown it to work directly for local interactions which do not involve a length scale, such as coagulation of point particles (see Chapter 5) and annihila-

tion shown later in this chapter. We have also treated non-local interactions such as branching or finite size particles after mapping the interaction length scales appropriately. Later in this chapter we also consider reactions such as exclusion. We have also characterized general evolving isotropic domains $[0, L(t))$ and derived the mapping (5.17)

$$h(t) = \int_0^t \left(\frac{L(0)}{L(s)} \right)^{1/\gamma} ds,$$

which has also been illustrated in Chapter 5.

The particular real-world application we have focused on is competition in microbial colonies as introduced and described in Chapter 3. We adapted a non-equilibrium growth model by considering a more realistic reproduction time statistic for each individual. This lead to a more generalized form of the standard Eden growth model, where we have used unimodal distributions for the reproduction times T , given by (3.4)

$$T \sim 1 - \delta + \text{Exp}(1/\delta) , \quad \delta \in (0, 1]$$

and we have shown numerical evidence that these δ -family of Eden models still lie in the KPZ universality class. This model has been shown to give similar sectoring patterns and scaling behaviour as in the experiments found in [69, 112], and the differences between the species are solely due to the prefactor σ_δ^2 which we have predicted analytically (4.37) in Chapter 4.

In this chapter we discuss the particular case of radially growing microbial colonies as shown in Figure 2.5. We shall show that under an appropriate mapping these colonies can be understood in a framework of self-affine domain boundaries with annihilating reactions in a linear geometry. This process is closely related to the coalescing system and has been well studied mathematically with analogous results to the ones shown in Section 6.3. We will show that our results contribute to a fundamental understanding to the effects of spatial competition on expanding population fronts as a generic emergent phenomenon for a large class of models. To corroborate our results with good numerical precision, we use the off-lattice based spatial stochastic δ -family of Eden models (see Chapter 3). We would like to stress that the purpose of this model is not an accurate quantitative reproduction of experimental data in [69], but a contribution to the fundamental understanding of processes such as competition and the effects of expanding population fronts. In particular, this application combines many results derived throughout the thesis and is a befitting end to our journey. We also include a section with possible other growth models that can be studied under the setting of our theory, which includes applications with potentially interesting consequences.

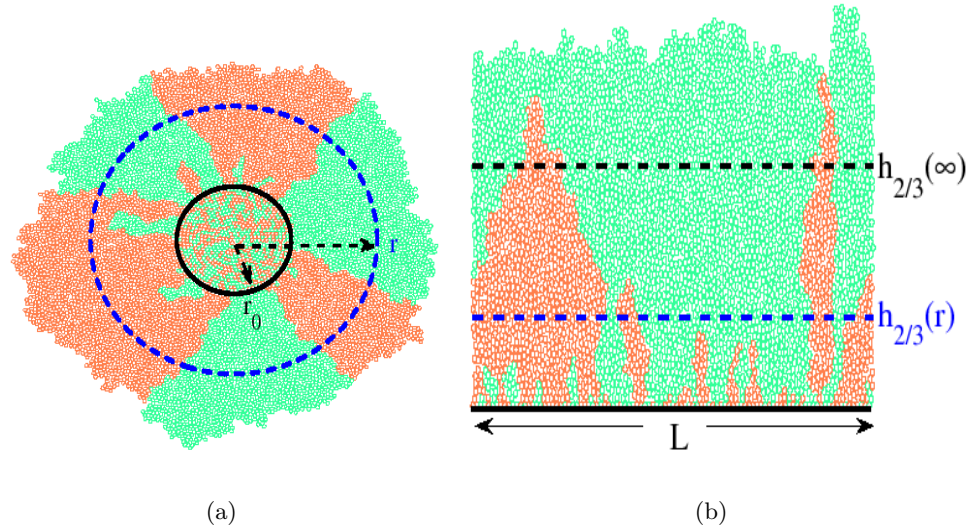


Figure 7.1: Simulations of colonies from the δ -family of Eden models introduced in Chapter 3 for $\delta = 1$. (a) Circular colony with an initial radius of $r_0 = 16$, grown up to a simulation time $t = 30$, leading to a final radius of approximately 55. (b) A linear colony with periodic boundary conditions in lateral direction with width $L = 100 \approx 2\pi r_0$, and the colonies are grown to a simulation time $t = 40$, leading to a height of approximately 50. The different colors denote cell types 1 and 2.

7.2 Population fronts in competition growth models

7.2.1 Introduction

Spatial expansion is ubiquitous to many processes across the physical world and they are particularly noticeable in ecological systems. The history of many species shows episodes of range contraction and expansion [57, 209, 211]. For many species range expansion leads to a decrease in heterozygosity in the population i.e. the number of different alleles decreases [2, 44]. As discussed in Chapter 1 processes such as range expansion, genetic drift and natural selection lead to the emergence of branching in the tree of life. Interesting, these evolutionary processes can be discussed in terms of the microbial populations as seen in Figure 2.5 and studied in [69]. Therefore our novel approach in understanding such systems is even applicable to more complicated biological phenomenon.

In this section we study the spatial distribution of radially growing clusters such as the microbial experiments shown in Figure 2.5. These colonies as well as simulations (see Figure 7.1) suggest that fluctuations at the frontier of a two-

dimensional range expansion can generate genetic sectoring patterns with fractal domain boundaries. Competition in these systems drives a coarsening process which gives rise to sectoring patterns and this leads to a gradual decrease in the number of sectors. As mentioned in the previous section, these systems can be studied by modelling the fluctuating tip of domain boundaries analogous to the systems studied in Chapter 5. For the strip geometry, due to the finite available space the effect of spatial competition leads to a decrease in diversity and eventually only one domain remains at the population front. In contrast, for the radially growing cluster, adding the component of spatial expansion leads to a change not just in the morphology of the patterns that can be observed but also affects the asymptotic behaviour. In general, spatial expansion can be seen as a component which is vital for biodiversity, coexistence and stability in nature.

The main result of this chapter is to understand the domain coarsening under range expansions via mapping to a generic linear geometry as discussed in Chapter 5. This will be in terms of simulations and results as shown in Chapter 3 and as discussed is applicable to the experiments in [69] and [112]. As a consequence, we can fully understand the distribution of the sectoring patterns under isotropic range expansions, as illustrated in Figure 7.1.

We use the mapping (6.17) to map the number of sectors $\langle N \rangle$ from the radially growing Eden model to the linear model on the strip geometry. The approach we take is solely based on the theory presented in Chapter 5 and to our knowledge this presents a new approach to separate the domain coarsening due to competition and the domain growth due to range expansion.

7.2.2 Equivalence of radial and fixed domain colonies

In Figure 7.2 we show a radial expanding annihilating structure and the corresponding structure on the fixed domain with periodic boundary conditions at the edges. The arms perform fractional Brownian motion. A visual comparison with Figure 7.1 shows a striking resemblance, where in both cases the interaction of annihilation leads to a gradual decrease in the number of arms. We therefore study the domain boundaries for the δ -family of Eden colonies (as defined in Section 3.3.2) in terms of the framework of Chapter 5.

Let $X := (X_h, h \geq 0)$ with $X_h \in [0, L)$ be an arm in a fixed structure on the strip geometry. In Section 3.3.2 we have shown that these arms can be well described by fractional Brownian motion (fBm) with Hurst exponent $H = 2/3$ and have a multiplicative factor σ_δ^2 in their mean squared displacement (3.19). In the analogous radial geometry, as before we represent each arm on the perimeter of a

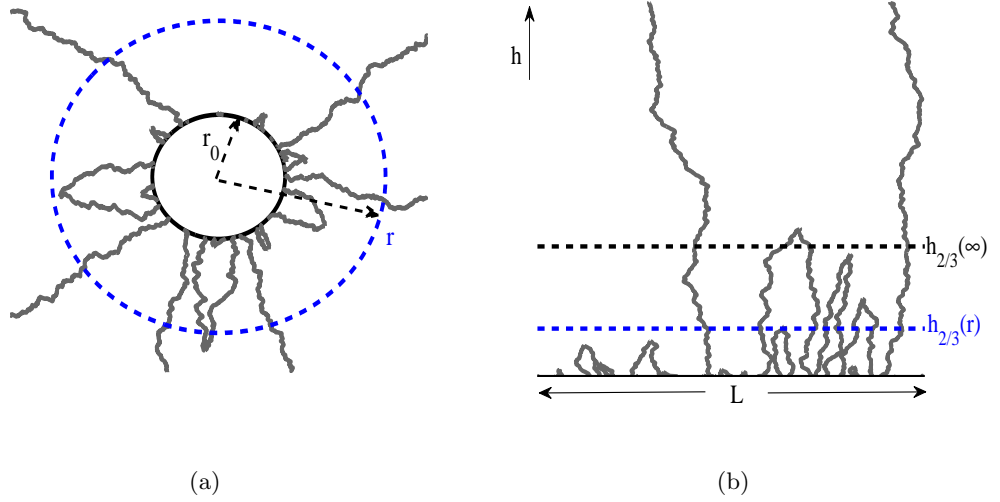


Figure 7.2: Expanding radial growth structure and the same structure on a fixed domain with periodic boundary conditions, illustrated for fractional Brownian motions ($H = 2/3$) with prefactor $\sigma_{\delta=1}^2 \approx 0.44$ and the particles interact through annihilation. The distribution of the rescaled structure at radius r is identical to the distribution of the fixed domain structure at height $h_{2/3}(r)$ as given by (7.3), indicated by a blue dashed line. The asymptotic behaviour of the radial structure is given by the limit of the mapping $h_{2/3}(\infty)$ (6.19), shown in the fixed domain as a black dashed line. Parameters are $L = 100$ with $r_0 = L/2\pi$ and initially 50 arms.

growing circle as

$$Y_r \in [0, 2\pi r) \quad \text{with} \quad r \geq r_0. \quad (7.1)$$

In order to connect the two domains we take $r_0 = L/2\pi$ and have periodic boundary conditions at the edges of each domain. Here we use the prediction of σ_δ^2 , found in Chapter 4 to be

$$\sigma_\delta^2 \approx 0.2685(\delta^2 + 0.4194)^{4/3}. \quad (7.2)$$

For the fBm case with general $H \in (0, 1)$ we have computed the exact mapping (6.17) to be

$$h_H(r) = \left[H(2H - 1) \int_{r_0}^r \int_{r_0}^r \frac{r_0^2}{ts} |t - s|^{2H-2} ds dt \right]^{1/2H}. \quad (7.3)$$

In Figure 7.3 we show the average number of sectors $\langle N \rangle$ for both the linear and radial δ -family Eden simulations. In the linear case as seen before in Sec-

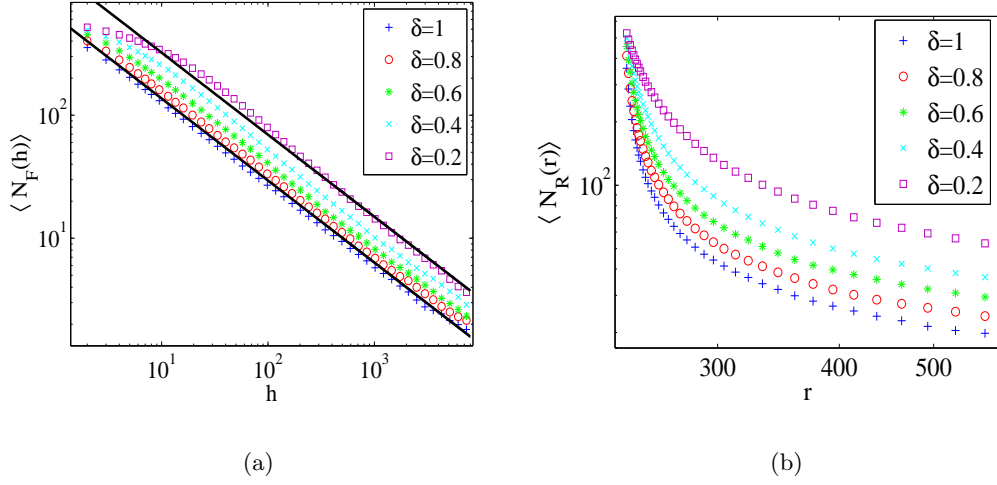


Figure 7.3: The average number of sectors $\langle N \rangle$ shown for the radial and linear δ -family of Eden models. We have $r_0 = L/(2\pi)$ and $L = 1500$ and the initial type are randomly assigned with equal probability. (a) For each δ value, $\langle N \rangle$ can be seen to follow a power law (7.4) with exponent $-2/3$, shown for the values $\delta = 1$ and $\delta = 0.2$ by the black curve with σ_δ^2 as in (7.2). (b) Due to the expansion in the domain, $\langle N_R(r) \rangle$ is a decreasing function which converges to a non-trivial limit greater than 1.

tion 3.3.3, the number of sectors $\langle N_F \rangle$ decrease as a power law with

$$\langle N_F(h) \rangle = \frac{L}{\sqrt{4\pi\sigma_\delta^2 h^{4/3}}}, \quad (7.4)$$

shown as the black solid curve and compared to data with $\delta = 1$ and $\delta = 0.2$ with σ_δ^2 as in (7.2). As discussed in Chapter 5 for these structures due to the finite available space, fixation always occurs $N_F(h) \rightarrow 1$ as $h \rightarrow \infty$, where for large L the average fixation time scales as

$$\tau \sim (L^2/\sigma_\delta^2)^{3/4} \sim (r_0^2/\sigma_\delta^2)^{3/4}.$$

For large systems ($r_0 \rightarrow \infty$), typically τ is much larger then the limit of the mapping $h_\gamma(\infty) \sim r_0$ given in (6.19). In Figure 7.3(b), we show the corresponding number of sectors $\langle N_R(r) \rangle$ for the radial model for several values of δ . For this model, analogous to the behaviour displayed in Figure 5.2(a) we expect that $N_R(r)$ decreases to a random limit typically taking values larger than 1 (see below).

Figure 7.4(a) shows the behaviour of $\langle N_R(r) \rangle$ after applying the mapping (7.3). As observed, the mapping works well and the full behaviour of the radial

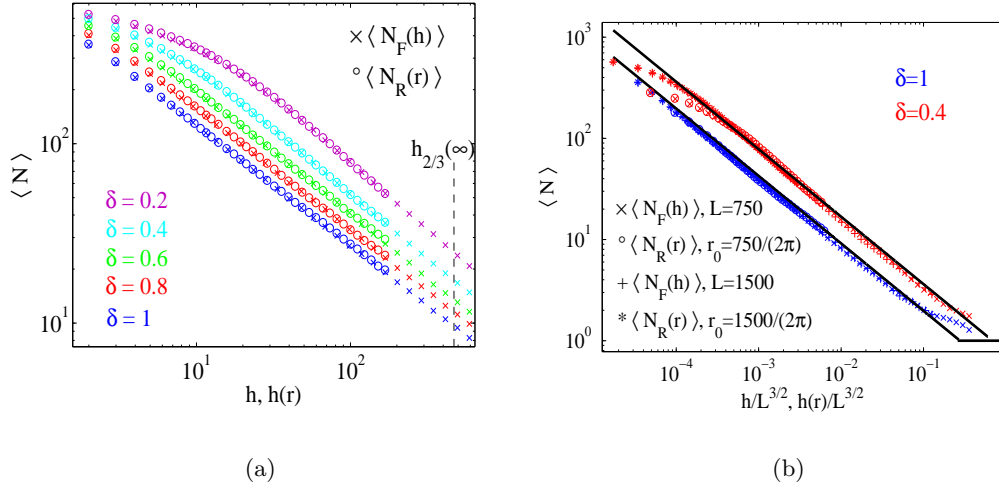


Figure 7.4: Illustrating the mapping (7.3) with $H = 2/3$ for the data $\langle N \rangle$ as shown in Figure 7.3. (a) For each δ value, we plot $\langle N_R(r) \rangle$ vs $h_H(r)$ and obtain a good data collapse with $\langle N_F(h) \rangle$. The dashed black line corresponds to the limit $h_{2/3}(\infty)$ given in (6.19). In (b) we show that a collapse of data with different system sizes can be achieved if we rescale the horizontal axis by $L^{3/2}$. Data are shown for two L values with $r_0 = L/(2\pi)$ and the black line is the prediction (7.4).

colonies can be understood through the linear model. Combining (6.19) and (7.4) gives an exact expression for the non-trivial limit

$$\lim_{r \rightarrow \infty} \langle N_R(r) \rangle = r_0^{1/3} \sqrt{\frac{3 \sin(\pi/3)}{2\sigma_\delta^2}}. \quad (7.5)$$

An interesting result is given in Figure 7.4(b) showing that the behaviour of $\langle N \rangle$ can be represented independent of the system size L . As illustrated for the $\delta = 1$ and $\delta = 0.4$ data, by plotting $\langle N_F(h) \rangle$ vs $h/L^{3/2}$ we obtain a data collapse for several L analogous to Figure 3.11. This is further confirmation that the only significant parameter in these systems is the exponent $\gamma = H$.

7.2.3 Discussion

In this section using the δ -family of Eden models described in Chapter 3, we have presented numerical evidence that the segregation patterns on expanding population fronts can be understood by the mapping $h_H(r)$ with domain boundaries being modelled by fractional Brownian motion. This leads to a complete understanding

of the sector statistics for expanding circular geometries in terms of linear growth models with fixed width L , which have been studied in great detail in the mathematics literature. We believe that this approach is applicable in various situations, and provides a general understanding of the competing effects of genetic drift and range expansions on population fronts. In general, the spatiotemporal dynamics of interacting components is fundamentally important in characterization of many systems. The behaviour displayed is a generic emergent phenomenon and exists for a large class of models in the field of non-equilibrium statistical mechanics [177, 178].

The mapping (7.3) implies that $h_H(r)$ converges to a finite limit $h_H(\infty)$ as $r \rightarrow \infty$ as long as $H = \gamma < 1$. So as long as the motion of sector boundaries is not ballistic (i.e. $\gamma < 1$), expansion will dominate the sector coarsening process and there is no fixation for expanding population fronts in a radial geometry. Ballistic sector boundaries can result from differences between the species fitness i.e. different reproduction rates r_1 and r_2 for each species, leading to selective advantages for one species. In that case the effects of circular range expansion and coarsening are on the same scale, which leads to interesting competition effects and can be explained with the generalized form of the mapping (5.4) in particular cases, which is subject to future research. On the other hand, the strength of the range expansion can also be affected by non-circular geometries which lead to a non-linear growth of the population front with distance. This could be the result of certain geometrical constraints in the growth medium such as a landscape, which can therefore affect the biodiversity at the population front. We still expect that such systems can be understood by a mapping to the linear experiment analogous to the one presented in Chapter 5. In general, the linear model provides the prototype for the pure coarsening effects due to genetic drift, and the full behaviour is determined by an interplay with geometric effects, which can be summarized in an effective mapping. The mathematical basis of this argument is the space-time symmetry and local scale invariance of the boundaries. Note also that the sector boundaries inside the population do not have to be static in more general situations. But as long as the range expansion is fast enough, changes due to death, migration or reproduction inside the population will not affect the behaviour at the population front. So our approach is widely applicable for locally reproducing species under range expansions, as long as boundary growth is the fastest relevant process in the system.

According to the well established paradigm of the KPZ universality class [95], for certain processes the roughness of the population front is largely independent of the microscopic details such as growth rules. This occurs as long as the spatial and temporal correlation lengths resulting from these details are small compared to the

system size and growth time, respectively. If this is the case, the exponent γ of the sector boundaries is therefore not affected by details of the mode of reproduction of a single individual, which will only influence the prefactor σ_δ . This determines the width of the sectors in the linear geometry in a very simple fashion (see Eq. (7.4)), whereas the mapping in general form $h(r)$ is independent of σ_δ . Therefore our result is expected to describe the sectoring patterns of a large class of locally reproducing species, and quite strikingly, all microscopic details can be summarized in the single parameter σ_δ . The continuum time and space δ -family of Eden models is only a simple caricature of that class, where we have assumed that cells divide in a spatially homogeneous fashion and follow reproduction times distributed by the δ -family (3.4). Although these assumptions may not hold for all microbial species, the correlation lengths referred to above are quite small and our simulations are therefore a good coarse-grained model on a macroscopic level (see Figure 7.1). To get the best possible agreement one would have to fit the variation parameter δ from a large set of experimental data. It is intriguing that we can predict the parameter σ_δ from the microscopic details of the mode of replication, as done in Chapter 4. A smaller value of σ_δ leads to explaining the yeast (*S. cerevisiae*) sectoring patterns (cf. Figure 3.3). Where the significantly finer patterns than the ones observed for *E. coli* correspond to a reduced fluctuations of the boundaries and a smaller value of the variation parameter δ , due to the temporal aspects of the reproduction playing a major role. Also other microscopic differences may have to be considered here, where amongst other characteristics, noticeably, cell shape and multiplication procedure are important [36, 183].

7.3 Further applications

7.3.1 Non-local growth and DLA

Various growth phenomena leading to the formation of random patterns have been studied extensively. In this thesis we have focused on the cases where behaviour arises from local growth rules. Further important classes of growth models are those which do not obey local growth rules and rates depend on the entire geometry of the cluster [9, 192, 216]. Amongst such models the diffusion limited aggregation (DLA) is a very basic one, but very important because it represents the limiting case of realistic growing phenomena [15, 16, 193]. On a subset of \mathbb{R}^2 the DLA model generates a self-similar structure with fractal dimension $D \approx 1.71$ [138, 141]. DLA clusters are randomly branched structures that exhibit constant tip splitting growth. The structures in these clusters is seen to be outwardly and open random

trajectories, with no characteristic length scale except for the size of the cluster and internal branch thickness. In physical and biological processes, phenomena such as DLA are observed under diffusion limited conditions. For example in microbial colonies, formation of DLA structures emerge for high agar concentrations and low nutrient concentrations (see Figure 2.4). In this parameter regime, it is known that the growth is dominated by the diffusion of the nutrients [155, 205]. The main reason for the self-similar nature of the cluster, is because of an inherent instability, where the nutrients are used up by the cells which are situated at the most advanced parts of the surface. This leads to empty regions in parts of the petri dish that contain insufficient nutrient levels for growth, and thus causes the appearance of a branched morphology. Since DLA cluster growth is simply limited by common diffusion processes, it is therefore not surprising that these clusters are observed across the physical world, including systems such as electrochemical deposition [66, 128], dielectric break-down [152], viscous fingering [161] and crystal growth [153]. The DLA process is far from equilibrium and history dependent, such that the internal pattern reflects the growth itself. In the framework of this thesis, we can attempt to describe these clusters by a collection of competing arms which appear to have a random outward directed motion and lead to an emergence of a branched structure. The growth and competition is dependent on the flux particle input, where the arms which are more branched out receive more particles. This non-local growth rule leads to strong correlations on the surface.

For DLA the overall geometry has a strong impact on growth processes, where in constant width channel geometry a stable arm will eventually propagate [176], while in radial geometry a continuously tip splitting branched structure emerges, with the number of arms in the asymptotic regime [197] still open to debate [15, 73, 133]. An interesting extension of our results would be to determine how to include non-local effects in the mapping such that we can also characterize these sort of systems. We believe that these systems may still be treatable with an extension to the models shown in Section 5.5. In order to perform an exact mapping we would have to consider the relative size of the particle compared to the system size, which has already been done in Section 5.5. By mapping the radially growing structure to the fixed structure, we would have to rescale the particle size in the fixed domain such that we have

$$d_F = \frac{r_0}{r(h)} d_R.$$

In order to describe DLA structures in our framework, we would have to determine the self-affine exponent γ for each arm and the effective branching rate so we can use the generalized mapping (5.4). Our plan is to use this approach in order to

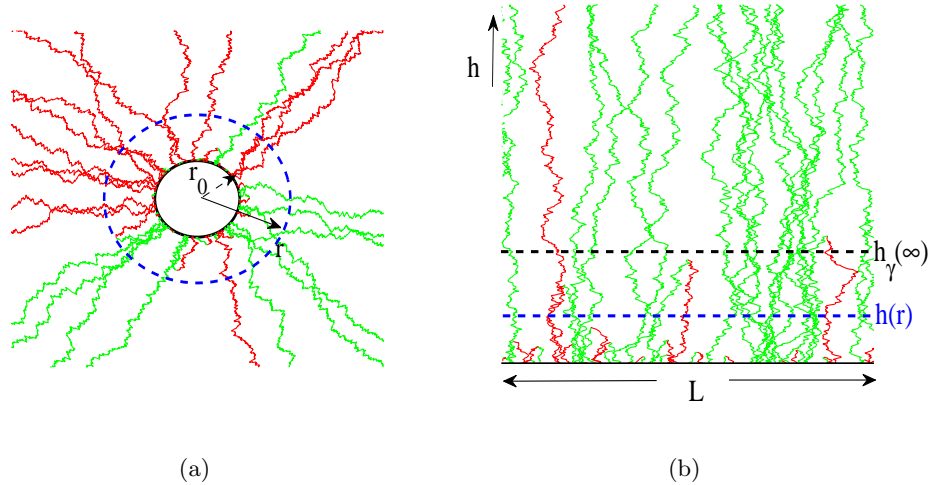


Figure 7.5: Expanding radial growth structure and the same structure on a fixed domain with periodic boundary conditions, illustrated for the case of annihilating Brownian motion ($\gamma = 1/2$). The particles are assigned a random type either A or B , and only interact with the opposite type by annihilation. The distribution of the rescaled structure at radius r is identical to the distribution of the fixed domain structure at height $h(r)$ as given by (5.4), indicated by a blue dashed line. Parameters are $L = 100$ with $r_0 = L/2\pi$, unit diffusion coefficient and initially 100 arms.

make a novel contribution to determine the asymptotic number of arms in a radial cluster by running high resolution DLA simulations on the strip geometry.

7.3.2 Possible application in cosmology

Another interesting model is a spatial fluctuating annihilation model with two or more distinct particle types. For the two type case, the particles perform random motion in space \mathbb{R}^n with $n > 0$ and annihilate when they meet different types i.e. $A + B \rightarrow \emptyset$, whereas they do not interact with the same type. An example of such a system in $n = 1$ spatial dimensions is shown in Figure 7.5 for radially growing and fixed directed structures, where the particles perform Brownian motion with $\gamma = 1/2$. The dynamics leads to the formation of clusters defined to be sets of neighbouring particles of the same type. In the fixed geometry as before, because of the finite size only one type will remain if initial numbers are random or the system will be empty if initial numbers are the same. This will be the same in the growing

radial cluster for $\gamma \geq 1$, however, for $\gamma < 1$ despite initial conditions due to the linear expansion we will always have a co-existence between different types.

This is further illustrated by computing several statistics as shown in Figure 7.6 for these Brownian structures with a random number of initial type A and B . Here $\langle CN \rangle$ denotes the number of clusters, which decreases with particle movement and interaction between different types. $\langle CD \rangle$ denotes the total distance between neighbouring clusters. For the fixed structure this will be monotonically increasing until there remains only one type. The cluster size denoted as $\langle CS \rangle$ is the number of particles per cluster, which increases due to the independence between same types and annihilation between different types. We can see that by using the mapping (5.4) with $\gamma = 1/2$ the growing radial clusters can be mapped to the fixed structure. In $n \geq 2$ dimensions these clusters are harder to define and it is easier to work with correlation functions.

Although these cluster models are clearly an over simplification, an ambitious application in $n = 3$ spatial dimensions would be to study cosmological fields such as the early universe during the inflationary period, (see [76, 131] and references within). An interesting question would be, if using such a model, we can make a contribution to the apparent asymmetry of matter and antimatter in the visible universe, which is one of the major unsolved problems in astrophysics, (see [3, 74] and references within). The basic idea is that the expansion of the universe leads to spatial separation of matter and antimatter on characteristic scales, which one might be able to predict using estimates for the expansion rate and the initial conditions, including the total amount of mass. Of course the model and simulations in the current form need significant fine tuning, where we would have to find the value of γ and the right geometrical manifold. For instance the sphere $S^3(r)$ is a simplification of the actual shape of the universe and it has been proposed in [130] that the shape is a Poincaré dodecahedral. Another question would be the expansion rate, was it linear, ballistic or exponential? Whilst these simulation parameters are not yet known to us, it is exciting to think that such a simple function as (5.4) could have such wide applications.

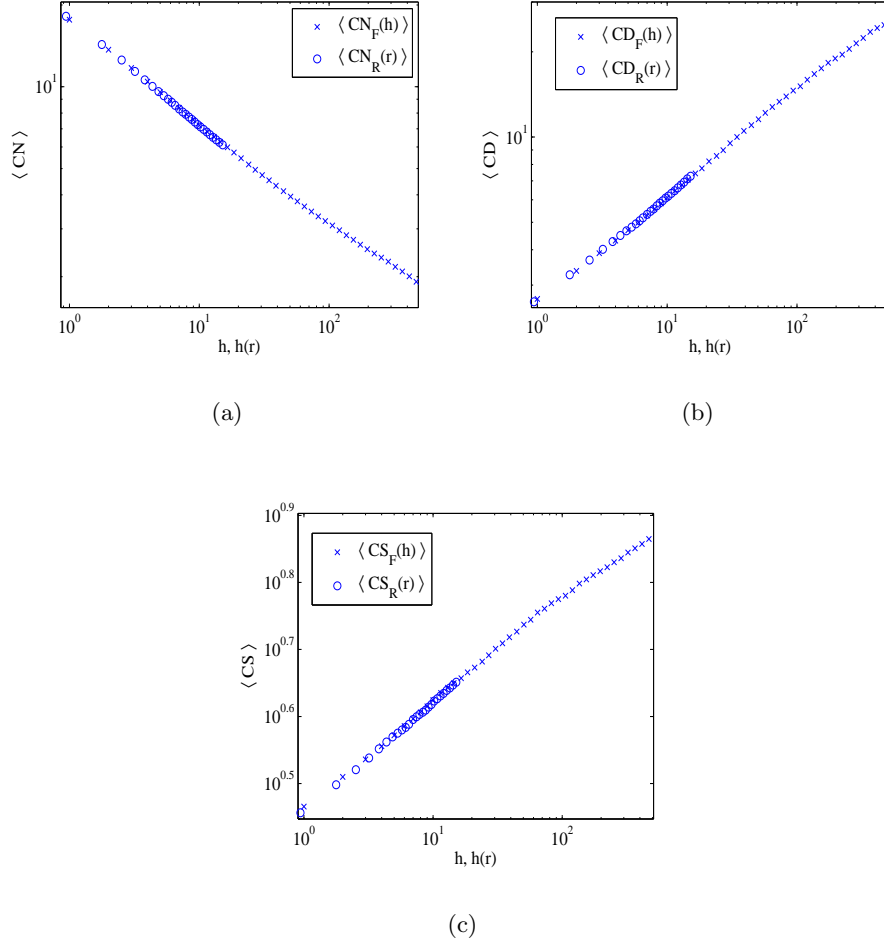


Figure 7.6: Statistics from a fixed domain and growing radial domain for a system as illustrated in Figure (7.5). Here we take $L = 100$ and $r_0 = L/(2\pi)$. The particles of types A and B , perform Brownian motion with the reaction condition $A + B \rightarrow \emptyset$ and do not interact otherwise. We use the mapping (5.4) with $\gamma = 1/2$ to plot the radial statistics $\langle CN_R(r) \rangle$, $\langle CD_R(r) \rangle$ and $\langle CS_R(r) \rangle$ vs $h(r)$ to obtain a data collapse. The data is shown for (a) number of clusters, (b) distance between neighbouring clusters and (c) cluster size i.e. number of particles in a cluster.

Appendix A

Elliptic theta functions

Here we give a list of the four elliptic theta functions. Let $z, q \in \mathbb{C}$ and $|q| < 1$. The elliptic theta function of the i^{th} kind is denoted as $\vartheta_i(z, q)$ and reads

1.

$$\vartheta_1(z, q) = 2q^{1/4} \sum_{n=0}^{\infty} (-1)^n q^{n(n+1)} \sin((2n+1)z),$$

2.

$$\vartheta_2(z, q) = 2q^{1/4} \sum_{n=0}^{\infty} q^{n(n+1)} \cos((2n+1)z),$$

3.

$$\vartheta_3(z, q) = 1 + 2 \sum_{n=1}^{\infty} q^{n^2} \cos(2nz),$$

4.

$$\vartheta_4(z, q) = 1 + 2 \sum_{n=1}^{\infty} (-1)^n q^{n^2} \cos(2nz).$$

The function $\vartheta_3(\pi z, q)$ is known as the Jacobi theta function and with q fixed is a Fourier transform for an entire function of z with period 1, and hence satisfies the identity $\vartheta_3(\pi(z+1), q) = \vartheta_3(\pi z, q)$. Also, $\vartheta_3(\pi z, q)$ is quasi-periodic where

$$\vartheta_3(\pi z - bi \log q, q) = q^{-b^2} \exp(-2\pi i b z) \vartheta_3(\pi z, q),$$

where $i = \sqrt{-1}$ and $b \in \mathbb{Z}$. In Section 5.3 and Section 6.3.1, we use the function $\vartheta_3(z, q)$ in the expression of the prediction of $\langle N_F(h) \rangle$ and $\langle D_F^2(h) \rangle$. For further reading see [1] page 569.

Appendix B

Stochastic analysis

Here we provide a background on the probability aspects used throughout the thesis. A more in depth review can be found in Sections 3, 4, 5 and 8 of [156].

B.1 Probability space

Let $(\Omega, \mathcal{F}, \mathbb{P})$ denote a probability space with probability measure \mathbb{P} . We have $\mathbb{P}(\Omega) = 1$ and the σ -algebra \mathcal{F} (also sometimes referred to as the σ -field) is a collection of subsets of Ω such that:

1. $\emptyset, \Omega \in \mathcal{F}$
2. If $A \in \mathcal{F} \Rightarrow A^c \in \mathcal{F}$, where $A^c = \{\omega \in \Omega \mid \omega \notin A\}$
3. $\{A_i\}_{i \in \mathbb{N}} \subset \mathcal{F} \Rightarrow \cup_{i \in \mathbb{N}} A_i \in \mathcal{F}$.

A random variable X on a probability space $(\Omega, \mathcal{F}, \mathbb{P})$ is such that $X : \Omega \rightarrow \mathbb{R}$. Define the Borel- σ -algebra $\mathbb{B}(\mathbb{R})$ to be the smallest σ -algebra to contain all the open subsets of \mathbb{R} (i.e. contains the topology). A random variable X is a measurable function satisfying

$$\{\omega \in \Omega, X(\omega) \in A\} \in \mathcal{F} \quad \text{for all } A \in \mathbb{B}(\mathbb{R}).$$

Define the $\mathcal{L}^p(\Omega, \mathcal{F}, \mathbb{P})$ vector space with $p > 0$ such that

$$\mathcal{L}^p(\Omega, \mathcal{F}, \mathbb{P}) := \{X : \Omega \rightarrow \mathbb{R} \mid \|X\|_{L^p} < \infty\},$$

with

$$\|X\|_{L^p} = (\mathbb{E}[X^p])^{1/p}, \tag{B.1}$$

where

$$\mathbb{E}[X] = \int_{\Omega} X(\omega) d\mathbb{P}(\omega)$$

is the expectation operator. Note if $\|X\|_{L^p} = 0$ this implies $X = 0$ almost surely (a.s. i.e. $\mathbb{P}(X \neq 0) = 0$). The vector space $\mathcal{L}^p(\Omega, \mathcal{F}, \mathbb{P})$ will be a Banach space with the norm (B.1) and if $p = 2$ then this will be a Hilbert space with inner product $\mathbb{E}[XY]$ for $X, Y \in \mathcal{L}^2(\Omega, \mathcal{F}, \mathbb{P})$. We call $\sigma(X)$ the σ -algebra generated by X , the smallest σ -algebra with respect to which X is measurable and contains the sets

$$\{\{\omega \in \Omega \mid X(\omega) \in A\} \mid \text{for all } A \in \mathbb{B}(\mathbb{R})\}.$$

B.2 Stochastic process

A stochastic process on a probability space $(\Omega, \mathcal{F}, \mathbb{P})$ is defined as a family of random variables $X := (X_t, t \geq 0)$. For each $t > 0$, we have $X_t : \Omega \rightarrow \mathbb{R}$ and measurable with respect to \mathcal{F} . A filtration $\{\mathcal{F}_t, t \geq 0\}$ is an increasing sequence of σ -algebras such that

$$\mathcal{F} = \cup_{t \geq 0} \mathcal{F}_t,$$

and for all $t \geq s$ we have $\mathcal{F}_s \subseteq \mathcal{F}_t$. The natural filtration is defined as the smallest collection of σ -algebras with respect to which all X_t are measurable and can be taken as

$$\mathcal{F}_t = \sigma(\{X_s, 0 \leq s \leq t\}).$$

The filtration represents all possible information of the process $(X_t, t \geq 0)$.

B.3 Stochastic integration

Let $(\Omega, \mathcal{F}_t, \mathbb{P})$ be a filtered probability space and $B := (B_t, t \geq 0)$ a standard Brownian motion as defined in (6.2.2) and adapted to a filtration $\{\mathcal{F}_t, t \geq 0\}$. Let the process $Y := (Y_t, t \geq 0)$ be continuous process adapted to $(\mathcal{F}_t, t \geq 0)$ such that for all $t \geq 0$

$$\int_0^t \mathbb{E}[Y_s^2] ds < \infty.$$

The term adapted means that Y_t is measurable with respect to \mathcal{F}_t for all $t \geq 0$.

The stochastic process $Z : (Z_t, t \geq 0)$ such that

$$Z_t = \int_0^t Y_s dB_s \tag{B.2}$$

exists on the space $(\Omega, \mathcal{F}_t, \mathbb{P})$. Note that in this case the filtration $(\mathcal{F}_t, t \geq 0)$ can be taken to generated by the process B . The stochastic process Z_t can be constructed

as follows: We take the elementary form of the process Y , on a time interval $[0, t]$ this takes the form

$$Y_s = Y_0 + \sum_{i=1}^n Y_{t_i} 1_{(t_{i-1}, t_i]}(s),$$

where $0 = t_0 < t_1 < \dots < t_n = t$ is a particular partition of $[0, t]$. Define the stochastic sum

$$Z_t^n := \sum_{i=0}^n Y_{t_{i-1}} (B_{t_i} - B_{t_{i-1}}), \quad (\text{B.3})$$

then

$$Z_t^n \xrightarrow{\mathcal{L}^2} Z_t \quad \text{as } n \rightarrow \infty,$$

and subsequently this convergence also holds in probability \mathbb{P} .

Let $(Y_t, t \geq 0)$ be a continuous deterministic function which is square summable, then the stochastic process as defined in (B.2) is a continuous martingale as given by the definition (6.2.3). This can be seen using the elementary process Z_t^n , we take $t > s'$ such that $0 = t_0 < t_1 < \dots < t_m = s' < \dots < t_n = t$

$$\mathbb{E}[Z_t^n | \mathcal{F}_{s'}] = \sum_{i=0}^n Y_{t_{i-1}} \mathbb{E}[B_{t_i} - B_{t_{i-1}} | \mathcal{F}_{s'}]$$

and since

$$\mathbb{E}[B_{t_i} - B_{t_{i-1}} | \mathcal{F}_{s'}] = \begin{cases} 0, & t_{i-1} \geq s' \\ B_{t_i} - B_{t_{i-1}}, & t_{i-1} < s' \end{cases}.$$

We have

$$\mathbb{E}[Z_t^n | \mathcal{F}_{s'}] = \sum_{i=0}^m Y_{t_{i-1}} (B_{t_i} - B_{t_{i-1}}) = Z_{s'}^m$$

and using

$$Z_{s'}^m \xrightarrow{\mathcal{L}^2} Z_{s'} \quad \text{as } m \rightarrow \infty,$$

therefore $\mathbb{E}[Z_t | \mathcal{F}_{s'}] = Z_{s'}$ for all $t > s'$.

The quadratic variation of the process $X = (X_t, t \geq 0)$ is defined by

$$[X]_t := \lim_{n \rightarrow \infty} \sum_{i=0}^n (X_{t_i} - X_{t_{i-1}})^2 \quad (\text{B.4})$$

where $0 = t_0 < t_1 < \dots < t_n = t$ is a partition of the interval $[0, t]$. For the process Z (B.2), in increment form we have

$$(Z_{t_i}^n - Z_{t_{i-1}}^n)^2 = Y_{t_{i-1}}^2 \Delta t$$

where we have used (see [156] page 48)

$$(B_{t_i} - B_{t_{i-1}})^2 \xrightarrow{\mathcal{L}^2} \Delta t \quad \text{as } t_i - t_{i-1} = \Delta t \rightarrow 0.$$

Then analogous to the Riemann integral, the quadratic variation (B.4) of Z_t is (see [156] page 163)

$$[Z]_t = \int_0^t Y_s^2 ds. \quad (\text{B.5})$$

Note that since $(Y_t, t \geq 0)$ is a deterministic function, then $[Z]_t$ is also deterministic and equal to the mean squared displacement $\mathbb{E}[Z_t^2]$, which is used in Section 6.2.

The process Z_t as in (B.2) with $[Z]_t$ increasing is a time-changed Brownian motion. This results follows from the following theorem:

Theorem B.3.1. *[Lévy characterization of Brownian Motion] Let X be a continuous martingale with $X_0 = 0$. Then the following are equivalent.*

- (i) X is standard Brownian motion on the underlying filtered probability space.
- (ii) $X_t^2 - t$ is a martingale.
- (iii) X has a quadratic variation $[X]_t = t$.

Note that by a corollary to (B.3.1), the process Z_t is a time-change Brownian motion (see [106] page 103) such that

$$Z_t = B_{[Z]_t}.$$

B.4 Itô formula

Let $X := (X_t, t \geq 0)$ be a stochastic process such that it satisfies the stochastic differential equation (SDE)

$$dX_t = a(X_t, t)dt + \sigma(X_t, t)dB_t, \quad (\text{B.6})$$

where B_t is a Brownian motion. Note that (B.6) is an increment form of the integral equation

$$X_t = X_0 + \int_0^t a(X_s, s) ds + \int_0^t \sigma(X_s, s) dB_s.$$

Let

$$f \in C^{2,1}(\mathbb{R} \times \mathbb{R}_+, \mathbb{R})$$

i.e. twice differentiable in space $x \in \mathbb{R}$ and once differentiable in time $t \in \mathbb{R}_+$. The process $f(X_t, t)$ satisfies the SDE

$$df(X_t, t) = \frac{\partial f}{\partial x} dX_t + \frac{\partial f}{\partial t} dt + \frac{1}{2} \frac{\partial^2 f}{\partial x^2} (dX_t)^2$$

and can be further written as

$$df(X_t, t) = \left(\frac{\partial f}{\partial x} a(X_t, t) + \frac{\partial f}{\partial t} + \frac{1}{2} \frac{\partial^2 f}{\partial x^2} \sigma(X_t, t)^2 \right) dt + \frac{\partial f}{\partial x} \sigma(X_t, t) dB_s.$$

This result is known as **Itô formula** (see [156] page 44) and is used in the derivation of (6.5).

Bibliography

- [1] M. Abramowitz and I. A. Stegun. *Handbook of Mathematical Functions: with Formulas, Graphs, and Mathematical Tables*. Dover Publications, 1st edition, 1965.
- [2] R. R. Ackermann and J. M. Cheverud. Detecting genetic drift versus selection in human evolution. *Proc. Natl. Acad. Sci. USA*, 101(52):17946–17951, 2004.
- [3] H. Agakishiev et al. Observation of the antimatter helium-4 nucleus. *Nature*, 473(7347):353–356, 2011.
- [4] P. A. Alemany and D. ben-Avraham. Inter-particle distribution functions for one-species diffusion-limited annihilation, $A + A \rightarrow 0$. *Phys. Lett. A*, 206(1-2):18–25, 1995.
- [5] A. Ali and S. Grosskinsky. PATTERN FORMATION THROUGH GENETIC DRIFT AT EXPANDING POPULATION FRONTS. *Adv. Complex Syst.*, 13(3):349–366, 2010.
- [6] A. Ali, E. Somfai, and S. Grosskinsky. Reproduction-time statistics and segregation patterns in growing populations. *Phys. Rev. E*, 85(2):021923, 2012.
- [7] S. G. Alves, T. J. Oliveira, and S. C. Ferreira. Universal fluctuations in radial growth models belonging to the KPZ universality class. *Europhys. Lett.*, 96(4):48003, 2011.
- [8] J. G. Amar and F. Family. Universality in surface growth: Scaling functions and amplitude ratios. *Phys. Rev. A.*, 45(8):5378–5393, 1992.
- [9] J. G. Amar, P.-M. Lam, and F. Family. Surface growth with long-range correlated noise. *Phys. Rev. A.*, 43(8):4548–4550, 1991.
- [10] G. W. Anderson, A. Guionnet, and O. Zeitouni. *An Introduction to Random Matrices*. Cambridge University Press, 1st edition, 2009.

- [11] D. Applebaum. *Lévy Processes and Stochastic Calculus*. Cambridge University Press, 2nd edition, 2009.
- [12] D. Avnir. *The Fractal Approach to Heterogeneous Chemistry: Surfaces, Colloids, Polymers*. Wiley-Blackwell, 1st edition, 1989.
- [13] M. Badoual, P. Derbez, M. Aubert, and B. Grammaticos. Simulating the migration and growth patterns of *Bacillus subtilis*. *Physica A*, 388(4):549–559, 2009.
- [14] M. Balazs, J. Quastel, and T. Seppalainen. Scaling exponent for the Hopf-Cole solution of KPZ/Stochastic Burgers. *ArXiv:0909.4816*, 2009.
- [15] R. C. Ball, M. Nauenberg, and T. A. Witten. Diffusion-controlled aggregation in the continuum approximation. *Phys. Rev. A*, 29(4):2017–2020, 1984.
- [16] R. C. Ball and E. Somfai. Diffusion-controlled growth: Theory and closure approximations. *Phys. Rev. E*, 67(2):021401, 2003.
- [17] A.-L. Barabasi and H. E. Stanley. *Fractal concepts in surface growth*. Cambridge University Press, 1st edition, 1995.
- [18] D. ben Avraham, M. A. Burschka, and C. R. Doering. Statics and dynamics of a diffusion-limited reaction: Anomalous kinetics, nonequilibrium self-ordering, and a dynamic transition. *J. Stat. Phys.*, 60(5-6):695–728, 1990.
- [19] E. Ben-Jacob and P. Garik. The formation of patterns in non-equilibrium growth. *Nature*, 343(0):523–530, 1990.
- [20] E. Ben-Jacob, H. Shmueli, O. Shochet, and A. Tenenbaum. Adaptive self-organization during growth of bacterial colonies. *Physica A*, 187(3-4):378–424, 1992.
- [21] F. Biagini, Y. Hu, B. Øksendal, and T. Zhang. *Stochastic Calculus for Fractional Brownian Motion and Applications*. Springer, Berlin, 1st edition, 2008.
- [22] T. Bohr and A. Pikovsky. Anomalous diffusion in the Kuramoto-Sivashinsky equation. *Phys. Rev. Lett.*, 70(19):2892–2895, 1993.
- [23] J. A. Bonachela, C. D. Nadell, J. B. Xavier, and S. A. Levin. Universality in Bacterial Colonies. *J. Stat. Phys.*, 144(2):303–315, 2011.
- [24] M. Bramson and D. Griffeath. On the Williams-Bjerknes Tumor Growth Model I. *The Annals of Probability*, 9(2):173–185, 1981.

- [25] A. Bressler and R. Pemantle. Quantum random walks in one dimension via generating functions. *Discrete Mathematics and Theoretical Computer Science*, 2007.
- [26] C. J. Brinker and D. E. Clark. *Better Ceramics Through Chemistry III: Symposium (Materials Research Society Symposium Proceedings)*. Materials Research Society, 1st edition, 1988.
- [27] A. Brú, S. Albertos, J. L. Subiza, J. L. García-Asenjo, and I. Brú. The Universal Dynamics of Tumor Growth. *Biophys. J.*, 85(5):2948–2961, 2003.
- [28] E. Brunet, B. Derrida, and D. Simon. Universal tree structures in directed polymers and models of evolving populations. *Phys. Rev. E*, 78(6):061102, 2008.
- [29] A. Bunde and S. Havlin. *Fractals and disordered systems*. Springer, 2nd edition, 1995.
- [30] M. O. Cáceres. Lévy noise, Lévy flights, Lévy fluctuations. *J. Phys. A: Math. Gen.*, 32(33):6009, 1999.
- [31] Q.-z. Cao and P.-z. Wong. Fractal interfaces in heterogeneous Eden-like growth. *Phys. Rev. Lett.*, 67(1):77–80, 1991.
- [32] L. Cavalli-Sforza, P. Menozzi, and A. Piazza. Demic expansions and human evolution. *Science*, 259(5095):639–646, 1993.
- [33] A. K. Chattopadhyay. Memory effects in a nonequilibrium growth model. *Phys. Rev. E*, 80(1):011144, 2009.
- [34] A. V. Chechkin, R. Metzler, J. Klafter, and V. Y. Gonchar. *Introduction to the Theory of Lévy Flights*. Wiley-VCH Verlag GmbH & Co. KGaA, 2008.
- [35] G. A. Churchill. Stochastic models for heterogeneous DNA sequences. *Bulletin of Mathematical Biology*, 51(1):79–94, 1989.
- [36] D. J. Cole, B. J. T. Morgan, M. S. Ridout, L. J. Byrne, and M. F. Tuite. Estimating the number of prions in yeast cells. *Math. Med. Biol.*, 21(4):369–395, 2004.
- [37] D. J. Cole, B. J. T. Morgan, M. S. Ridout, L. J. Byrne, and M. F. Tuite. Approximations for Expected Generation Number. *Biometrics*, 63(4):1023–1030, 2007.

- [38] P. J. Collings and M. Hird. *Introduction to Liquid Crystals: Chemistry and Physics*. CRC Press, 4th edition, 1997.
- [39] J. Cook and B. Derrida. Directed polymers in a random medium: $1/d$ expansion and the n -tree approximation. *J. Phys. A: Math. Gen.*, 23(9):1523, 1990.
- [40] I. Corwin. The Kardar-Parisi-Zhang equation and universality class. *ArXiv:1106.1596*, 2011.
- [41] J. Csavina, J. Field, M. P. Taylor, S. Gao, A. Landázuri, E. A. Betterton, and A. E. Sáez. A review on the importance of metals and metalloids in atmospheric dust and aerosol from mining operations. *Sci Total Environ.*, 433(0):58–73, 2012.
- [42] A. C. de la Torre, A. Maltz, H. O. Martín, P. Catuogno, and I. García-Mata. Random walk with an exponentially varying step. *Phys. Rev. E*, 62(6):7748–7754, 2000.
- [43] L. Decreusefond and A. S. ÜstÜnel. Stochastic Analysis of the Fractional Brownian Motion. *Potential Anal.*, 10(2):177–214, 1999.
- [44] M. DeGiorgioa, M. Jakobssonb, and N. A. Rosenberga. Explaining world-wide patterns of human genetic variation using a coalescent-based serial founder model of migration outward from Africa. *Proc. Natl. Acad. Sci. USA*, 106(38):16057–16062, 2009.
- [45] B. Derrida and R. Dickman. On the interface between two growing Eden clusters. *J. Phys. A: Math. Gen.*, 24(4):L191, 1991.
- [46] C. R. Doering and D. ben Avraham. Interparticle distribution functions and rate equations for diffusion-limited reactions. *Phys. Rev. A*, 38(6):3035–3042, 1988.
- [47] M. Eden. A Two-dimensional Growth Process. *Proc. Fourth Berkeley Symposium on Maths, Statistics and Probability.*, 4(0):223–239, 1961.
- [48] S. F. Edwards and D. R. Wilkinson. The Surface Statistics of a Granular Aggregate. *Proc. R. Soc. Lond. A*, 381(1780):17–31, 1982.
- [49] S. F. Elena and R. E. Lenski. Evolution experiments with microorganisms: the dynamics and genetic bases of adaptation. *Nature Reviews*, 4(6):457–469, 2003.

- [50] A. Elfving, Y. LeMarc, J. Baranyi, and A. Ballagi. Observing Growth and Division of Large Numbers of Individual Bacteria by Image Analysis. *Appl. Environ. Microbiol.*, 70(2):675–678, 2004.
- [51] F. Family. Scaling of rough surfaces: effects of surface diffusion. *J. Phys. A: Math. Gen.*, 19(8):L441, 1986.
- [52] F. Family and T. Vicsek. Scaling of the active zone in the Eden process on percolation networks and the ballistic deposition model. *J. Phys. A.*, 18(2):L75, 1985.
- [53] F. Family and T. Vicsek. *Dynamics of Fractal Surfaces*. World Scientific Publishing, 1st edition, 1991.
- [54] J. H. Fendler. Interactions and reactions in reversed micellar systems. *Acc. Chem. Res.*, 9(4):153–161, 1976.
- [55] P. L. Ferrari and H. Spohn. Random Growth Models. *ArXiv:1003.0881*, 2010.
- [56] C. Finlayson. Biogeography and evolution of the genus *Homo*. *Trends Ecol Evol.*, 20(8):457–463, 2005.
- [57] M. C. Fisher, G. L. Koenig, T. J. White, G. San-Blas, R. Negroni, I. G. Alvarez, B. Wanke, and J. W. Taylor. Biogeographic range expansion into South America by *Coccidioides immitis* mirrors New World patterns of human migration. *Proc. Natl. Acad. Sci. USA*, 98(8):4558–4562, 2001.
- [58] H. C. Fogedby. Lévy Flights in Random Environments. *Phys. Rev. Lett.*, 73(19):2517–2520, 1994.
- [59] D. Forster, D. R. Nelson, and M. J. Stephen. Large-distance and long-time properties of a randomly stirred fluid. *Phys. Rev. A*, 16(2):732–749, 1977.
- [60] T. Gang, D.-P. Hao, X. Hui, H. Kui, and X. Zhi-Peng. Effects of memory on scaling behaviour of Kardar-Parisi-Zhang equation. *Chin. Phys. B*, 19(10):100508, 2010.
- [61] C. W. Gardiner. *Handbook of Stochastic Methods*. Springer, 4th edition, 2009.
- [62] A. Giacometti and M. Rossi. Interface dynamics from experimental data. *Phys. Rev. E*, 62(2):1716–1724, 2000.
- [63] A. Giacometti and M. Rossi. Pseudospectral approach to inverse problems in interface dynamics. *Phys. Rev. E*, 63(4):046102, 2001.

- [64] I. Giardina. Collective behavior in animal groups: Theoretical models and empirical studies. *HFSP J*, 2(4):205–219, 2008.
- [65] N. Goldenfeld. *Lectures on Phase Transitions and the Renormalization Group (Frontiers in Physics)*. Westview Press, 1st edition, 1992.
- [66] D. Grier, E. Ben-Jacob, R. Clarke, and L. M. Sander. Morphology and Microstructure in Electrochemical Deposition of Zinc. *Phys. Rev. Lett.*, 56(12):1264–1267, 1986.
- [67] M. J. Grimson and G. C. Barker. Scaling behaviour of an extended Eden model. *J. Phys. A: Math. Gen.*, 27(3):653–658, 1994.
- [68] M. Hahn, K. Kobayashi, and S. Umarov. Fokker-Planck-Kolmogorov equations associated with time-changed fractional Brownian motion. *Proc. Amer. Math. Soc.*, 139(2):691–705, 2011.
- [69] O. Hallatschek, P. Hersen, S. Ramanathan, and D. R. Nelson. Genetic drift at expanding frontiers promotes gene segregation. *Proc. Natl. Acad. Sci. USA*, 104(50):19926–19930, 2007.
- [70] O. Hallatschek and D. R. Nelson. Gene surfing in expanding populations. *Theor. Popul. Biol.*, 73(1):158–170, 2008.
- [71] O. Hallatschek and D. R. Nelson. Life at the front of an expanding population. *Evolution*, 64(1):193–206, 2010.
- [72] T. Halpin-Healy. Directed polymers in random media: Probability distributions. *Phys. Rev. A*, 44(6):R3415–R3418, 1991.
- [73] W. G. Hanan and D. M. Heffernan. Multifractal analysis of the branch structure of diffusion-limited aggregates. *Phys. Rev. E*, 85(2):021407, 2012.
- [74] E. R. Harrison. *Cosmology: The Science of the Universe*. Cambridge University Press, 2nd edition, 2000.
- [75] S. Havlin, S. V. Buldyrev, H. E. Stanley, and G. H. Weiss. Probability distribution of the interface width in surface roughening: analogy with a Lévy flight. *J. Phys. A: Math. Gen.*, 24(16):L925, 1991.
- [76] S. Hawking. *A Brief History Of Time*. Bantam, 1st edition, 1998.
- [77] S. He, G. L. M. K. S. Kahanda, and P.-z. Wong. Roughness of wetting fluid invasion fronts in porous media. *Phys. Rev. Lett.*, 69(26):3731–3734, 1992.

- [78] Y.-L. He, H.-N. Yang, T.-M. Lu, and G.-C. Wang. Measurements of dynamic scaling from epitaxial growth front: Fe film on fe(001). *Phys. Rev. Lett.*, 69(26):3770–3773, 1992.
- [79] J. Herrmann. Diffusion in the general theory of relativity. *Phys. Rev. D*, 82(2):024026, 2010.
- [80] G. Hewitt. The genetic legacy of the Quaternary ice ages. *Nature*, (6789), 2000.
- [81] P. C. Hohenberg and B. I. Halperin. Theory of dynamic critical phenomena. *Rev. Mod. Phys.*, 49(3):435–479, 1977.
- [82] V. K. Horvath, F. Family, and T. Vicsek. Dynamic scaling of the interface in two-phase viscous flows in porous media. *J. Phys. A: Math. Gen.*, 24(1):L25, 1991.
- [83] Y. Hu, D. Nualart, and J. Song. Fractional martingales and characterization of the fractional Brownian motion. *ArXiv:0711.1313*, 2007.
- [84] M. A. C. Huergo, M. A. Pasquale, A. E. Bolzán, A. J. Arvia, and P. H. González. Morphology and dynamic scaling analysis of cell colonies with linear growth fronts. *Phys. Rev. E*, 82(3):031903, 2010.
- [85] X. Hui, T. Gang, M. Jingjie, H. Dapeng, and X. Zhi-peng. Scaling behaviour of the time-fractional Kardari-Parisi-Zhang equation. *J. Phys. A*, 44(27):275003, 2011.
- [86] T. Imamura and T. Sasamoto. Exact Solution for the Stationary Kardar-Parisi-Zhang Equation. *Phys. Rev. Lett.*, 108(19):190603, 2012.
- [87] H. Itoh, J. Wakita, T. Matsuyama, and M. Matsushita. Periodic Pattern Formation of Bacterial Colonies. *J. Phys. Soc. Jpn.*, 68(4):1436–1443, 1999.
- [88] C. Jacob. Branching Processes: Their Role in Epidemiology. *Int. J. Environ. Res. Public Health*, 7(3):1186–1204, 2010.
- [89] H. Jeong, B. Tombor, R. Albert, Z. Oltvai, and A.-L. Barabási. The large-scale organization of metabolic networks. *Nature*, 407(6804):651–654, 2000.
- [90] L.-L. Jiang, T. Zhou, M. Perc, and B.-H. Wang. Effects of competition on pattern formation in the rock-paper-scissors game. *Phys. Rev. E*, 84(2):021912, 2011.

- [91] K. Johansson. Shape Fluctuations and Random Matrices. *Commun. Math. Phys.*, 209(2):437–476, 2000.
- [92] R. Jullien and R. Botet. Scaling properties of the surface of the Eden model in $d = 2, 3, 4$. *J. Phys. A: Math. Gen.*, 18(12):2279, 1985.
- [93] R. Jullien and R. Botet. *Aggregation and Fractal Aggregates*. Singapore: World Scientific, 1st edition, 1987.
- [94] M. Karayiorgou, M. Torrington, G. R. Abecasis, H. Pretorius, B. Robertson, S. Kaliski, S. Lay, C. Sobin, N. Möller, S. L. Lundy, M. L. Blundell, J. A. Gogos, and J. L. Roos. Phenotypic characterization and genealogical tracing in an Afrikaner schizophrenia database. *Am J Med Genet B*, 124B(1):20–28, 2004.
- [95] M. Kardar, G. Parisi, and Y.-C. Zhang. Dynamic Scaling of Growing Interfaces. *Phys. Rev. Lett.*, 56(9):889–892, 1986.
- [96] M. Kardar and Y.-C. Zhang. Scaling of Directed Polymers in Random Media. *Phys. Rev. Lett.*, 58(20):2087–2090, 1987.
- [97] E. Katzav and M. Schwartz. Kardar-Parisi-Zhang equation with temporally correlated noise: A self-consistent approach. *Phys. Rev. E*, 70(1):011601, 2004.
- [98] K. D. Keefer and D. W. Schaefer. Growth of Fractally Rough Colloids. *Phys. Rev. Lett.*, 56:2376–2379, 1986.
- [99] H. Kilgariff. Introduction to Bacteria, 2nd Edition. *J Med Microbiol.*, 38(5):388, 1993.
- [100] J. M. Kim and J. M. Kosterlitz. Growth in a restricted solid-on-solid model. *Phys. Rev. Lett.*, 62(19):2289–2292, 1989.
- [101] J. M. Kim, M. A. Moore, and A. J. Bray. Zero-temperature directed polymers in a random potential. *Phys. Rev. A*, 44(4):2345–2351, 1991.
- [102] Y. Kim and S. H. Yook. Phase transition in restricted solid-on-solid models with finite-distance hoppings. *J. Phys. A: Math. Gen.*, 30(14):L449, 1997.
- [103] M. Kimmel and D. E. Axelrod. *Branching Processes in Biology*. Springer, 1st edition, 2002.

- [104] S. Kirkpatrick, C. D. Gelatt, and M. P. Vecchi. Optimization by Simulated Annealing. *Science*, 220(4598):671–680, 1983.
- [105] S. Kitsunezaki. Interface Dynamics for Bacterial Colony Formation. *J. Phys. Soc. Jpn.*, 66(5):1544–1550, 1997.
- [106] F. C. Klebaner. *Introduction to Stochastic Calculus with Applications*. World Scientific Publishing Company, 2nd edition, 1999.
- [107] S. Klopstein, M. Currat, and L. Excoffier. The Fate of Mutations Surfing on the Wave of a Range Expansion. *Mol. Biol. Evol.*, 3(23):482–490, 2005.
- [108] N. Kobayashi, O. Moriyama, S. Kitsunezaki, Y. Yamazaki, and M. Matsushita. Dynamic Scaling of the Growing Rough Surfaces. *J. Phys. Soc. Jpn.*, 73(8):2112–2116, 2004.
- [109] N. Kobayashi, T. Sato, Y. Yamazaki, and M. Matsushita. Modelling and Numerical Analysis of the Colony Formation of Bacteria. *J. Phys. Soc. Jpn.*, 72(4):970–971, 2003.
- [110] R. Kopelman. Fractal Reaction Kinetics. *Science*, 241(4873):1620–1626, 1988.
- [111] K. S. Korolev, M. Avlund, O. Hallatschek, and D. R. Nelson. Genetic demixing and evolution in linear stepping stone models. *Rev. Mod. Phys.*, 82(2):1691–1718, 2010.
- [112] K. S. Korolev, J. B. Xavier, D. R. Nelson, and K. R. Foster. A Quantitative Test of Population Genetics Using Spatiogenetic Patterns in Bacterial Colonies. *The American Naturalist*, 178(4):538–552, October 2011.
- [113] M. Kotrla and A. Levi. Kinetics of crystal growth near the roughening transition: a Monte Carlo study. *Surf Sci*, 317(12):183–193, 1994.
- [114] P. L. Krapivsky and S. Redner. Random walk with shrinking steps. *Am. J. Phys.*, 72:591–598, 2004.
- [115] G. A. Kriegsmann. Pattern formation in microwave heated ceramics: cylinders and slabs. *IMA J Appl Math.*
- [116] J. Krug and P. Meakin. Microstructure and surface scaling in ballistic deposition at oblique incidence. *Phys. Rev. A*, 40(4):2064–2077, 1989.

- [117] J. Krug, P. Meakin, and T. Halpin-Healy. Amplitude universality for driven interfaces and directed polymers in random media. *Phys. Rev. A.*, 45(2):638–653, 1992.
- [118] J. Krug and H. Spohn. Mechanism for rough-to-rough transitions in surface growth. *Phys. Rev. Lett.*, 64(19):2332–2332, 1990.
- [119] E. W. Kuennen and C. Y. Wang. Off-lattice radial Eden cluster growth in two and three dimensions. *J. Stat. Mech. Theory Exp.*, 2008(5):P05014, 2008.
- [120] J.-T. Kuhr, M. Leisner, and E. Frey. Range expansion with mutation and selection: dynamical phase transition in a two-species Eden model. *New J. Phys.*, 13(11):113013, 2011.
- [121] S. Kyriacos, F. Nekka, L. Cartilier, and P. Vico. Insights into the Formation Process of the Retinal Vasculature. *Fractals*, 5(4):615–624, 1997.
- [122] L. Miettinen, M. Myllys, J. Merikoski, and J. Timonen. Experimental determination of KPZ height-fluctuation distributions. *Eur. Phys. J. B*, 46(1):55–60, 2005.
- [123] A. M. Lacasta, I. R. Cantalapiedra, C. E. Auguet, A. Peñaranda, and L. Ramírez-Piscina. Modeling of spatiotemporal patterns in bacterial colonies. *Phys. Rev. E*, 59(6):7036–7041, 1999.
- [124] C.-H. Lam and L. M. Sander. Inverse method for interface problems. *Phys. Rev. Lett.*, 71(4):561–564, 1993.
- [125] J. S. Langer. Instabilities and pattern formation in crystal growth. *Rev. Mod. Phys.*, 52(1):1–28, 1980.
- [126] N. I. Lebovka and N. V. Vygornitskii. How does the geometry affect the criticality in two-component spreading phenomena? *J. Phys. A: Math. Gen.*, 31(46):9199–9208, 1998.
- [127] R. Lehe, O. Hallatschek, and L. Peliti. The Rate of Beneficial Mutations Surfing on the Wave of a Range Expansion. *PLoS Comput. Biol.*, 8(3):e1002447, 2012.
- [128] G. Li, L. M. Sander, and P. Meakin. Comment on “Self-similarity of diffusion-limited aggregates and electrodeposition clusters”. *Phys. Rev. Lett.*, 63(12):1322–1322, 1989.

- [129] M. Y. Lin, H. M. Lindsay, D. A. Weitz, R. Klein, R. C. Ball, and P. Meakin. Universal diffusion-limited colloid aggregation. *J. Phys.: Condens. Matter.*, 2(13):3093, 1990.
- [130] J.-P. Luminet, J. R. Weeks, A. Riazuelo, R. Lehoucq, and J.-P. Uzan. Do-decahedral space topology as an explanation for weak wide-angle temperature correlations in the cosmic microwave background. *Nature*, 425(6958):593–595, 2003.
- [131] D. H. Lyth and A. Riotto. Particle physics models of inflation and the cosmological density perturbation. *Phys. Rep.*, 314(12):1–146, 1999.
- [132] B. B. Mandelbrot. *The Fractal Geometry of Nature*. W. H. Freeman, 1st edition, 1982.
- [133] B. B. Mandelbrot, B. Kol, and A. Aharony. Angular Gaps in Radial Diffusion-Limited Aggregation: Two Fractal Dimensions and Nontransient Deviations from Linear Self-Similarity. *Phys. Rev. Lett.*, 88(5):055501, 2002.
- [134] A. A. Masoudi, S. Hosseinabadi, J. Davoudi, M. Khorrami, and M. Kohandel. Statistical analysis of radial interface growth. *J. Stat. Mech. Theory Exp.*, 2012(2):L02001, 2012.
- [135] T. O. Masser and D. ben Avraham. A Method of intervals for the study of diffusion-limited annihilation, $A + A \rightarrow 0$. *Phys. Rev. E*, 63(6):066108, 2001.
- [136] M. Matsushita, J. Wakita, H. Itoh, K. Watanabe, T. Arai, T. Matsuyama, H. Sakaguchi, and M. Mimura. Formation of colony patterns by a bacterial cell population. *Physica A*, 274(1-2):190–199, 1999.
- [137] E. Mayr. *Animal Species and Evolution*. Belknap Press, 1st edition, 1963.
- [138] P. Meakin. Diffusion-controlled cluster formation in 2 – 6 dimensional space. *Phys. Rev. A*, 27(3):1495–1507, 1983.
- [139] P. Meakin. Universal scaling properties of ballistic deposition and Eden growth on surfaces. *J. Phys. A: Math. Gen.*, 20(16):L1113, 1987.
- [140] P. Meakin. Fractal structures. *Prog. Solid State Chem.*, 20(3):135–233, 1990.
- [141] P. Meakin. The growth of rough surfaces and interfaces. *Phys. Rep.*, 235(45):189–289, 1993.

- [142] P. Meakin. *Fractals, Scaling and Growth Far from Equilibrium*. Cambridge University Press, 1st edition, 1998.
- [143] E. Medina, T. Hwa, M. Kardar, and Y.-C. Zhang. Burgers equation with correlated noise: Renormalization-group analysis and applications to directed polymers and interface growth. *Phys. Rev. A.*, 39(6):3053–3075, 1989.
- [144] R. Metzler and T. F. Nonnenmacher. Space-and time-fractional diffusion and wave equations, fractional Fokker-Planck equations, and physical motivation. *Chem Phys*, 284(1-2):67–90, 2002.
- [145] S. Mitri, J. a. B. Xavier, and K. R. Foster. Social evolution in multispecies biofilms. *Proc. Natl. Acad. Sci. USA*, 108(2):10839–10846, 2011.
- [146] M. Mobilia. Oscillatory dynamics in rock-paper-scissors games with mutations. *J. Theor. Biol.*, 264(1):1–10, 2010.
- [147] W. L. Morgan, J. N. Bardsley, J. Lin, and B. L. Whitten. Theory of ion-ion recombination in plasmas. *Phys. Rev. A*, 26(3):1696–1703, 1982.
- [148] R. Munasinghe, R. Rajesh, R. Tribe, and O. Zaboronski. Multi-scaling of the n-Point Density Function for Coalescing Brownian Motions. *Commun. Math. Phys.*, 268(3):717–725, 2006.
- [149] J. D. Murray. *Mathematical Biology II: Spatial Models and Biomedical Applications*. Springer, 3rd edition, 2003.
- [150] T. Nagatani. From ballistic deposition to the Kardar-Parisi-Zhang equation through a limiting procedure. *Phys. Rev. E*, 58(1):700–703, 1998.
- [151] M. Nei, T. Maruyama, and R. Chakraborty. The Bottleneck Effect and Genetic Variability in Populations. *Evolution*, 29(1):1–10, 1975.
- [152] L. Niemeyer, L. Pietronero, and H. J. Wiesmann. Fractal Dimension of Dielectric Breakdown. *Phys. Rev. Lett.*, 52(12):1033–1036, 1984.
- [153] J. Nittmann and H. E. Stanley. Role of fluctuations in viscous fingering and dendritic crystal growth: a noise-driven model with non-periodic sidebranching and no threshold for onset. *J. Phys. A: Math. Gen.*, 20(15):L981, 1987.
- [154] G. W. Niven, T. Fuks, J. S. Morton, S. A. Rua, and B. M. Mackey. A novel method for measuring lag times in division of individual bacterial cells using image analysis. *J Microbiol Methods.*, 65(2):311–317, 2006.

- [155] M. Ohgiwari, M. Matsushita, and T. Matsuyama. Morphological Changes in Growth Phenomena of Bacterial Colony Patterns. *J. Phys. Soc. Jpn.*, 61(3):816–822, 1992.
- [156] B. Øksendal. *Stochastic Differential Equations: An Introduction with Applications*. Springer, 6th edition, 2003.
- [157] T. J. Oliveira, S. C. Ferreira, and S. G. Alves. Universal fluctuations in Kardar-Parisi-Zhang growth on one-dimensional flat substrates. *Phys. Rev. E*, 85(1):010601, 2012.
- [158] L. R. Paiva and S. C. F. Jr. Universality class of isotropic on-lattice Eden clusters. *J. Phys. A: Math. Theor.*, 40(1):F43–F49, 2006.
- [159] K. J. Palmer, M. S. Ridout, and B. J. T. Morgan. Modelling cell generation times by using the tempered stable distribution. *J. Roy. Statist. Soc. Ser. C Appl. Statist.*, 57(4):379–397, 2008.
- [160] L. Paterson. Radial fingering in a Hele Shaw cell. *J. Fluid Mech.*, 113:513–529, 1981.
- [161] L. Paterson. Diffusion-Limited Aggregation and Two-Fluid Displacements in Porous Media. *Phys. Rev. Lett.*, 52(18):1621–1624, 1984.
- [162] I. Pázsit and L. Pal. *Neutron Fluctuations: A Treatise on the Physics of Branching Processes*. Elsevier Science, 1st edition, 2007.
- [163] L. Popovic. Asymptotic genealogy of a critical branching process. *ArXiv:math/0503577*, 2005.
- [164] E. O. Powell. Growth Rate and Generation Time of Bacteria, with Special Reference to Continuous Culture. *J Gen Microbiol*, 15(3):492–511, 1956.
- [165] M. Prähofer and H. Spohn. Scale Invariance of the PNG Droplet and the Airy Process. *J. Stat. Phys.*, 108(5):1071–1106, 2002.
- [166] T. Rador. Random walkers with shrinking steps in d dimensions and their long term memory. *Phys. Rev. E*, 74(5):051105, 2006.
- [167] T. Rador and S. Taneri. Random walks with shrinking steps: First-passage characteristics. *Phys. Rev. E*, 73(3):036118, 2006.
- [168] O. Rahn. A CHEMICAL EXPLANATION OF THE VARIABILITY OF THE GROWTH RATE. *J Gen Physiol.*, 15(3):257–277, 1932.

- [169] S. Ramachandran, O. Deshpande, C. C. Roseman, N. A. Rosenberg, M. W. Feldman, and L. L. Cavalli-Sforza. Support from the relationship of genetic and geographic distance in human populations for a serial founder effect originating in Africa. *Proc. Natl. Acad. Sci. USA*, 102(44):15942–15947, 2005.
- [170] M. Rappaz, A. Jacot, and W. Boettinger. Last-stage solidification of alloys: Theoretical model of dendrite-arm and grain coalescence. *Metall Mater Trans A*, 34(3):467–479, 2003.
- [171] T. Reichenbach, M. Mobilia, and E. Frey. Mobility promotes and jeopardizes biodiversity in rock-paper-scissors games. *Nature*, 448(7157):1046–1049, 2007.
- [172] J. H. Relethford. Global patterns of isolation by distance based on genetic and morphological data. *Hum Biol.*, 76(4):499–513, 2004.
- [173] I. Rodriguez-Iturbe and A. Rinaldo. *Fractal River Basins: Chance and Self-Organization*. Cambridge University Press, 1st edition, 1997.
- [174] M. Rost and J. Krug. A particle model for the Kuramoto-Sivashinsky equation. *Physica D*, 88(1):1–13, 1995.
- [175] S. P. Sabatini, F. Solari, and L. Secchi. Rapid range expansion of a wing-dimorphic bush-cricket after the 2003 climatic anomaly. *Biol. J. Linn. Soc.*, 97(1):118127, 2009.
- [176] P. G. Saffman and G. Taylor. The penetration of a fluid into a porous medium or Hele-Shaw cell containing a more viscous fluid. *Proc. R. Soc. Lond. A*, 245(1242):312–329, 1958.
- [177] Y. Saito and H. Müller-Krumbhaar. Critical Phenomena in Morphology Transitions of Growth Models with Competition. *Phys. Rev. Lett.*, 74(21):4325–4328, 1995.
- [178] Y. Saito and S. Omura. Domain competition during ballistic deposition: Effect of surface diffusion and surface patterning. *Phys. Rev. E*, 84(2):021601, 2011.
- [179] S. G. Samko, A. A. Kilbas, and O. I. Marichev. *Fractional Integrals and Derivatives: Theory and Applications*. Taylor and Francis Ltd, 1st edition, 1993.
- [180] K. Sasaki and T. Nakagawa. Exact Results for a Diffusion-Limited Pair Annihilation Process on a One-Dimensional Lattice. *J. Phys. Soc. Jpn.*, 69(5):1341–1351, 2000.

- [181] T. Sasamoto and H. Spohn. Exact height distributions for the KPZ equation with narrow wedge initial condition. *Nucl. Phys. B*, 834(3):523–542, 2010.
- [182] C. A. Serino and S. Redner. The pearson walk with shrinking steps in two dimensions. *J. Stat. Mech*, 2010(1):P01006, 2010.
- [183] J. A. Shapiro. Organization of developing *Escherichia coli* colonies viewed by scanning electron microscopy. *J Bacteriol.*, 169(1):142–156, 1987.
- [184] M. Shiino and M. Yamana. Statistical mechanics of stochastic neural networks: Relationship between the self-consistent signal-to-noise analysis, Thouless-Anderson-Palmer equation, and replica symmetric calculation approaches. *Phys. Rev. E*, 69(2):011904, 2004.
- [185] M. F. Shlesinger, G. M. Zaslavsky, and U. Frisch. *Lévy Flights and Related Topics in Physics: Proceedings of the International Workshop Held at Nice, France, 27-30 June 1994 - Lecture Notes in Physics v. 450*. Springer, Berlin, 1995.
- [186] A. I. Shushin. Magnetic field effects on electron-hole recombination in disordered organic semiconductors. *Phys. Rev. B*, 84(11):115212, 2011.
- [187] D. Siegal-Gaskins and S. Crosson. Tightly-regulated and heritable division control in single bacterial cells Biophys. *Biophys J*, 95(4):2063–2072, 2008.
- [188] P. Singleton. *Introduction to bacteria*. Wiley-Blackwell, 2nd edition, 1992.
- [189] M. L. Slater, S. O. Sharrow, and J. J. Gart. Cell cycle of *Saccharomy cerevisiae* in populations growing at different rates. *Proc. Natl. Acad. Sci. USA*, 74(9):3850–3854, 1977.
- [190] B. D. Slaughter, S. E. Smith, and R. Li. Symmetry Breaking in the Life Cycle of the Budding Yeast. *Cold Spring Harb Perspect Biol.*, 1(3):a003384, 2009.
- [191] E. Somfai and L. M. Sander. Scaling and river networks: A Landau theory for erosion. *Phys. Rev. E*, 56(1):R5–R8, 1997.
- [192] H. Stanley, A. Bunde, S. Havlin, J. Lee, E. Roman, and S. Schwarzer. Dynamic mechanisms of disorderly growth: Recent approaches to understanding diffusion limited aggregation. *Physica A*, 168(1):23–48, 1990.
- [193] H. Stanley, A. Coniglio, S. Havlin, J. Lee, S. Schwarzer, and M. Wolf. Diffusion limited aggregation: a paradigm of disorderly cluster growth. *Physica A*, 205(1-3):254–271, 1994.

- [194] H. E. Stanley, F. Family, and H. Gould. Kinetics of aggregation and gelation. *J Polym Sci*, 73(1):19–37, 1985.
- [195] K. A. Takeuchi, M. Sano, T. Sasamoto, and H. Spohn. Growing interfaces uncover universal fluctuations behind scale invariance. *Scientific Reports*, 1(34):1–4, 2011.
- [196] A. Templeton. Out of Africa again and again. *Nature*, 416(6876):45–51, 2002.
- [197] H. Thome, M. Rabaud, V. Hakim, and Y. Couder. The saffman-Taylor instability: From the linear to the circular geometry. *Phys. Fluids A*, 1(2):224–240, 1989.
- [198] D. W. Thompson. *On growth and form*. Cambridge University Press, 1st edition, 1992.
- [199] R. Tokita, T. Katoh, Y. Maeda, J. Wakita, M. Sano, T. Matsuyama, and M. Matsushita. Pattern Formation of Bacterial Colonies by *Escherichia coli*. *J. Phys. Soc. Jpn.*, 78(7):074005, 2009.
- [200] J. Tosevski, P. Sazdanovic, I. Zivanovic-Macuzic, M. S. Vulovic, D. Jeremic, N. Milosevic, and D. Ristanovic. Fractal analysis of dendritic arborization patterns of pyramidal neurons in human basolateral amygdala. *Annals of General Psychiatry*, 7(1), 2008.
- [201] C. A. Tracy and H. Widom. Total current fluctuations in the asymmetric simple exclusion process. *J. Math. Phys.*, 50(9):095204, 2009.
- [202] N. Vandewalle and M. Ausloos. Lack of universality in two-dimensional multicomponent spreading phenomena. *Phys. Rev. E*, 52(4):3447–3454, 1995.
- [203] N. Vandewalle and M. Ausloos. Two-component spreading phenomena: Why the geometry makes the criticality. *Phys. Rev. E*, 54(3):3006–3008, 1996.
- [204] T. Vicsek. *Fractal Growth Phenomena*. World Scientific Publishing, 2nd edition, 1991.
- [205] T. Vicsek, M. Cserzó, and V. K. Horváth. Self-affine growth of bacterial colonies. *Physica A*, 167(2):315–321, 1990.
- [206] Y. Wakamoto, J. Ramsden, and K. Yasuda. Single-cell growth and division dynamics showing epigenetic correlations. *Analyst*, 130(3):311–317, 2005.

- [207] J. Wakita, H. Itoh, T. Matsuyama, and M. Matsushita. Self-Affinity for the Growing Interface of Bacterial Colonies. *J. Phys. Soc. Jpn.*, 66(1):67–72, 1997.
- [208] J. Wakita, I. Ràfols, H. Itoh, T. Matsuyama, and M. Matsushita. Experimental Investigation on the Formation of Dense-Branching-Morphology-Like Colonies in Bacteria. *J. Phys. Soc. Jpn.*, 67(10):3630–3636, 1998.
- [209] L. H. Walkinshaw and D. A. Zimmerman. Range Expansion of the Brewer Blackbird in Eastern North America. *The Condor*, 63(2):162–177, 1961.
- [210] C. Y. Wang, P. L. Liu, and J. B. Bassingthwaite. Off-lattice Eden-C cluster growth model. *J. Phys. A: Math. Gen.*, 28(8):2141, 1995.
- [211] D. Wegmann, M. Currat, and L. Excoffier. Molecular Diversity After a Range Expansion in Heterogeneous Environments. *Genetics*, 174(4):2009–2020, 2006.
- [212] T. Williams and R. Bjerknes. Hyperplasia: the spread of abnormal cells through a plane lattice. *Adv. in Appl. Prob.*, 3(210), 1971.
- [213] K. G. Wilson and J. Kogut. The renormalization group and the ϵ expansion. *Phys. Rep.*, 12(2):75–199, 1974.
- [214] L. G. Wilson, V. A. Martinez, J. Schwarz-Linek, J. Tailleur, G. Bryant, P. N. Pusey, and W. C. K. Poon. Differential Dynamic Microscopy of Bacterial Motility. *Phys. Rev. Lett.*, 106(1):018101, 2011.
- [215] H. S. Wio, C. Escudero, J. A. Revelli, R. R. Deza, and M. S. de la Lama. Recent developments on the Kardar Parisi Zhang surface-growth equation. *Philos Transact A Math Phys Eng Sci*.
- [216] T. A. Witten and L. M. Sander. Diffusion-Limited Aggregation, a Kinetic Critical Phenomenon. *Phys. Rev. Lett.*, 47(19):1400–1403, 1981.
- [217] D. E. Wolf and J. Villain. Growth with Surface Diffusion. *Europhys. Lett.*, 13(5):389, 1990.
- [218] J. o. B. Xavier, E. Martinez-Garcia, and K. R. Foster. Social Evolution of Spatial Patterns in Bacterial Biofilms: When conflict drives disorder. *The American Naturalist*, 174(1), 2009.
- [219] T. Zhou, Z.-Q. Fu, and B.-H. Wang. Epidemic dynamics on complex networks. *ArXiv:0508096*, 2005.